NAVAL POSTGRADUATE SCHOOL

MONTEREY, CALIFORNIA

DISSERTATION

RIP CHANNELS, MEGACUSPS, AND SHORELINE CHANGE: MEASUREMENTS AND MODELING

by

Mark D. Orzech

June 2010

Dissertation Supervisor: Edward B. Thornton
Committee Chair: Jamie H. MacMahan

Approved for public release; distribution is unlimited

THIS PAGE INTENTIONALLY LEFT BLANK

REPORT DOCUMENTATION PAGE			*Form Approved OMB No. 0704-0188*

1. AGENCY USE ONLY *(Leave blank)*	**2. REPORT DATE** June 2010	**3. REPORT TYPE AND DATES COVERED** Dissertation

4. TITLE AND SUBTITLE: Rip Channels, Megacusps, and Shoreline Change: Measurements and Modeling	**5. FUNDING NUMBERS**
6. AUTHOR(S) Mark D. Orzech	
7. PERFORMING ORGANIZATION NAME(S) AND ADDRESS(ES) Naval Postgraduate School Monterey, CA 93943-5000	**8. PERFORMING ORGANIZATION REPORT NUMBER**
9. SPONSORING / MONITORING AGENCY NAME(S) AND ADDRESS(ES) N/A	**10. SPONSORING / MONITORING AGENCY REPORT NUMBER**

11. SUPPLEMENTARY NOTES The views expressed in this thesis are those of the author and do not reflect the official policy or position of the Department of Defense or the U.S. Government. IRB Protocol number _____.

12a. DISTRIBUTION / AVAILABILITY STATEMENT Approved for public release; distribution is unlimited.	**12b. DISTRIBUTION CODE**

13. ABSTRACT (maximum 200 words)

To investigate the relationship between alongshore rip channel migration rates and alongshore sediment transport rates, multi-year surf-zone video and wave datasets are examined at three sites along Monterey Bay, on the coast of California. Time-averaged, rectified video images are used to estimate daily rip migration rates, and the CERC formula is used to compute concurrent bulk alongshore sediment transport rates. Correlation coefficients between daily rates of transport and migration are low, but they improve with frequency-based filtering. While higher frequency migration events (on time scales shorter than eight days) are often obscured below the "noise floor," longer period oscillations (spring/neap tidal and seasonal cycles) show up more clearly. Cumulatively summed mean rip migration distance and net alongshore sediment transport correlate well (with correlation coefficient r = 0.76 – 0.94), indicating that an approximately linear relationship exists at longer timescales.

To examine the nature of megacusp formation on rip channel bathymetries and identify dominant sediment transport components, five years of surf-zone video and ADCP wave data are analyzed and the XBeach 2DH nearshore model is applied in a series of simulations over realistic bathymetries. XBeach is shown to hindcast measured shoreline change with moderate skill for lower wave energies. A process-based analysis is used to identify significant forcing terms at mean, infragravity, and very-low-frequency timescales. Observations and model results both suggest that megacusps can form shoreward of either rip channels or shoals, depending on forcing conditions. In all model simulations, mean advective sediment transport plays the most important role in the creation of megacusps.

14. SUBJECT TERMS rip channels, megacusps, alongshore sediment transport, morphodynamics, XBeach, surf-zone video, correlations, infragravity, VLF	**15. NUMBER OF PAGES** 133
	16. PRICE CODE

17. SECURITY CLASSIFICATION OF REPORT	**18. SECURITY CLASSIFICATION OF THIS PAGE**	**19. SECURITY CLASSIFICATION OF ABSTRACT**	**20. LIMITATION OF ABSTRACT**
Unclassified	Unclassified	Unclassified	UU

NSN 7540-01-280-5500 Standard Form 298 (Rev. 2-89)
Prescribed by ANSI Std. 239-18

THIS PAGE INTENTIONALLY LEFT BLANK

Approved for public release; distribution unlimited

RIP CHANNELS, MEGACUSPS, AND SHORELINE CHANGE: MEASUREMENTS AND MODELING

Mark D. Orzech
Civilian Research Associate, United States Navy
B.S., Harvey Mudd College, 1988
M.C.E., University of Delaware, 1997

Submitted in partial fulfillment of the
requirements for the degree of

DOCTOR OF PHILOSOPHY IN PHYSICAL OCEANOGRAPHY

from the

NAVAL POSTGRADUATE SCHOOL
June 2010

Author: _____
Mark D. Orzech

Approved by:

_____	_____
Edward B. Thornton	Jamie H. MacMahan
Professor of Oceanography (Emer.)	Professor of Oceanography
Dissertation Supervisor	Dissertation Committee Chair
_____	_____
Timothy P. Stanton	Thomas H.C. Herbers
Professor of Oceanography	Professor of Oceanography
_____	_____
Kenneth Davidson	Jeffrey D. Paduan
Professor of Meteorology (Emer.)	Professor of Oceanography

Approved by: _____
Jeffrey D. Paduan, Chair, Department of Oceanography

Approved by: _____
Douglas Moses, Vice Provost for Academic Affairs

THIS PAGE INTENTIONALLY LEFT BLANK

ABSTRACT

To investigate the relationship between alongshore rip channel migration rates and alongshore sediment transport rates, multi-year surf-zone video and wave datasets are examined at three sites along Monterey Bay, on the coast of California. Time-averaged, rectified video images are used to estimate daily rip migration rates, and the CERC formula is used to compute concurrent bulk alongshore sediment transport rates. Correlation coefficients between daily rates of transport and migration are low, but they improve with frequency-based filtering. While higher frequency migration events (on time scales shorter than eight days) are often obscured below the "noise floor," longer period oscillations (spring/neap tidal and seasonal cycles) show up more clearly. Cumulatively summed mean rip migration distance and net alongshore sediment transport correlate well (with correlation coefficient r = 0.76 – 0.94), indicating that an approximately linear relationship exists at longer timescales.

To examine the nature of megacusp formation on rip channel bathymetries and identify dominant sediment transport components, five years of surf-zone video and ADCP wave data are analyzed and the XBeach 2DH nearshore model is applied in a series of simulations over realistic bathymetries. XBeach is shown to hindcast measured shoreline change with moderate skill for lower wave energies. A process-based analysis is used to identify significant forcing terms at mean, infragravity, and very-low-frequency timescales. Observations and model results both suggest that megacusps can form shoreward of either rip channels or shoals, depending on forcing conditions. In all model simulations, mean advective sediment transport plays the most important role in the creation of megacusps.

THIS PAGE INTENTIONALLY LEFT BLANK

TABLE OF CONTENTS

LIST OF FIGURES

THIS PAGE INTENTIONALLY LEFT BLANK

LIST OF TABLES

THIS PAGE INTENTIONALLY LEFT BLANK

LIST OF ACRONYMS AND ABBREVIATIONS

1D	One-dimensional
2D	Two-dimensional
2DH	Two-dimensional-horizontal; depth-averaged
ADCP	Acoustic Doppler current profiler
ARGUS	Video camera processing system developed by Oregon State University
ATV	All-Terrain Vehicle
avg	average
b/w	black and white
CDIP	Coastal Data Information Program (U.C. San Diego)
CERC	Coastal Engineering Research Center (USACE)
COCMP	Coastal Ocean Currents Modeling Program (State of California)
Eq.	Equation
Fig.	Figure
GLM	Generalized Lagrangian Mean (Andrews & McIntyre, 1978)
GPS	Global Positioning System
hr	hour
Hz	Hertz
JONSWAP	Joint North Sea Wave Project (refers to type of wave frequency spectrum)
km	kilometers
m	meters
mm	millimeters
MSL	Mean Sea Level
NC	North Carolina
NOAA	National Oceanic and Atmospheric Administration
NPS	Naval Postgraduate School
O( )	Of the order of ... (used to denote approximate magnitude)
PWC	Personal Watercraft (“jetski”)
RCEX	Rip Current Experiment (Sand City, California, May 2007)
RMS, rms	Root-mean-square
RO	Rip-opposite (located shoreward of rip channels)

s	seconds
SO	Shoal-opposite (located shoreward of shoals between rip channels)
USACE	United States Army Corps of Engineers
VLF	Very-low-frequency (0.0005 to 0.004 Hz)

ACKNOWLEDGMENTS

This research was supported by the the State of California's Coastal Ocean Currents Modeling Program (COCMP), as well as Office of Naval Research (ONR) contracts N0001408WR20006, N00014-05-1-0154, N0001407WR20226, N00001408WR20006, N000140710556, and National Science Foundation contracts OCE 0728324 and OCE 0754426. My sincere appreciation goes first to Drs. Ed Thornton, Jamie MacMahan, Ad Reniers, and Tim Stanton for their patient guidance and consistently helpful advice. Many thanks also to Drs. Tom Herbers, Jeff Paduan, and Ken Davidson for their support and feedback. I am also very grateful to Dr. Paduan and Dr. Wieslaw Maslowski for providing me with the additional work and funding that were essential to supporting my family while I completed this dissertation. I am further indebted to Jim Stockel for developing both ADCP and video data processing software and teaching me how to work with them, to Rob Wyland, Ron Cowen, and Keith Wyckoff for the many hours they spent installing, repairing, and maintaining the video equipment and ADCPs, to John Woods and Courtney Minetree for their assistance with the rip migration analysis, to Dr. Rikk Kvitek and Mr. Todd Hallenbeck of California State University, Monterey Bay for providing bathymetry data for southern Monterey Bay, and to Corey Olfe and Julie Thomas at CDIP for their prompt and friendly responses to my repeated requests for additional model output. Thanks also to reviewers R. Ranasinghe and R. Davidson-Arnott for their helpful comments and questions on the submitted first draft of the article that became Chapter II. Finally, I thank my wonderful wife, Nanette, and daughter, Audrey, for their love and support, which kept me going even when it all seemed an impossible dream.

THIS PAGE INTENTIONALLY LEFT BLANK

I. INTRODUCTION

The surf zone is a highly complex and dynamic physical environment in which a continuously changing spectrum of wind waves, swell, and longer timescale oscillations act to generate complicated flow fields, suspend and transport sediment, and reshape the beach and bathymetry. Despite this complexity, coherent and quasi-uniform patterns such as alongshore bars, rip channels, and beach cusps are often found at most coastal locations. Decades of research have gradually shed light on some of the many mysteries of the nearshore environment, but there are still innumerable questions remaining to be answered.

The present dissertation focuses on rip channels and beach megacusps, two related nearshore features that are commonly seen along the steep beach morphology of southern Monterey Bay, on the California coast (Fig. 1). Rip channels are cross-shore-oriented depressions created in a barred or terraced bathymetry by offshore-directed rip currents, which commonly occur when shoaling waves approach consistently normal to the shoreline. Megacusps are large, concave erosional patterns that sometimes develop on a beach in the presence of rip channel bathymetry and usually have alongshore spacing comparable to that of the rips.

The first of the two major sections of this study (Chapter II) addresses the alongshore migration of rip channels and its correlation with alongshore sediment transport. The principal hypothesis is that there is a linear relationship between alongshore migration and sediment transport rates, which are most strongly correlated at longer (seasonal and yearly) timescales. The investigation examines one to three years of time-averaged surf-zone video images from three sites along southern Monterey Bay, using them to track the alongshore positions of multiple rip channels over time. Wave data from offshore buoys are shoaled and refracted to the surf zone and used to estimate alongshore sediment transport rates for the same periods as the video data. Several different types of filtering techniques are applied to the estimated migration and transport

rate time series, which are then correlated at multiple timescales. The material contained in this chapter has been accepted for publication in the journal *Marine Geology* (Orzech, Thornton, MacMahan, O'Reilly, & Stanton, 2010).

The second major section (Chapter III) investigates basic questions about the formation of megacusps on rip channel bathymetry. The principal hypothesis is that megacusps can form shoreward of either rip channels or shoals, as determined by the combined effects of existing bathymetry shape, mean wave energy, and average tidal elevation. The analysis calibrates and evaluates the recently developed, depth-averaged coastal sediment transport model XBeach using measured data from Sand City, California, then applies the model to simulate both types of megacusp formation. Multiple examples of both "rip-opposite" and "shoal-opposite" megacusps are identified in time-averaged surf-zone video, and concurrent wave data are used to identify the climates associated with each megacusp type. The model is adapted to perform a process-based analysis of advective and diffusive sediment transport contributions for three selected cases, at two-hour-mean, very-low-frequency (VLF), and infragravity timescales. The material in this chapter will be submitted for publication to the journal *Coastal Engineering* by the end of May 2010.

II. ALONGSHORE RIP CHANNEL MIGRATION AND SEDIMENT TRANSPORT

A. INTRODUCTION

The causal relationship between nearshore flow processes and alongshore migration of rip channels is highly complex. Small-scale changes in rip channel morphologies that occur on hourly or daily timescales are too complicated to be well simulated at this time. At timescales of months to years, however, a quasi-linear relationship may develop in which seasonal variations in climatology become dominant and generate large scale, proportional shifts of rip channels. The subsequent analysis demonstrates this relationship by measuring rip migration and estimating concurrent alongshore sediment transport, exploring both shorter (tidal) and longer (seasonal) timescale trends and examining correlations. Rip channel migrations are measured with time-averaged video imaging techniques, while alongshore transport is estimated by transforming measured deep water wave spectra to shallow water using a spectral wave propagation model and then applying a standard bulk transport formulation. The analysis focuses on three sites in southern Monterey Bay, California (Fig. 2).

1. Rip Channel Migration

When incoming waves approach a barred beach from a near shore-normal direction, offshore-directed rip currents can develop and cut channels through the sandbar (Aagaard, Greenwood, & Nielsen, 1997; Brander & Short, 2001; MacMahan, Thornton, & Reniers, 2006). Shoreward of the bar, feeder currents converge into the rip from both sides, propelled by wave radiation stresses and alongshore setup gradients (Bowen, 1969). Offshore, channel flow diverges and weakens, forming a rip head that can extend beyond the outer surf zone. Rip channels on open coasts tend to occur simultaneously over relatively long stretches of beach with quasi-regular spacing. Herein, a grouping of similarly spaced rip channels over an alongshore distance of 1 to 2 km will be designated a “rip field.”

For the past two decades, rip channel location, width, and behavior have been measured using video imaging techniques introduced by Lippmann & Holman (1989). Because nearshore wave breaking is depth-dependent (Thornton & Guza, 1983), it tends to be concentrated over shallow-water shoals in the surf zone. In rectified, time-averaged (timex) surf-zone images, the regions of persistent wave breaking over shallow sandbars appear as white bands of surface foam. When rip channels are present, the white bands are interrupted by darker patches with little or no wave breaking, a consequence of the channels' greater depths. This makes it possible to trace the rip channels' subsurface locations by tracking variations in the intensity of image pixels (Lippmann & Holman, 1989; van Enckevort & Ruessink, 2001). The alongshore locations of intensity minima in the bar have been shown to correspond well with those of the underlying rip channels (Ranasinghe, Symonds, & Holman, 1999, Ranasinghe, Symonds, Black, & Holman, 2004).

Most rip channel research has focused on the wave conditions under which rips develop, while less has been done to analyze and model the alongshore motion of existing channels. Several studies have directly or indirectly monitored longer term rip motion in the field. Short (1985) described visual observations of rip locations for nineteen months along Narrabeen Beach, Australia. Ruessink, van Enckevort, Kingston, & Davidson (2000) measured the cross-shore and alongshore motion of crescentic bar systems on an open coast with rectified video images and cross-shore bathymetry profiles over a six-week period at Egmond, the Netherlands. They found that migration rates approached 100 m/day owing to large incident wave angles and that the rates were proportional to the alongshore component of the deep-water energy flux. Bogle, Bryan, Black, Hume, & Healy (2001) used rectified video images to track rip channel formation and evolution for 11 months at the 2 km pocket beach at Tairua, New Zealand and found a mean migration rate of 14 m/day averaged over selected storms. Rip channel migration speeds ranging from 2–20 m/day were measured using a four-year video data set at the 2.5 km embayed Palm Beach, Australia (Ranasinghe et al., 1999; Holman, Symonds, Thornton, & Ranasinghe, 2006). These authors noted that periods of high wave energy occasionally caused the rip channel bathymetry to "reset" itself, with all channels

disappearing for a period of hours to days and then re-emerging at different locations. The individual rip channels were found to persist an average of 46 days. In contrast, along the nearby, relatively long, straight Surfers Paradise Beach, rip channels migrated 5–50 m/day and persisted only eight days on average (Turner, White, Ruessink, & Ranasinghe, 2007).

Larger wave heights and more oblique angles of incidence, from either swell or locally generated wind waves, result in greater alongshore currents and rates of sediment transport (e.g., Komar, 1998). The relationship with rip channel migration appears to be more complex, particularly on hourly to daily timescales. Once a rip channel has been established, the morphology and flow dynamics tend to positively reinforce each other, leading to a relatively stable channel in a fixed location (Murray, 2004). Holman et al. (2006) find that eight-day average rip channel migration rates can be linearly related to predicted alongshore current velocities with $r^2 = 0.78$.

Few modelers have focused specifically on the propagation of rip channels and its dependence on alongshore sediment transport. A simplified view of these processes suggests that they should be linearly correlated, at least to first order (Fig. 3). Smit, Klein, & Stive (2003) found a direct relationship between wave incidence angle and rip migration direction using a process-based model with an idealized bathymetry. However, no attempt was made to physically verify this relationship with field data. Ruessink et al. (2000) used complex empirical orthogonal function analysis (CEOF) to calculate crescentic bar migration during six weeks at the Egmond site, but noted that such a procedure only works for relatively uniform wave conditions with regularly spaced rip channels. Klein & Schuttelaars (2006) modeled crescentic bar systems and found that rip migration rates correlated with the alongshore wavelength of the crescentic bars.

Herein, it is hypothesized that the alongshore migration rate of rip channels may be expressed as a linear function of the local alongshore sediment transport rate over longer timescales. Measuring this correlation requires accurate estimates of both migration rates and alongshore transport rates.

2. Alongshore Sediment Transport

Alongshore sediment transport has been analyzed and modeled for decades, and a variety of formulations have been developed to predict it. The bulk transport formula developed by the Coastal Engineering Research Center (CERC; U.S. Army Corps of Engineers, 2002) is among the earliest and most widely used. It provides a cross-shore- and depth-integrated estimate of the total alongshore sediment transport rate, q_s, based on alongshore wave momentum flux and requires only the cross-shore transport of alongshore wave-induced momentum (radiation stress), S_{yx}, and phase speed at breaking, C_b, as input parameters.

$$q_{s,CERC} = KS_{yx}C_b \tag{1}$$

where K is an empirical, dimensional constant.

In the following sections, the study site and methods are described, then results and correlations are presented and significant findings are discussed in greater detail. An error analysis is included in the appendix.

B. STUDY SITE AND INSTRUMENTATION

Monterey Bay, California, is an ideal location for the study of rip channels and associated beach processes (Thornton, Sallenger, & MacMahan, 2007). Waves refract over the Monterey Bay submarine canyon (Fig. 2) and consistently approach the shoreline from near shore-normal, resulting in year-round rip fields and relatively weak alongshore currents (typically < 0.5 m/s). For most of the year, deep water swell waves generally approach the Monterey Bay from the northwest, generated by the energy of western Pacific tropical cyclones in the summer and fall and northern Pacific storms in the winter. This pattern is episodically interrupted during the winter months, when larger tropical weather systems approach the California coast directly from the west. The one-year-return-period root-mean-square (RMS) wave height at breaking is approximately 3.5 m. There is an order of magnitude variation in wave energy along the shoreline, owing to wave refraction and sheltering by Pt. Piños headland. Mean rms breaking wave heights range from under 1 m at Monterey in the south to over 2 m near mid-bay. This creates a

concomitant variation in alongshore morphodynamic length scale, with rip channel spacing increasing from south to north (Thornton et al., 2007).

Along much of the shoreline, a steep (approximately 1:10) beach gradually curves out to a 1:100 low tide terrace, then steepens to about 1:20 offshore of the bar (MacMahan, Thornton, Stanton, & Reniers, 2005). Maximum tidal range is about ±1.5 m. Following the classification of Wright & Short (1984), the alongshore morphology is characterized as transverse-barred with regular incisions by rip channels. Alongshore rip spacing varies from approximately 100 to 500 m, and large-scale beach megacusps have comparable alongshore lengths. Mean grain size increases from 0.1 mm at the Monterey wharf to 0.4 mm north of Marina, with an additional ±0.05 to 0.1 mm variation across the surf zone at any given location.

Since 2001, the Naval Postgraduate School (NPS) has maintained several video camera towers continuously recording surf-zone images along the southern half of the Monterey Bay shoreline. The present study will analyze video data from sites at Sand City, the former Stilwell Hall (on Fort Ord), and Marina (Fig. 2). At each site, five-image datasets are produced every 20 minutes by Eltec "MiniHypercam" b/w video cameras, which internally process 800x600 pixel images at approximately 10 Hz to generate a time-exposure pixel intensity mean, a standard deviation, and a single snapshot, as well as images of maximum and minimum pixel intensity. Camera calibration, ground truthing, and image rectification procedures follow those outlined for Argus camera systems by Holland, Holman, Lippmann, Stanley, & Plant (1997). At Sand City, cross- and alongshore pixel resolution are about 0.5 and 11 m per pixel, respectively, at mid-range (400 m) from the camera tower and 1.0 and 19.8 m, respectively, at the alongshore edges of the view fields (750 m). At Stilwell and Marina, mid-range (500 m) resolution values are about 0.6 and 9.1 m, and long-range (1000 m) values are 1.3 and 29 m, respectively. The beach and nearshore topography along southern Monterey Bay has been extensively measured, providing detailed records that can be used to validate video-based morphology estimates.

Spectral wave data are available from several offshore buoys (National Oceanic and Atmospheric Administration, 2010a; Coastal Data Information Program, 2010). NPS

also operates acoustic Doppler current profilers (ADCPs) along the 13m depth contour offshore of the Sand City and Marina video towers. Each ADCP returns continuous 1 Hz time series of velocities over the water column and pressure.

C. METHODS

1. Tracking Rip Migration

Video images from three NPS cameras at Sand City, Stilwell, and Marina, are used to identify and track rip channel locations. The Sand City and Stilwell video datasets encompass three years (Nov 2004–Nov 2007), while the Marina images cover a single year (Jan 2007–Jan 2008). The measurement procedure followed here parallels that described by Holman et al. (2006). Rip locations are manually identified by visually selecting and marking off intensity minima on alongshore transects through the daily rectified timex images (see, for example, Fig. 4). The subjective error of this procedure was first estimated by having a 110-day section of video record (Stilwell, 2004–5) analyzed independently in this manner by Mark Orzech and Ed Thornton along with two graduate students (Table 1). The average user-associated RMS digitization error for rip locations marked by all four subjects ranged from 10.1 m near the cameras to 12.1 m near the far edges of the rectified images. Overall user-associated digitization error is estimated to be 11.5 m, which is essentially the same error found by Holman et al, (2006).

By recording channel positions from sequential, daily-averaged images, a timestack database is compiled for each site, tracking the development, migration, and extinction of rips in the field of view of the video cameras (Fig. 4). A representative migration rate for each date is obtained from each timestack by computing three-point slopes of each continuous rip location timeline on that date, then taking the ensemble average across the rip field of these rates of change. The alongshore averaging technique allows the varied motions of multiple rips to be represented by a single time series and also contributes to reducing subjective errors inherent in the rip-marking process (see appendix).

High waves, large incident angles, and strong alongshore currents can occasionally wipe out a rip channel bathymetry, completely filling in all channels. After a period of hours to days, the channels generally re-form, often in different locations. Such events are called resets and are identified in rip location time series where timelines break and/or shift dramatically alongshore (Fig. 5). Resets are relatively rare in Monterey Bay compared with previous investigations, occurring one to two times per year. Identification of resets with video is not always reliable, as reset periods tend to be associated with inclement conditions and more frequent video "whiteouts" due to heavy fog, rains and larger waves that break across the entire surf zone and obliterate the images of rip channels. An examination of offshore swell and local wind wave data for each reset period identified in Fig. 5 does not reveal any consistent conditions that might have led to the shifts. Relatively high, long-period waves (H_{rms} = 1.5–3.5 m; T_p > 15 s) do appear to be present during each reset. However, wave directions are inconsistent: three resets have wave approach angles from 0 – 3º south of shore normal, while one (Marina in December 2007) sees mean angles exceeding 7º south, and another (the Stilwell site in September 2007) has swell approaching from 3º north. Estimated alongshore transport forcing due to local wind waves is less than ten percent of that due to swell in all cases. The infrequent occurrence of resets in southern Monterey Bay likely results from the region's consistently small wave incident angles and associated weak alongshore currents, which are rarely strong enough to obliterate rip channels.

Alongshore flow in the surf zone may also include contributions driven by the shear of currents in deeper water, which are not included in the present analysis. Notably, mean alongshore velocities measured outside the surf zone by the Sand City ADCP can flow in the opposite direction of the predicted wave-induced alongshore current. Results from the one-month 2007 Rip Current EXperiment (RCEX) at Sand City indicate that alongshore flow in the surf zone can be composed of both wave-induced currents and contributions from other coastal circulations and eddies (Brown, 2009). The rip field reset observed at Sand City in December 2006 may have been partly due to unusually strong circulation patterns and higher transport rates resulting from these additional factors. Over the five days surrounding this reset event, ADCP-measured

alongshore currents in 13 m water depth at the site were strongly southward and up to an order of magnitude larger than model-predicted surf zone flows.

2. Modeling Alongshore Sediment Transport

Alongshore sediment transport rates are computed with the CERC formula (Eq. 1), using wave spectra measured at offshore wave buoys and transformed to shallow water with a wave refraction model. Before transport is computed, model wave output is first verified by comparison with in situ ADCP data over a shorter time period.

a. Wave Inputs

Because available ADCP wave data do not extend over the entire video measurement period, continuous time series are obtained at each site from a spectral wave refraction model (O'Reilly & Guza, 1993) operated by the Coastal Data Information Program (CDIP) at U.C. San Diego. Initialized by directional wave spectra measured at multiple offshore buoys, the CDIP model generates hourly estimates of nearshore wave frequency spectra and directional moments together with significant wave height ($H_s = \sqrt{2}H_{rms}$) and both peak and mean values of wave period and direction (Coastal Data Information Program, 2010). Because of the nearly shore-normal wave approach along the Monterey Bay shoreline, small errors in estimated shoreline orientation can significantly affect the magnitude and direction of calculated alongshore transport (see Appendix). In this analysis, CDIP-predicted wave information is used in the transport computations, and shore-normal angles are estimated from the orientations of beach contours measured in recent shoreline surveys conducted using an all-terrain vehicle (ATV) equipped with a global positioning system (GPS) (Thornton et al, 2007).

Sixteen months of data from the Sand City ADCP, deployed in approximately 13 m depth, are used to assess the accuracy of wave model predictions. Processed ADCP output includes hourly frequency-directional spectra from which S_{yx}, wave height, period, and direction can be extracted. CDIP model wave output in 15 m water depth is further shoaled and refracted to 13 m where the ADCPs are located, assuming alongshore uniform bathymetry. The CDIP model comparisons with in situ

ADCP wave data at Sand City are summarized in Fig. 6. Correlation of wave heights is good, with an almost 1:1 ratio between predicted and measured values. In contrast, predicted (energy-weighted) mean directions correlate less well with ADCP values. This is not unexpected, because the (measured and modeled) mean directions at Sand City only vary by about 10º, which is just slightly larger than the noise in the ADCP mean direction estimates. However, modeled radiation stress values, S_{yx}, used in the sediment transport predictions correlate well with ADCP-initialized predictions (Fig. 6, lower left), with a coefficient of 0.94. Comparisons with the ADCP at the Marina site (not shown) follow a similar pattern.

b. CERC Formula Estimates

Alongshore sediment transport estimates are computed using the CERC formula (Eq. 1), initialized at 15 m depth with CDIP wave data. S_{yx} is conserved from 15 m depth to breaking depth over assumed straight and parallel contours. The total S_{yx} is obtained as the sum over the sea-swell band of frequencies (0.04–0.25 Hz) of contributions at each frequency $S_{yx}(f)$, which are computed from the product of wave energy spectrum $E(f)$, second directional moment $b_2(f) = \int_0^{2\pi} S(f,\alpha)\sin 2\alpha d\alpha$ (where $S(f,\alpha)$ is the frequency-directional spectrum and α is wave incident angle), and the ratio of group to phase speed $n(f)$, using linear wave theory:

$$q_{s,CERC} = KS_{yx}C_b = K\left[\frac{1}{4}\rho g \int_{0.04}^{0.25} E(f)b_2(f)n(f)df\right]_{15m} C_b \qquad (2)$$

The subscript "15m" indicates that these quantities are evaluated offshore, at 15 m depth. Using shallow water wave theory, $C_b = \sqrt{gh_b}$, where breaking depth h_b is determined using the method of Dean & Dalrymple (1984) by iteratively shoaling and refracting input waves, assuming alongshore uniform bathymetry. Empirical coefficient K is set to 0.147 m^3/hour per Joule/(m·s), as recommended by the Shore Protection Manual (U.S. Army Corps of Engineers, 2002). Fixed, site-specific reduction factors of 0.5, 0.375, and 0.25 are applied to calculated transport rates at Sand City, Stilwell, and

Marina, based on results from Zyserman & Fredsøe (1988) in which alongshore sediment transport is found to significantly decrease as the spacing between rip channels narrows. This alters transport magnitudes only and does not affect correlations with rip migration rates. Hourly values are summed over each day to obtain daily transport rates. As might be expected from the earlier S_{yx} comparisons, the correlations of CERC-based sediment transport rates with ADCP-based values at Sand City are high (r = 0.94; Fig. 6, lower right panel).

D. RESULTS AND DISCUSSION

Daily RMS rip migration rates are calculated for the entire rip field at each of the three sites (Table 2, Column 1). Rip channels at Sand City have a three-year-mean RMS migration of 5.8 m/day, while those at Stilwell average 6.7 m/day over the same period. Marina's rips have the largest mean RMS migration rate, 9.0 m/day, over their single recorded year. Modal daily RMS migration rates at Sand City, Stilwell, and Marina were 4.5, 4.5, and 7.5 m/day, and maximum RMS rates were 18, 22, and 30 m/day, respectively. Migration rates are mostly northward at Sand City and southward at Stilwell and Marina.

The ranges of absolute sediment transport rates predicted by the CERC formulation at each site are shown in Table 2, Column 2. Trends seen in transport magnitudes among the sites are similar to those seen with RMS migration rates and are a result of the variations in wave energy and shoreline orientation along the coast of southern Monterey Bay. Sheltered Sand City in the south has the lowest estimated mean transport magnitude of 68 m^3/day as well as the lowest maximum transport, and transport is skewed heavily northward owing to the shoreline orientation relative to typical westerly wave approach. The middle site, Stilwell, has a maximum estimated transport rate nine times larger than Sand City and a mean transport magnitude of 200 m^3/day. The greatest single-day transport rate, nearly 23,000 m^3/day, occurred at the northernmost site, Marina, which has a predicted mean transport magnitude more than double that of Stilwell. While overall transport at Stilwell trends slightly southward, at Marina the north-south sediment balance is almost zero.

Because the mean RMS migration values are smaller than the digitization error of 11.5 m, an analysis is performed to determine whether daily migration rates are distinguishable above the noise floor resulting from the rip identification process (similar to Holman et al., 2006). Using the methods outlined in Section IIC, daily RMS migration rates are computed from 10 synthetic Gaussian noise time series with zero mean and RMS values equal to our digitization error. The mean RMS migration rate for the synthetic data is roughly 8.5 m/day, which is of the same order as the measured RMS daily rates given above. One-day migration rates will thus generally be difficult to distinguish from digitization noise at all three sites. As would be expected, correlations with CERC formula daily sediment transport rates are consequently poor: daily correlation coefficients are r=0.01, 0.44, and 0.38 at Sand City, Stilwell, and Marina, respectively (Table 2, Column 3).

1. Extended CERC Formulation

Sand City often features significant alongshore wave height gradients (Fig. 7), owing to strong refraction and sheltering by Point Piños (Fig. 2). The original CERC formulation (Eq. 1 and 2) implicitly neglects the resultant forcing due to variations in wave setup $\bar{\eta}$ (alongshore pressure gradients) and radiation stress component S_{yy}, which oppose and balance each other outside the surf zone but combine in shallower water to modify the alongshore flow (Bowen, 1969; Keeley & Bowen, 1977). To examine if including transport forcing by these gradients might improve comparisons, an extended version of the CERC formulation is applied at Sand City. In the extended CERC formula (Ozasa & Brampton, 1980; List, Hanes, & Ruggiero, 2007), a second term is added to account for transport forced by alongshore wave height gradients:

$$q_{s,CERCex} = KS_{yx}C_b + \frac{K_2 H_{rms,b}^{5/2}}{\beta}\cos(\alpha_b)\left(-\frac{\partial H_{rms,b}}{\partial y}\right) \qquad (3)$$

where K_2 is a semi-empirical function of sediment density and porosity, $H_{rms,b}$ is the RMS wave height at breaking, β is the average beach slope across the surf zone, and α_b is wave incident angle at breaking.

Alongshore wave height gradient $\partial H_{rms,b} / \partial y$ is estimated at Sand City by dividing the difference between CDIP-predicted H_{rms} values at Sand City and Stilwell by 4000 m (Fig. 7). An example of the relative distribution of transport rates due to the additional forcing, as well as its effect on the overall transport rate distribution at Sand City, is provided in Fig. 8. Calculated alongshore transport due to wave height gradients at the site is up to 20% of that obtained for radiation stresses alone and is always to the south. However, the mean of the $\partial H / \partial y$ CERC contribution (1 cu m/day) is only 5% of the mean of the original CERC rates (-20 cu m/day) (Fig. 8). With the expanded transport formulation, the daily migration-transport correlation coefficient for periods excluding resets remains just 0.01. For this reason, the expanded formulation is rejected; all reported sediment transport estimates are based on the original CERC formula.

2. Noise Filtering Techniques

To resolve the noise problem described above, four different filtering techniques are used that examine rate correlations from different perspectives. First, a simple running average technique is applied to compute migration and transport rates over a longer time step that exceeds the noise floor. Second, a low-pass filter with varying cut-off frequencies is applied to the complete time series of mean daily migration and transport at each site to remove high frequency noise effects and focus on longer-term trends. Third, correlations are performed only including days with the highest 10% of transport rates for each site, anticipating that there is a threshold of transport required to initiate rip channel migration. Fourth, daily rates are cumulatively summed, a method which is shown to be equivalent to applying a graduated low-pass filter that also damps high frequency noise and emphasizes seasonal oscillations. In all cases, reset events are excluded from the analysis. This four-part analysis is followed by a brief discussion of the anomalous Sand City site, an idealized migration-transport relationship, and tidal signatures in rip migration.

a. Time-Averaged Filtering

Uncertainty in the measured migration rates is reduced by averaging the daily rates over longer intervals (in a manner similar to Holman et al., 2006). It is determined that eight-day-averaged rates are required for migration values to be well distinguished from digitization noise error. For eight-day averaged synthetic Gaussian migration time series, the RMS migration rate is determined to be approximately 1.4 m/day, with a 95% exceedance value of 2.2 m/day. For inter-reset periods, the eight-day averaged RMS rip migration rates range from 2.2 m/day at Sand City to 4.7 m/day at Marina, all of which are at or above the 95% confidence limit for the synthetic noise. For all days and all sites combined, 60% of eight-day mean migration rate magnitudes exceed the corresponding eight-day RMS noise rate. The correlations of CERC-estimated eight-day-averaged transport rates with the corresponding rip migration rates for inter-reset periods are listed for each site in Table 2, Column 4. At the anomalous Sand City site, despite the longer averaging periods, the correlation of migration and CERC model transport rates is still only 0.06. Nearly all calculated mean daily sediment transport rates are directed northward at this location (skewness of rates = -3.3; see Fig. 8), while in contrast, 41% of daily mean migration rates are toward the south and migration rates have a slightly southward skewness (+0.07). At the more exposed Stilwell site, a higher correlation, r=0.60, was found between daily eight-day-averaged sediment transport and rip migration rates. Alongshore transport rates for the single recorded year at Marina have a similar correlation, 0.58.

b. Low-Pass Filtering

A generalization of time averaging is examined by applying a fourth-order Butterworth, zero phase-shift, time-domain low-pass filter to the rip migration and CERC model sediment transport rate time series, and then recomputing the correlations. Filtering out frequencies above 1/(8 days) only increases the inter-reset time series correlation for daily rates at Sand City to r=0.06, confirming the anomalous nature of the site. In contrast, it significantly improves them to r=0.66 at Stilwell, and r=0.60 at Marina (Table 2, Column 5). As an example, pre- and post-filter time series are

compared for the Stilwell site in Fig. 9. Correlation values for low-pass-filtered migration and transport rates at each site are plotted against cut-off filter frequency in Fig. 10, with cutoff frequencies ranging from 1/(360 days) to 1/(5 days). As expected, *r* generally increases as more high frequency energy is excluded (though correlations at Sand City only reach 0.33). The highest correlations are found at 1/(360 days) for the three-year dataset at Sand City, at 1/(90 days) for Stilwell and close to 1/(25 days) for the shorter, one-year Marina time series. The maxima do not always occur at the yearly frequency because of the datasets' relatively short length and the skewed nature of the data, in which most of the migration occurs over three winter months.

c. High-Energy Filtering

An examination of daily rip migration and sediment transport rate time series suggests that migration may lag behind transport, particularly during the milder spring and summer wave climate at the Stilwell and Marina sites. In general, a gradual southward sand transport begins in the early spring at both sites but is initially accompanied by little or no southward rip migration until later in the summer. At the Stilwell site from July-September in 2005 and 2006, daily rip migration rates are near zero (Fig. 9, upper panels), while calculated daily sand transport rates average about 200 m^3/day toward the south. At the end of these periods, however, daily rates jump to 500 and then 800 m^3/day southward, coincident with the sudden shifts to higher rip migration rates in the same direction. At Sand City, calculated mean sand transport is 75 m^3/day for the same slow periods, after which it abruptly doubles to over 150 m^3/day. At the Marina site in 2007, estimated sand transport averages around 400 m^3/day for July to early September, then spikes to 1600 m^3/day in early September and October, at roughly the same time as daily migration rates begin to surpass 10 m/day.

These results suggest that there may be a critical alongshore sand transport rate for initiation of measurable alongshore rip migration that is usually not produced by the smaller summer waves in Monterey Bay. However, this rate is most probably site-specific and dependent on additional factors such as rip channel spacing, grain size, and beach slope. For exposed sites like Stilwell and Marina, the critical transport rate appears

to be approximately 500–1000 m^3/day, but at sheltered Sand City it may be significantly less owing to the finer sand size. Rip channel spacing clearly plays a role in determining its estimated value (via the transport reductions mentioned in Section IIC).

If such a critical alongshore transport rate exists, correlations that included only higher energy days would be significantly better than those for the entire migration and transport dataset for a given location. To test this, the original migration and transport rate datasets are restricted to days with the highest 10% of alongshore transport rate magnitudes at each site (i.e., greater than 130 m^3/day at Sand City and 800 m^3/day at Stilwell and Marina). Relative to the original time series, correlations for the limited datasets increase to r=0.23 at Sand City, r=0.66 at Stilwell and r=0.54 at Marina (Table 2, Column 6).

d. Cumulative Summing

Cumulatively summed daily migration rates are next compared with cumulatively summed net transport rates for inter-reset periods at each site. The summed migration rates represent the average displacement of all the rips in a rip field from their most recent post-reset positions at a given time (i.e., mean migration distance), while the summed transport rates provide an estimate of the net amount of sediment that has moved past an arbitrary cross-shore transect at the measurement site since the last reset event (i.e., net alongshore transport).

The summing process is equivalent to a low-pass filter, as may be illustrated by representing rate data as a Fourier series, $q_s = A_0 + \sum_{n=1} A_n \cos(n\omega_1 t - \varphi_n)$, in which φ_n is the phase of the sinusoidal component at frequency $n\omega_1$ with amplitude A_n, and the constant term A_0 represents the mean migration or transport rate. Integrated (i.e., summed) over time,

$$Q_s = \int q_s dt = A_0 t + \sum_{n=1} \frac{A_n}{n\omega_1} \sin(n\omega_1 t - \varphi_n) \qquad (4)$$

The lower frequencies ($n\omega_1 < 1$) are amplified by the factor $1/n\omega_1$ while the higher frequencies ($n\omega_1 > 1$, corresponding to periods less than 6.28 days) are increasingly

damped. Cumulative sums of migration and transport rates thus damp high frequency noise and emphasize longer-period, well-correlated seasonal trends. When Eq. 4 is applied to rate data from the Stilwell site, yearly oscillations are amplified over 200 times by the filtering process relative to single-day cycles, while monthly oscillations are amplified 30 times. The integrated total Q_s now also includes a linearly increasing component A_0t that, if nonzero, will accumulate with time and ultimately outpace all oscillatory contributions. As will be seen below, this linear trend can have a strong influence on correlations of cumulatively summed data.

Summed mean migration distances (for inter-reset periods) are plotted together with summed net sediment transport in Fig. 11, with a separate panel for each site. The calculated net transport generally follows the mean rip migration. The seasonal signatures of large scale climate forcing are clearly visible in the mean migration and net transport patterns of Fig. 11, particularly for the more westward facing Stilwell and Marina sites. At Stilwell (with a shore normal of 290º), a gradual southward transport and migration in the spring and summer months accelerates in the fall as larger northern swell begin to arrive. This trend is sharply reversed in November to January of each year by intense, relatively short-term migrations toward the north, forced by the large, storm-generated western swell that impinge on the coastline with a southerly approach angle (Fig. 12). At Marina (shore normal 278º), a very similar pattern was recorded for 2007, marked by an extremely sharp northward reversal in early December that coincided with the arrival of an intense winter storm out of the west. In contrast, Sand City's northwestward-facing shoreline (shore normal 310º) is subject to an almost year-round *southerly* approach angle for incident waves and a consistent northward mean flow along the shoreline. Only in the fall and early winter months is the northward trend briefly reversed by the arrival of large northern Pacific swell. (See the appendix for discussion of wave directional errors and the lack of seasonal transport patterns at Sand City.)

At Sand City, cumulative migration and net transport are both heavily biased northward, and seasonal trends are missing from the calculated sediment transport record. At the Stilwell and Marina sites, transport directions are more balanced, with clearer seasonal variations. The maximum rip field displacement between resets is 400 m

(northward) at Sand City, but only 200–300 m (southward) at Stilwell and Marina. In contrast, the net transport for the period at Sand City (3.3×10^4 m^3) is significantly less than values for Stilwell (5×10^4 m^3) and Marina (10^5 m^3). The pronounced seasonal variations in cumulative migration and net transport that occurred in 2004–2005 at Stilwell are significantly milder for 2006–2007. This seasonal variation is prominent in the 2007 cumulative migration record at Marina but less apparent in the calculated net transport. The lag of mean rip migration behind net sediment transport that was described in the preceding section is visible on Fig. 11 in the summer and fall of each year, most clearly at Stilwell and Marina. It also introduces an offset in the linear best-fit line plotted for those sites in Fig. 13.

Correlations of mean rip migration and calculated net sediment transport for inter-reset periods are higher than those obtained by any of the three preceding filtering methods (Table 2, Column 7). Correlation coefficient *r* reaches 0.94 at Sand City, 0.76 at Stilwell, and 0.87 at Marina. The high correlation at Sand City is initially surprising, given the poor comparison of other filtered migration and sediment transport rates relative to the other two sites. However, further examination shows the result to be heavily influenced by the strong northward trends of migration and transport at this southernmost site. When the linear trend is removed from both mean migration and net transport time series, *r* drops to 0.18 at Sand City, while detrended values at Stilwell (r=0.62) and Marina (r=0.34) are less severely affected.

The high correlation of mean rip channel migration with net alongshore sediment transport calculated with the CERC formula corresponds to previous results. Holman et al. (2006) found high correlation with a proxy of alongshore current proportional to $H^{1/2}\sin 2\alpha$, which is similar to the $b_2(f)$ input to the radiation stress used in the CERC formulation, and Ruessink et al. (2000) found migration proportional to alongshore wave power, which is implicit in the CERC formulation.

It should be noted that correlation values from the low-pass filter imposed by cumulative summing are larger than the corresponding Butterworth-low-pass-filtered maxima shown in Fig. 10, because the summing process includes some contributions

from every frequency component. These results support the existence of a fundamental connection between migration and transport at seasonal timescales.

3. Anomalous Sand City

Although an exhaustive investigation is beyond the scope of the present analysis, it seems appropriate to suggest reasons for the anomalously poor correlation results at the Sand City site. In the author's view, the mismatch between transport and migration is most likely due to site-specific measurement errors, the effects of neglected local shoreline irregularities, and the site's unusual wave characteristics. Measurement errors, including outdated bathymetries and incorrect estimates of shoreline orientation, are discussed further in the appendix. An important break in the shoreline occurs at Tioga Avenue, 400 m north of the Sand City site, where large amounts of concrete and other construction materials have been dumped onto the beach and surf zone. It is probable that the resulting mini-peninsula blocks at least some southward transport toward the Sand City site, which reduces the seasonal southward rip migration shown in the top panel of Fig. 9 relative to the other two sites and may also act to focus or reflect shoaling waves. There is a storm drain outfall 50 m south of the Sand City camera tower, which scours a channel into the beach face each winter and contributes additional sediment to the surf zone. Finally, the Sand City location features both a significant alongshore wave height gradient and generally lower wave energies than are found farther north. As shown in this study, the inclusion of $\partial H/\partial y$ in the expanded CERC formula can change alongshore transport rates by up to 20%; however, a true estimate of its effects may require a more accurate local gradient rather than the large-scale average used here. The Sand City site's milder wave climate results in correspondingly slower bathymetric change. Video-estimated rip migration rates are closer to the noise floor than at Stilwell and Marina and thus also more likely to be obscured.

4. The Migration-Transport Relationship

A highly simplified picture of migrating rip channels is presented in Fig. 14 to illustrate the quasi-linear relationship between alongshore transport and rip migration. For such an idealized rip field, a mean migration of, say, Δy = 10 m to the south can most

simply be represented as a translation of each rip channel by 10 m in that direction. The associated net transport must fill in the northern side of each channel while removing sand from its southern side. This would most likely result from a southward-flowing alongshore current. Conservation of mass dictates that flow traveling southward from a shoal into a deeper rip will slow down, dropping some of its sediment load along the northern edge of the rip. Upon reaching the rip's southern edge, the flow must then accelerate onto the shoal, suspending and removing sediment. Over the longer term, these variations will reshape the rip channel and shift it southward.

In this scenario, neglecting other sources, the volume of transported sediment over a given period will be directly proportional to the volume of each rip channel, and the channel migration rate will be linearly related to the alongshore transport rate. Assuming an average surf-zone width of 100 m and mean rip channel depth of 2 m, comparable to values seen in southern Monterey Bay, a rip migration rate of 1 m/day would require a sediment transport rate of at least 200 m^3/day. An overall migration of 200 m will thus need a net sediment transport volume of at least 4 x 10^4 m^3. Despite a highly simplified analysis, this estimate is of the same order as those obtained in southern Monterey Bay using more complex alongshore transport formulations and recorded wave data (Fig. 9). The idealized estimate above assumes that all transported sediment is used to enable rip migration, while in reality a portion of such sediment might also come from regions between rips, and much of it will bypass a number of channels before finally settling to the bed.

5. Tidal Effects on Migration

Rip migration processes on weekly to monthly timescales are investigated by examining energy density spectra. Migration rate time series for selected inter-reset periods are divided into linearly detrended ensembles of 56 days (Sand City and Stilwell) and 28 days (Marina), overlapped by 50%. The length of the time series was chosen to minimize spectral leakage at the hypothesized fortnightly spring-neap tidal cycles. Spectra of rip migration rates at the three sites are plotted versus frequency for oscillatory periods exceeding 2.5 days in Fig. 15. The spectral noise floor is indicated (assuming

white noise variance for the synthetic mean RMS migration rate described at the beginning of Section IID), and is not significant. For the three-year dataset at Stilwell, a peak occurs for a period of 28 days that is significant to at least 80 percent confidence, suggesting that the lunar tidal cycle may have an effect on alongshore sediment flows and accompanying rip migration rates. The three-year Sand City and one-year Marina datasets both feature a peak near 0.073 $days^{-1}$, corresponding to a period of approximately 14 days. A less significant spectral peak is also visible close to 1/(7 days) for the two southern locations, possibly indicating that the 14- and 28-day cycles are in-phase harmonics resulting from an asymmetric system response.

These results suggest that there may be enhanced migration at times when the tidal range is greatest, and both the highest and lowest portions of the beach are subjected to more intense wave breaking and increased sediment suspension. Tidal signatures similar to these are commonly detected in measurements of alongshore currents (e.g., Thornton & Kim, 1993). Alongshore flows tend to be weak or nonexistent during lower tides but become stronger at higher tides (Brown, 2009), and stronger currents also appear to be associated with greater rip migration (e.g., Holman et al., 2006). Field measurements on a macrotidal beach suggest that sediment suspension can be enhanced due to increased bed roughness during falling tides (Masselink & Pattiaratchi, 2000) and tidally generated fluctuations in the beach groundwater table (Masselink & Turner, 1999).

E. SUMMARY AND CONCLUSIONS

Rip migration measurements and CERC model alongshore transport estimates are correlated to test the hypothesis that the alongshore migration rate of rip channels may be expressed as a linear function of the local alongshore sediment transport rate over longer timescales. Daily rip channel locations are determined from time-lapse video images at three sites along southern Monterey Bay for periods of one to three years, and daily migration rates (averaged over all rips in the rip field) are computed. The video digitization error is estimated to be 11.5 m by having four individuals identify rips on a 110-day record. The performance of the CDIP spectral wave propagation model is

validated by comparison with nearshore ADCP measurements, and model-predicted radiation stresses, S_{yx}, achieve a correlation of r=0.94 with S_{yx} values computed from ADCP data at Sand City. For each site, the CDIP model is then used to refract measured offshore waves into the surf zone, where the CERC formula is applied to generate estimates of alongshore sediment transport rates. An expanded CERC transport formulation that also includes effects of alongshore wave height gradients is applied to the Sand City site, where such gradients are significant.

A parallel simulation conducted with random Gaussian time series indicates that daily rip migration rates will not generally be distinguishable above the noise associated with digitization. Correlations of daily migration and transport rates are indeed relatively low, so several alternative filtering methods are used to compare them in ways that will overcome the noise barrier. Correlations using an expanded CERC model that includes forcing by alongshore wave height gradients to calculate transport at Sand City are little changed from the standard CERC-predicted values, so that formulation is excluded from further consideration. Gaussian-noise simulations identify a minimum time step of approximately 8 days, below which averaged rip migration rate data will likely be indistinguishable from digitization noise. Rip migration and sediment transport rates averaged over 8 days attain correlation coefficients 50–100% higher than those found with daily rates. Low-pass filtering with a cutoff frequency of 1/(8 days) gives coefficient values slightly better than those from eight-day-averaged rates at each site. Correlating only the 10% of days with the highest transport rates significantly improves upon daily correlation results at Sand City as well as at Stilwell and Marina. Cumulatively summed rates result in nearly doubled correlation values relative to daily rates. Correlations at the Sand City site remain anomalously low for all filtering methods except cumulative summing.

Results obtained with each filtering method provide insight into the nature of the migration-transport relationship. The moderate increases in correlation values obtained with eight-day-averaged migration and transport rates emphasize the challenges of accurately representing complex nearshore processes, even after data are filtered. The low-pass filtering analysis highlights important longer-period oscillations (such as tidal

and seasonal cycles) that might influence alongshore rip migration patterns. Improved correlations of daily rates obtained under higher energy conditions suggest that there may be a limited range of conditions over which a linear relationship applies. Cumulatively summed migration and transport rates can be used to track the mean migration of each rip field and the net amount of sediment transported north or south along the beach at each site. Plots of these quantities suggest that rip migration might lag behind sediment transport, particularly in milder summer months when the minimum energy and transport levels necessary for migration may not be attained by the smaller waves. On the basis of the high correlations obtained between cumulatively summed migration and transport rates, it is concluded that the alongshore migration rate of rip channels may be expressed as a linear function of the local alongshore sediment transport rate over longer timescales.

III. MEGACUSPS ON RIP CHANNEL BATHYMETRY

A. INTRODUCTION

Rip channels are cross-shore-oriented depressions that can develop in the surf-zone region of a barred or terraced bathymetry, when near shore-normal waves generate offshore-directed rip currents (Aagaard et al., 1997; Brander & Short, 2001; MacMahan et al., 2006). Closer to shore, feeder currents develop that converge into the rip from both sides, forced by wave radiation stresses and alongshore setup pressure gradients (Bowen, 1969). Rip channels on open coasts tend to occur simultaneously over relatively long stretches of beach with quasi-regular spacing.

Beach cusps are crescent-shaped, concave indentations in the beach face that are a common sight along many coastlines. Smaller "swash" cusps can appear on almost any beach and generally have cross-shore widths of around 5 – 10 m and alongshore wavelengths ranging from 10 – 50 m. When rip channels are present, larger megacusps can form with wavelengths of 100 – 500 m that approximately match the alongshore spacing of the rips (Thornton et al., 2007). Rip channel and megacusp location, size, and behavior can be measured on site with GPS-based survey equipment, but complete surveys are time-intensive, costly, and consequently less frequent. When cameras are available, adequate estimates of shapes and sizes can often be obtained using video imaging and rectification techniques (Lippmann & Holman, 1989).

Most visual evidence suggests that megacusp embayments are aligned with rip channels (e.g., Fig. 1b). Thornton et al. (2007) found a significant but fairly low correlation ($r^2 = 0.35$) between surveyed rip channel and megacusp locations along 18km of the southern Monterey Bay shoreline. The maximum cross-correlation corresponded to a near zero lag value, implying alignment of rip channels and megacusp embayments. Its low value was explained by noting that the two surveys were conducted 21 days apart, and that this level of decorrelation would be expected for these data if rip channels and megacusps were assumed to act independently with time. Other, more closely spaced surveys were not available. The role of rip channel bathymetry in the development of

beach megacusps has not been investigated in depth in the field. Short (1979) hypothesized that megacusps may be either erosional or depositional features of rip currents, but field measurements of swash flow in this region have been too limited to confirm or refute this theory.

Greater progress has been made in modeling megacusp formation processes. Alongshore- and depth-averaged one-dimensional (1D) models that have been applied to the problem allow for changes in shoreline position but can only crudely account for alongshore differences (e.g., Edelman, 1968; Nishi & Kraus, 1996). Cross-shore- and depth-averaged 1D "line" models used in instability analyses have predicted the development of cusp-like shoreline features; however, they give little or no information about how shoreline erosion and accretion patterns are distributed across the width of the beach face (e.g., Falques & Calvete, 2005; Horikawa, 1988; Komar, 1998). Some two-dimensional (2D) models have proven effective in predicting nearshore circulations including rip channels (e.g., Reniers, Thornton, & Roelvink, 2004; Calvete, Dodd, Falques, & van Leeuwen, 2005), but they have generally worked with a fixed boundary for the shoreline. Several 2D studies have measured or modeled a surf-zone counter-circulation on the shoreward end of a rip channel and suggested that it may play a role in creating megacusp embayments (Haller, Dalrymple, & Svendsen, 2002; Calvete et al., 2005; MacMahan, Thornton, Reniers, Stanton, & Symonds, 2008). Models combining alongshore and cross-shore variability with an adjustable shoreline position have largely not been tested owing to the significantly increased complexity of the problem.

The formation of megacusps occurs over timescales on the order of hours to days, while the principal wave-generated forcing periods range from seconds (wind waves, $f \sim 0.1Hz$) and minutes (infragravity and edge waves, $f \sim 0.004 - 0.04Hz$) to somewhat less than an hour (very-low-frequency, VLF, waves, $f \sim 0.0005 - 0.004Hz$). Roelvink & Stive (1989) decomposed the near-bed flow field into mean, wave-group, and short wave frequency components, $u = \bar{u} + \tilde{u}_L + \tilde{u}_S$, then expanded different velocity moment expressions to investigate the flow and cross-shore sediment transport contributions due to wave asymmetry and the interaction of short-wave variance with

long-wave velocities. Thornton, Humiston, & Birkemeier (1996) used a similar technique with field data from Duck, NC, to investigate the principal processes involved in generating a bar/trough beach profile and to predict cross-shore bar migration. They concluded that the mean components contributed half of all surf-zone sediment transport, with the largest contribution coming from the alongshore current. Using a later dataset from the same site, Gallagher, Elgar, & Guza (1998) also found mean transport components to be dominant, but found that transport due to the undertow (cross-shore mean flow) played the biggest role. Reniers et al. (2004) found that intersecting trains of wave groups can force large-scale horizontal eddies in the surf zone with timescales in the VLF range and length scales the order of the surf zone width. Although sufficient field data are not available to perform such a frequency-based study for a megacusp formation event, it is possible to use a calibrated nearshore model to perform a process-based analysis of sediment transport forcing at these different frequency ranges.

The present analysis focuses on megacusp formation in the presence of rip channels under different wave and tidal conditions, utilizing both field data and modeling simulations. It is hypothesized that the sizes and locations of the megacusps in Monterey Bay are determined by the morphodynamic interactions between the shoaling waves and the local rip channel bathymetry, and that daily mean water level plays a key role in determining when and where megacusps form on a given beach. The following section includes a description of the study site and an examination of available field data. Section IIIC begins with a summary of relevant model theory, which is followed by model calibration and testing, and then a series of simulations in which two distinct types of megacusps are generated. In Section IIID, sediment transport processes for three selected cases of megacusp formation are decomposed to two-hour-mean, VLF, and infragravity timescales and examined individually to identify dominant contributions.

B. FIELD DATA

1. Study Site

The study is limited to wave conditions and rip channel bathymetry similar to those found along the shoreline of southern Monterey Bay, California (Fig. 2). Swell

waves approaching the bay are refracted over the submarine canyon and consistently arrive at the shoreline with a near shore-normal direction. As a result, alongshore currents are generally weak (usually < 0.5 m/s), and rip channel bathymetry is usually present, except possibly during extreme storm events. The maximum offshore significant wave height is expected to be 5 m (one-year return period) or greater, and the tidal range can be as large as ±1.5 m. Because of wave refraction and sheltering by Pt. Piños headland, there is an order of magnitude variation in wave energy and morphodynamic scale from south to north along the bay. Mean grain size increases gradually from about 0.1mm at the Monterey wharf to 0.4 mm north of Marina, varying by an additional ±0.05 to 0.1 mm across the surf zone. Rip channel spacing and alongshore megacusp wavelengths also increase as one travels northward, from approximately 100 m at Monterey to 500 m near the Salinas River. The steep (approximately 1:10) beach extends onto a 1:100 low tide terrace, which steepens to about 1:20 (MacMahan et al., 2005), and then gradually tapers to 1:50 for depths greater than 10 m.

The following analysis focuses on Sand City, where shoaling waves and currents are continuously monitored by three shoreline video cameras and an acoustic Doppler current profiler (ADCP) deployed offshore at 13 m depth. Several multi-investigator surf-zone experiments have been conducted at the site (MacMahan et al., 2005; Brown, MacMahan, Reniers, & Thornton, 2009), providing high resolution bathymetry data from a number of surveys conducted with geographic-positioning-system (GPS)-equipped personal watercraft (PWC) and backpack. Offshore wave data are also available from buoys maintained by NOAA (National Oceanic and Atmospheric Administration, 2010a).

2. Sand City Measurements

The Sand City ADCP and video datasets provide qualitative insight into megacusp formation. ADCP pressure and velocity data are combined to generate directional wave spectra, from which basic wave properties including significant wave height, peak period, and direction can be determined. Surf-zone video images from the three Sand City cameras are first calibrated and rectified to plan view using ARGUS system techniques (Holland et al., 1997). In the rectified, time-averaged surf-zone

images, deeper rip channels appear as darker patches while shallower shoals show up as white regions owing to persistent foam from wave breaking. The alignment of these features with the underlying bathymetry was confirmed by Ranasinghe et al. (1999, 2004) and is visually apparent when measured bathymetry contours are plotted over video images (Fig. 16). The approximate shoreline contour can often also be detected as a white line of foam running between the surf zone and the (usually darker) beach face.

By combining rectified video images with measured wave data, it is possible to identify megacusp formation events and track the types of waves that tend to create them (e.g., Fig. 17). Reviewing daily video datasets recorded at the Sand City site over a 50-month period from 2005–2009, the author visually identified 26 megacusp formation events, in which a previously straight shoreline evolved into one with megacusps. The majority (20) of these megacusp formation events result in "rip-opposite" (RO) megacusps, with embayments shoreward of the rip channels, and usually coincide with narrower neap tidal ranges, when mean daily water levels are close to MSL. Maximum H_s values for these events reach 1.5 – 2 m and T_p ranges from 10 – 12 s. The RO megacusp contours appear widest at mean sea level (MSL) and narrower at higher beach elevations, suggesting that RO embayment erosion may be greatest near mean sea level. In six cases, however, "shoal-opposite" (SO) megacusps are created, whose embayments instead are located shoreward of the surf-zone shoal regions between the channels. These events tend to occur during spring tides, when larger tidal ranges and diurnal inequalities result in elevated mean daily water levels, and they often feature milder wave conditions, with H_s < 1 m. The resulting beach megacusps appear to be centered higher on the beach, well above MSL. Both types of megacusps are visible in two sample rectified images from the Sand City site (Fig. 18). RO megacusps are recorded with the shoreline near MSL (top panel) after a period in which wave heights reached 2 m. SO megacusps appear in the second image when the shoreline contour is near MSL + 1 m (bottom panel), following a several-day period of relatively small waves (H_s ~ 0.7 m). These results suggest that wave heights and mean daily water levels may influence the alongshore locations of megacusp embayments.

On available measured bathymetries from the Sand City site, megacusp embayments consistently appear shoreward of the rip channels and their contours usually extend up the beach face to elevations several meters above MSL. The only directly measured evidence of any type of shoal-opposite cusp creation at Sand City is recorded on several bathymetries from the 2001 RIPEX experiment, in which somewhat shorter wavelength "swash" cusps appear near the MSL + 2 m contour with embayments shoreward of both rip channels and shoals (Fig. 19). Refractive focusing of waves by the bathymetry during periods of sustained higher water levels may have helped to create and/or deepen the SO cusps.

C. MODELING

1. XBeach Theory

Nearshore morphodynamics models may generally be divided into two groups. In *forced* process models, the hydrodynamic conditions generate complementary patterns in the underlying morphology (e.g., Holman & Bowen, 1982). In contrast, for stability or *free* models (also referred to as self-organized models (Blondeaux, 2001)) the length and time scales of the evolving morphology generally do not match those of the hydrodynamics (Dodd et al., 2003). Reniers et al. (2004) forced non-linear wave equations using wave groups described by a directional spectrum that generated large-scale horizontal vortices whose alongshore length scale (O(100–500 m)) was quasi-periodic and similar to that of the wave groups. These long-period (O(4 min–1 hour)) vortical motions are referred to as very-low-frequency (VLF) motions. For very small values of directional spreading, the morphology response was self-organized, but for values exceeding two degrees it became quasi-forced (at wave-group scales). In this range, the generated rip channel spacing closely followed the alongshore scales of the vortices, and channel growth was enhanced by the effects of positive feedback on the hydrodynamics.

Beach evolution is particularly difficult to model in two dimensions, in part because the process intrinsically requires a temporally variable shoreline position. XBeach, a recently developed 2D, depth-averaged numerical coastal model, has been

designed to include such a moving shoreline, allowing for robust simulations of dune erosion, overwash, and breaching (Roelvink, Reniers, van Dongeren, van Thiel de Vries, McCall, & Lescinski, 2009). The model incorporates the quasi-forced morphodynamic formulation of Reniers et al. (2004) and operates on wave-group timescales, parameterizing the sediment transport contributions of individual waves. XBeach also allows for gradual changes to the back beach and dune via an innovative avalanching function. It is principally designed for modeling beach change under storm conditions, and its performance under more moderate wave climates has not yet been fully evaluated. XBeach consists of a mainly first-order upwind, Fortran-based code that includes components for calculating wave forcing, flow velocities, suspended sediment transport and the resulting bed level changes. The following three subsections provide a summary of relevant theory from the existing XBeach model. Additional model modifications made for this study will be discussed in Section IIID.

a. Waves and Rollers

Wave forcing is determined by solving wave action and roller energy balance equations to obtain radiation stresses and then forcing. The wave action balance equation sets the total change of wave action equal to the frequency-normalized dissipation:

$$\frac{\partial A}{\partial t}+\frac{\partial c_x A}{\partial x}+\frac{\partial c_y A}{\partial y}+\frac{\partial c_\theta A}{\partial \theta}=-\frac{\varepsilon_w}{\sigma} \tag{5}$$

where the wave action at each location, A, is equal to the directionally distributed spectral wave energy, E_w, normalized by frequency σ. The wave action propagation speeds c_x and c_y are the sum of group velocity and current components in x- and y-directions, respectively, and c_θ, the propagation speed in the θ-direction, accounts for both bottom refraction and current refraction.

For the present analysis, wave conditions at the offshore boundary are obtained by converting a 2D, directionally spread JONSWAP spectrum into a bound long wave energy time series that varies at wave-group timescales. The JONSWAP-based spectrum is used in place of measured wave spectra in the interests of generalizing model

results and avoiding complicated higher order effects that might result from irregular ADCP-based spectra. The time series is composed of 200 frequency components, each of which is assigned its own amplitude, direction, and random phase. Component amplitudes are interpolated from the 2D input spectrum, and wave angles are assigned randomly using the cumulative distribution function of the directional spreading for the input spectrum (van Dongeren, Reniers, Battjes, & Svendsen, 2003).

The wave energy dissipation due to breaking follows an adapted version of Roelvink (1993):

$$\varepsilon_w = \frac{1}{4}\alpha Q_b \rho g f_m \frac{H_{rms}^3}{h} \tag{6}$$

with α=O(1), ρ representing seawater density, g the gravitational constant, and f_m equal to a representative intrinsic frequency. H_{rms} is root-mean-square (RMS) wave height, and h is water depth. In this expression, following Battjes & Janssen (1978), the fraction of breaking waves is calculated as

$$Q_b = 1 - \exp\left[-\left(\frac{H_{rms}^2}{\gamma h}\right)^n\right] \tag{7}$$

in which γ is a user-set parameter representing the ratio of RMS wave height to water depth at breaking, and n is a user-set parameter with a default value of 10.

Coupled to the wave action balance is the roller energy balance, in which the wave energy dissipation, ε_w, becomes a source term:

$$\frac{\partial E_r}{\partial t} + \frac{\partial c_x E_r}{\partial x} + \frac{\partial c_y E_r}{\partial y} + \frac{\partial c_\theta E_r}{\partial \theta} = -\varepsilon_r + \varepsilon_w \tag{8}$$

where E_r is the directionally distributed roller energy, and the roller dissipation, ε_r, is proportional to the product of the wave phase velocity and the surface shear stress induced by the roller.

b. Flow Field

The depth-averaged velocity flow field is obtained by solving the shallow water wave equations (including the *x*- and *y*-momentum equations and the conservation of mass-flux equation), which are adapted to a Generalized Lagrangian Mean (GLM) formulation (Andrews & McIntyre, 1978; Feddersen, Guza, Herbers, & Elgar, 2000) in order to include short-wave-induced mass fluxes and return flows:

$$\frac{\partial u^L}{\partial t} + u^L \frac{\partial u^L}{\partial x} + v^L \frac{\partial u^L}{\partial y} - \nu_h \left(\frac{\partial^2 u^L}{\partial x^2} + \frac{\partial^2 u^L}{\partial y^2} \right) = -\frac{c_f u^E \sqrt{(1.16 u_{rms})^2 + \left(u^E\right)^2 + \left(v^E\right)^2}}{h} - g \frac{\partial \eta}{\partial x} + \frac{F_x}{\rho h} \tag{9a}$$

$$\frac{\partial v^L}{\partial t} + u^L \frac{\partial v^L}{\partial x} + v^L \frac{\partial v^L}{\partial y} - \nu_h \left(\frac{\partial^2 v^L}{\partial x^2} + \frac{\partial^2 v^L}{\partial y^2} \right) = -\frac{c_f v^E \sqrt{(1.16 u_{rms})^2 + \left(u^E\right)^2 + \left(v^E\right)^2}}{h} - g \frac{\partial \eta}{\partial y} + \frac{F_y}{\rho h} \tag{9b}$$

$$\frac{\partial \eta}{\partial t} + \frac{\partial u^L h}{\partial x} + \frac{\partial v^L h}{\partial y} = 0 \tag{9c}$$

Velocities *u* and *v* are in the Lagrangian frame (superscript *L*) except for those associated with bottom shear stresses, which are Eulerian (superscript *E*). Term c_f is the bed friction coefficient, u_{rms} is short-wave orbital velocity (calculated from computed wave energy and period), η is the free surface elevation, and F_x and F_y are the wave-induced stress gradients. Term ν_h is the horizontal fluid diffusion coefficient, computed at each timestep as a sum of background and turbulent contributions:

$$\nu_h = \nu_b + \beta_\nu h \left(\varepsilon_r / \rho \right)^{1/3} , \tag{10}$$

with user-adjustable background eddy viscosity, ν_b, and turbulent viscosity factor, β_ν, each between 0 and 1 (van Thiel de Vries, 2008; Battjes, 1975). In a recent study by Brown et al. (2009) at Sand City, California, a similar expression for turbulent diffusion (with $\beta_\nu = 1$, but based on wave height) was found to predict measured surf-zone

diffusivities accurately (r^2 = 0.95). For computations, a staggered grid is employed on which velocities are defined at the sides of each cell while bed and surface elevations are defined in the center.

c. Sediment Transport

A depth-averaged advection-diffusion equation is used to model the sediment transport (Galappatti & Vreugdenhil, 1985):

$$\frac{\partial hC}{\partial t}+\frac{\partial hCu^E}{\partial x}+\frac{\partial hCv^E}{\partial y}+\frac{\partial}{\partial x}\left(D_h h\frac{\partial C}{\partial x}\right)+\frac{\partial}{\partial y}\left(D_h h\frac{\partial C}{\partial y}\right)=\frac{hC_{eq}-hC}{T_s} \tag{11}$$

with the depth-averaged sediment concentration, C, allowed to vary on the wave-group timescale. For the present analysis, the horizontal sediment diffusion coefficient, D_h, is computed in the same manner as ν_h (Eq. 10). The adaptation time, T_s, describes the timescale of the sediment response to differences between the equilibrium concentration, C_{eq}, and the actual concentration, C. It is calculated using a simple ratio of water depth to sediment fall velocity and limited to a value greater than or equal to 0.2 s.

The equilibrium sediment concentration is determined from one of two selected formulations, both of which are tested this analysis. The first option is the Soulsby-van Rijn formulation (Soulsby, 1997):

$$C_{eq}=\frac{A_{sb}+A_{ss}}{h}\left[\sqrt{u^2_{stirring}}-u_{cr}\right]^{2.4} \tag{12}$$

where the stirring velocity, $u^2_{stirring}$, is a combination of the Eulerian mean velocity and near-bed short-wave orbital velocity:

$$u^2_{stirring}=\left(u^E\right)^2+\left(v^E\right)^2+0.018\frac{u^2_{rms}}{c_d}. \tag{13}$$

It must exceed a critical threshold value, u_{cr}, in order to initiate sediment transport via a nonzero C_{eq}. Short-wave orbital velocity, u_{rms}, is computed from local wave height and a

representative wave period, T_{rep}, which is somewhat less than T_p and determined from a weighted average including only spectral frequencies with high energy levels. The drag coefficient, c_d, is determined from flow velocity alone (neglecting short wave effects). The bed load and suspended load coefficients, A_{sb} and A_{ss}, are functions of sediment grain size and density as well as local water depth. Because the Soulsby-van Rijn formulation tends to predict unrealistically high sediment transport rates under large breaking waves, XBeach also includes a Shields-parameter-based limiter, θ_{sf}, which is used to define a maximum attainable stirring velocity and place an upper limit on C_{eq} values under extreme conditions (McCall et al., 2010).

The second formulation option for C_{eq} uses a different expression for the near-bed wave-breaking-induced turbulence, based on the bore-averaged turbulence energy (van Thiel de Vries, 2008):

$$C_{eq} = \frac{A_{sb}}{h}\left[\left(\left|u^E\right|^2 + 0.64u_{rms,2}^2\right)^{0.5} - u_{cr}\right]^{1.5} + \frac{A_{ss}}{h}\left[\left(\left|u^E\right|^2 + 0.64u_{rms,2}^2\right)^{0.5} - u_{cr}\right]^{2.4} \tag{14}$$

Short-wave orbital flow effects are included here as $u_{rms,2} = \sqrt{u_{rms}^2 + 1.45k_b}$, where the bore coefficient k_b is a function of the short-wave bore interval, T_{bore}, estimated using a parameterized model of the wave shape (Rienecker & Fenton, 1981). While the Soulsby-van Rijn expression has wave-generated sediment suspension proportional to flow drag (i.e., forced from the bottom), in the alternate formulation it is dependent on maximum wave surface slope (i.e., forced from the surface), which van Thiel de Vries (2008) found to be better correlated with observations in wave tank experiments.

The rates of horizontal sediment transport in x and y directions are given by

$$S_x = hC\left(u^E + u_{asym}\right) + D_h h\frac{\partial C}{\partial x} \tag{15}$$

$$S_y = hC\left(v^E + v_{asym}\right) + D_h h\frac{\partial C}{\partial y} \tag{16}$$

Eulerian velocities u^E and v^E are augmented by velocity asymmetry contributions (u_{asym} and v_{asym}) that account for additional sediment suspension due to wave asymmetry in the surf zone. The magnitude of these terms is tuned with the user-adjustable parameter, $u_{a,fac}$. The rate of change in the bed level, $\partial z_b/\partial t$, is obtained by assuming conservation of sediment volume and is dependent upon gradients of S_x and S_y together with the bed porosity, p:

$$\frac{\partial z_b}{\partial t} + \frac{f_{mor}}{(1-p)}\left(\frac{\partial S_x}{\partial x} + \frac{\partial S_y}{\partial y}\right) = 0 \tag{17}$$

The morphological acceleration factor, f_{mor}, has a default value of 1 but can be increased by the user to speed up bathymetry change at each timestep (Roelvink, 2006). XBeach also includes a simple avalanching function to account for slumping of overly steep slopes. When the bed slope in x or y exceeds a user-set critical value, m_{cr}, surrounding bed elevations are gradually adjusted to reduce it to this value.

As has been illustrated, the theoretical basis of XBeach is very similar to that of the more established Delft3D model (Roelvink & van Banning, 1994). However, there are several important differences between the two. While the Delft3D wave solver is essentially stand-alone, the wave action solver in XBeach is an integral part of the main code. Because XBeach is based on wave action, it includes the effects of wave-current interaction. Numerical schemes used in Delft3D are generally higher order, while XBeach relies on simple forward differencing to maintain stability. While this implies that the newer model will be less accurate, it also allows for somewhat more rapid computation of results. Finally, as mentioned in the previous paragraph, the morphological computations in XBeach include an avalanching function not available with Delft3D. This makes the new model particularly well suited to simulating coastal erosion of the back beach, including dune undercutting and slumping.

2. Model 1D Calibration

To calibrate XBeach parameters to the Sand City site, the model is initialized in 1D with an alongshore-averaged beach profile created from the bathymetry measurements of the 2007 RCEX experiment (Brown et al., 2009), which is extended offshore to 30 m depth using a 1:50 slope. In a total of 36 simulations varying six model parameters, XBeach computes the profile evolution until an "equilibrium profile" has been attained, defined as less than 1 mm vertical change in 10 simulation hours at all cross-shore locations. Wave spectral inputs at the offshore boundary, H_{m0} = 0.89 m and T_p = 9.8 s, are based on the average conditions measured by the ADCP at Sand City from 2006 – 2007, reverse-shoaled to 30 m depth. First, the Shields limiter (θ_{sf}), wave asymmetry ($u_{a,fac}$), and suspended sediment response ($T_{s,fac}$) are optimized simultaneously in a set of 27 tests, with each parameter assigned three different values (all other model parameters are set to defaults). Optimal site-specific values for the tested parameters are extracted from the simulation whose final equilibrium profile maintains the best root-mean-square (RMS) fit to the initializing profile. Using the optimal settings determined for θ_{sf}, $u_{a,fac}$, and $T_{s,fac}$, values for three additional parameters are then varied individually in nine additional tests to fine tune the model's performance, including the morphological acceleration factor (f_{mor}), the threshold water depth (h_{min}), and the breaker parameter ($\gamma \sim H_s/h$). In all simulations, it is found that XBeach tends to flatten the initial Sand City profile's shoal terrace until it is nearly horizontal. None of the simulations generate a persistent bar-trough profile, although such profiles are occasionally measured across the shoals at Sand City. These model limitations are discussed further in Section IIIE.

Final optimized values for the six tested parameters resulted in an RMS elevation difference of 13 cm (and maximum difference of 95 cm) between equilibrium and initializing profiles (Fig. 20). Parameter ranges and optimal values are summarized in Table 3. While the optimal values generally appear reasonable, both θ_{sf} and γ are somewhat lower than their default settings. In simulations with hurricane waves, McCall et al. (2010) found an optimal value of θ_{sf} = 1, but the present simulations indicate that a smaller value of 0.8 is more effective under more moderate conditions. While most field measurements generally suggest a value of about 0.60 for γ when using significant wave

height (e.g., Thornton & Guza, 1982), these simulations obtain better results with a lower value of 0.45. Applying the Delft3D model at the same site, Reniers, MacMahan, Thornton, & Stanton (2006) also found $\gamma = 0.45$ to give the best match to measured wave heights throughout the surf zone. A field study by Sallenger & Holman (1985) indicated that γ could range from 0.41 to 0.78 across the surf zone when computed using H_s. For waves breaking across a flat terrace, Raubenheimer, Guza, & Elgar (1996) observed γ values as low as 0.2.

3. Model 2D Evaluation

With optimal site-specific parameter values established, XBeach is applied in 2D to hindcast two cases of bathymetry evolution measured during RCEX. The first test makes a quantitative evaluation of the model's skill using measured bathymetry. The second test evaluates model performance more qualitatively, comparing output bathymetry to rectified video images. Additional model parameter settings used for the 2D simulations are provided in Table 4. To maintain computational stability, the model's wave-current interaction option is turned off. Instead, wave-current interaction effects are represented by increasing the eddy viscosity due to roller-induced turbulence, setting $\beta_\nu = 1$ and $\nu_b = 0.1$ in Eq. 10. To help speed up computations, the bathymetry grid is made variable in the cross-shore direction, starting with dx = 32 m offshore and decreasing to dx = 4 m in the nearshore. In both cases, input bathymetry is extended offshore to approximately 30 m depth using a 1:50 slope, and in the alongshore direction by appending a mirror image of the entire measurement region to each side.

a. Quantitative Evaluation

The quantitative 2D model testing is conducted using data recorded over a ten-day period during the RCEX experiment at Sand City (Fig. 21). The model is initialized with nearshore bathymetry measured on May 1, 2007, and model output is validated against measured bathymetry from May 11, 2007. Two different types of simulations are conducted. The first 22 simulations are limited to the approximately 3.5-day "storm" period (May 3 – 7), anticipating that these waves were responsible for the majority of the bathymetry change over the ten days. Average "storm" wave statistics are

extracted to initialize a JONSWAP spectrum with H_{m0} = 1.40 m and T_p = 9.5 s. In the storm test cases, wave height and period are either fixed at these values, increased by 20%, or decreased by 20%, with peak direction set to shore-normal. For these and all following simulations, spectra are given a moderate directional spread (cosine power $s = 8$), with Nyquist frequency $f_{nyq} = 0.3$ Hz and JONSWAP peak enhancement factor $\gamma_{jsp} = 3.3$ (Table 4). Both C_{eq} formulations are tested for each of the nine different wave height and period combinations. Model settings for the morphological acceleration factor (f_{mor}) are varied between 1 and 10 in four additional tests using only average wave statistics. The mean water level is fixed at MSL.

In an attempt to better represent the actual wave climate over the entire 10-day period, XBeach is run for ten full days in a set of 9 additional "daily" simulations, initialized with either daily-averaged or two-day-averaged wave height and period values. The tests include three combinations of wave height and period for each day: [H_{m0}, T_p], [H_{m0} + 20%, T_p + 20%], and [H_{m0} – 20%, T_p – 20%]. Two different values, 1 and 10, are used for the model's f_{mor} parameter in the daily-averaged wave cases.

Model skill in the quantitative 2D tests is measured with the following ratio (Gallagher et al., 1998):

$$Skill = 1 - \frac{\sum_{i=1}^{N} \left(dz_{b,meas_i} - dz_{b,xb_i} \right)^2}{\sum_{i=1}^{N} \left(dz_{b,meas_i} \right)^2}, \qquad (18)$$

in which $dz_{b,meas_i}$ and dz_{b,xb_i} are measured and XBeach-predicted bed level change at location i, respectively. A skill value of one indicates a perfect model, a value of zero is the same as predicting no bathymetry change, and a negative value is worse than predicting no change.

In the present tests, XBeach achieves skill values between -0.1 and +0.6 (Fig. 22). For simulations using representative storm wave statistics, the best results are obtained after about three days of simulation time. Lower skill values are obtained when "storm" wave height and/or period are set to 20% less than the actual measured mean

values (i.e., H_{m0} = 1.12 m, T_p = 7.6 s), while better skill is achieved with measured or larger waves and periods (i.e., H_{m0} = 1.40 – 1.68 m and T_p = 9.5 – 11.4 s). In the ten-day simulations using daily and two-day averaged wave inputs, model skill tends to reach a maximum after about 4 days, and then gradually declines as the bathymetry is further smoothed. The highest skill value (skill = 0.60) is achieved for an 84-hr "storm" simulation with H_{m0} = 1.40 m, T_p = 9.5 s, using the Soulsby-van Rijn formulation for C_{eq} and a morphologic acceleration factor = 1. A closer comparison of modeled and measured bathymetries for two of the large-wave, higher-skill cases reveals that model performance is better in deeper portions of the surf zone than in the swash zone, where contours appear excessively smoothed (Fig. 23), particularly in the 10-day results. Simulations with smaller waves achieve a higher skill in the swash region but a lower skill farther offshore, where they underpredict bathymetry change.

b. Qualitative Evaluation

A second, smaller set of qualitative, 2D XBeach tests is conducted with the goal of hindcasting a recorded megacusp formation event. On May 23, 2007, three days after the conclusion of the RCEX experiment, megacusps were observed by video cameras at the Sand City site. Initializing bathymetry data are available from RCEX measurements on May 18, but only video records are available for May 23. Continuous wave data for the time period are obtained from the 13-m ADCP (Fig. 24). For the mild "storm" period from May 20–23, average wave statistics are H_{m0} = 1.1 m and T_p = 10.0 s. XBeach is initialized with the May 18 bathymetry and then run for three days with a morphological acceleration factor of 10. To limit the complexity of the problem, shore-normal, JONSWAP-distributed waves are used at the boundary, with spectral parameters based on measured wave values. Offshore H_{m0} and T_p are again varied by ±20% about the measured values in the same manner as for the "daily" quantitative tests. Shields factor, θ_{sf}, is set to either 0.8 or 1.2, and each of the two C_{eq} formulations is applied, resulting in a total of 12 tests. Mean water level is again fixed at MSL. Modeled final bathymetries are compared to video shoreline images to gauge XBeach's success at hindcasting an actual episode of megacusp formation.

The quantitative test results above suggest that oversmoothing of the intertidal zone may be less of a problem for XBeach in simulations during periods featuring more moderate waves and shorter simulation periods. This is confirmed by results from the present tests, which provide evidence that XBeach can hindcast such an event and reasonably represent the associated shallow water flow field and bathymetry shape. Optimal model results are obtained using the Soulsby-van Rijn equilibrium concentration formulation and "storm" waves with H_{m0} = 1.1 m and T_p = 10 s, and appear mildly oversmoothed when compared to the May 23rd video image (Fig. 25, top panel). The modeled final shoreline contour successfully captures the locations of all three megacusp embayments that develop in the video view field. In one of the three predicted embayments, the modeled flow field also includes swash zone counter-circulations (Fig. 25, middle panel). A comparison of initial and final bathymetries and shoreline contours shows that the modeled waves and flow field acted to deepen and broaden three pre-existing, smaller RO perturbations into larger RO megacusp embayments (Fig. 25, bottom panel).

4. Megacusp Formation

A range of different scenarios is now used to examine the role of mean daily water levels, wave energy, and bathymetry in megacusp formation processes in southern Monterey Bay. Key model parameters are again fixed at settings determined in the 1D equilibrium profile simulations. The two initializing bathymetries for the scenarios are based on measured RCEX bathymetry data from the Sand City site recorded on May 1, 2007 (Fig. 26). A realistic model bathymetry is prepared by three-point smoothing the measured bathymetry data in both cross- and alongshore directions. A second, idealized model bathymetry is constructed by superimposing identical, 100m-spaced rip channels onto an alongshore-uniform depth grid created from the alongshore-mean profile of bathymetry recorded on May 1. In the surf zone, amplitudes of the idealized rip channels are adjusted to match the vertical range of the measured bathymetry profiles. On the beach, measured alongshore variations are retained in the "real" bathymetry, but in the

"ideal" bathymetry they are tapered off to an initial planar beach above MSL + 1.5 m. Offshore of the measured region, both bathymetries are extended out to 30 m depth using a planar 1:50 slope.

As noted in Section IIIB, most megacusp formation at the Sand City site is observed to occur when maximum offshore significant wave heights are roughly 1.5 – 2 m. However, in preliminary 2D trials with XBeach using modeled wave heights of 1.5 m or above, surf-zone and beach contours are found to rapidly smooth and straighten until bathymetry is nearly alongshore-uniform throughout the model grid. This oversmoothing tendency was also observed in results from the preceding model evaluation tests. To limit such effects during simulations of idealized megacusp formation, only mild-to-moderate wave climates (i.e., H_{m0} = 0.5 to 1.2m, T_p = 7 to 11 sec) are included. As was also mentioned in Section IIIB, such moderate waves have also been found to generate megacusps at Sand City, although the cusps themselves may be shallower and/or require more time to fully develop. Tests are allowed to run for longer periods (up to two days) to exaggerate the waves' effects on the beach face. The implicit expectation is that when XBeach is run for a longer time with smaller waves, predicted bathymetry change will reasonably match that which would occur with larger waves in the field over a shorter duration.

These tests are targeted at creating both RO and SO megacusps, under a range of wave conditions and at multiple, fixed water levels. Nine different simulations (three wave types at three tide elevations) each are run over both the "ideal" and "real" bathymetries. Initializing shore-normal JONSWAP waves at the offshore boundary are given three different sets of significant wave height and peak period values: [H_{m0}, T_p] = [0.5 m, 7 sec], [0.89 m, 9.8 sec], and [1.2 m, 11 sec]. The second set of values is the same as were used for the equilibrium profile computations. Three different fixed water levels are employed to investigate the role of monthly tidal cycles and bathymetry: MSL + 0 m, +0.75 m, and +1.5 m. Simulations with water levels below MSL are not included because wave breaking shifts farther offshore and has little effect on the beach.

Simulation results are summarized in Fig. 27. Of the 18 megacusp formation simulations, a total of seven scenarios result in the formation of purely SO megacusps,

while six scenarios result in the growth of purely RO megacusps. Two simulations on "real" bathymetry result in a mix of both SO and RO megacusps. In the three remaining scenarios, the shallow water regions and the shoreline are washed out, resulting in a "flat," alongshore uniform bathymetry. Overall results indicate that SO megacusps tend to consistently form when fixed water levels are higher, while RO megacusps usually develop when the water level is fixed near MSL.

An examination of the flow fields from two selected ideal bathymetry simulations sheds some light on the important differences between the two types of megacusp formation. The first selected simulation generates SO megacusps (Fig. 28) and features moderate waves (H_{m0} = 1.2 m, T_p = 11 s) and a high water level (MSL + 1.5 m). Here, the "ideal" rip channel bathymetry refractively focuses wave energy onto the shoals and strengthens the onshore flow field there. The refracted waves converge onto the shoals but do not fully break until they reach the shoreline. The concentration of wave energy shoreward of the shoals likely results in greater sediment suspension there instead of at rip channel locations. This sediment is advected alongshore by the diverging flow field at the shoreline, creating SO megacusps.

In a second selected simulation, with the water level at MSL, the same moderate waves as above (H_{m0} = 1.2 m, T_p = 11 s) now generate flows that slowly carve out RO megacusps (Fig. 29). Here, the different breaking patterns over shoals and rip channels result in a setup imbalance near the shoreline and converging flow into rip channels from the surrounding shoals. The initial bathymetry (Fig. 29, top panel) includes narrow alongshore concavities in the beach shoreward of the rip channels (as seen in blue MSL contour line), so that the converging flow in the shallow surf zone creates counter-circulations in the swash region (Fig. 29, middle and bottom panels). This diverging flow at the shoreline further erodes the initial concavities and steepens them into larger RO megacusps.

The combined results of the nine idealized bathymetry simulations strongly suggest that pre-existing beach perturbations are essential to modeled RO megacusp formation. Without the perturbations, modeled counter-circulations do not develop shoreward of the rip channels, and RO megacusp formation is not initiated. As was

mentioned earlier, all beach perturbations are smoothed out above MSL + 1.5 m on the "ideal" bathymetry (Fig. 26). As the above reasoning would suggest, the only cases of RO megacusp formation on this bathymetry occur for fixed water levels below this cutoff elevation (Fig. 27, bottom panel).

A more complex result is seen in the third selected simulation, which tracks the evolution of the "real" bathymetry during a high water period under small waves (Fig. 30). In this case, small shore-normal waves (H_{m0} = 0.5 m, T_p = 7 s) are shoaled over the three-point-smoothed RCEX bathymetry with water level fixed at MSL + 1.5 m. For these conditions, the bathymetry response is decidedly "mixed," changing at different timescales. After twelve hours, a broad RO megacusp has formed at about y = 600 m (Fig. 30, second panel). The mean onshore flow over an obliquely angled shoal is redirected by the bathymetry into a localized alongshore jet near the shoreline that removes sediment from the megacusp embayment region. Qualitative similarities between this flow field and the RO megacusp video image shown earlier (Fig. 18, top panel) suggest that the simulation may be capturing some aspects of megacusp formation processes at Sand City that are missing from ideal bathymetry results. As time passes, this feature is joined by slowly deepening SO megacusps at alongshore shoal locations, roughly y = 440 m and 560 m (Fig. 30, bottom panel). In the field, such a beach shape might be expected to develop in the summer over a timescale of several days, when milder summer waves gradually modify the upper beach with the aid of sustained high water levels seen during periods of maximum range spring tides.

D. PROCESS-BASED FREQUENCY ANALYSIS

To investigate the sediment transport processes associated with megacusp formation in different frequency ranges, two idealized bathymetry cases from the preceding section are selected for a more in-depth analysis—one case that results in SO megacusps and a second that features RO megacusps. Results from a third simulation on the realistic bathymetry are also examined and contrasted with the two idealized cases. To facilitate this analysis, the sediment transport equations in the XBeach code (Eq. 15 and 16) are rewritten with their principal terms expanded into two-hour-mean, VLF, and infragravity frequency ranges:

$$
\begin{aligned}
S_x &= \overline{S_x} + \widehat{S_x} + \widetilde{S_x} \\
&= (\overline{hC} + \widehat{hC} + \widetilde{hC})\left[(\overline{u}^E + \hat{u}^E + \tilde{u}^E) + (\overline{u}_{asym} + \hat{u}_{asym} + \tilde{u}_{asym})\right] \\
&\quad + (\overline{D}_h + \hat{D}_h + \tilde{D}_h)(\overline{h} + \hat{h} + \tilde{h})\frac{\partial(\overline{C} + \hat{C} + \tilde{C})}{\partial x}
\end{aligned} \tag{19}
$$

$$
\begin{aligned}
S_y &= \overline{S_y} + \widehat{S_y} + \widetilde{S_y} \\
&= (\overline{hC} + \widehat{hC} + \widetilde{hC})\left[(\overline{v}^E + \hat{v}^E + \tilde{v}^E) + (\overline{v}_{asym} + \hat{v}_{asym} + \tilde{v}_{asym})\right] \\
&\quad + (\overline{D}_h + \hat{D}_h + \tilde{D}_h)(\overline{h} + \hat{h} + \tilde{h})\frac{\partial(\overline{C} + \hat{C} + \tilde{C})}{\partial y}
\end{aligned} \tag{20}
$$

For each expanded quantity, an overbar indicates the wave-group mean, a carat is used for the VLF variations, and a tilde is used for the infragravity variations. Note that, in Eq. 19 and 20, the total sediment concentration in the water column, *hC*, is expanded as a single quantity in the two advection terms. In the modified XBeach code, the three different frequency contributions to each term are updated at every sub-second model timestep. Each term's mean is computed as a running average over 7200 s (two hours), which filters out wave-group and other lower frequency oscillations while still resolving variations associated with daily tides and storm events. The VLF contribution is computed as a 250-s running average of each term after its mean has been subtracted. This term will include transport due to very-low-frequency, large-scale horizontal surf-zone eddies discussed in Section IIIA. The infragravity contribution is then obtained as a residual by subtracting the computed mean and VLF contributions from the original term's "instantaneous" value at each timestep.

The modified version of XBeach tracks the contributions of 90 distinct components, including 36 advection components made up of a two-term product (e.g., $\overline{hC\tilde{u}}$) and 54 diffusion components made up of a three-term product (e.g., $\overline{D}_h\hat{h}\frac{\partial\tilde{C}}{\partial y}$). At every two-hour output timestep, the adapted model computes and stores two-hour average values of each component at all grid locations. Based on the results of Thornton et al. (1996) and Gallagher et al. (1998), it is anticipated that the largest components will be those containing just mean terms (e.g., $\overline{hC\overline{u}}$). Components involving a product of

two terms in the same frequency range (e.g., $\widehat{hC}\hat{v}$ or $\overline{D}_h\tilde{h}\frac{\partial\tilde{C}}{\partial x}$) are also expected to be significant in cases where in-phase resonant oscillations create a positive feedback (as seen in Reniers et al., 2004). If the paired oscillating terms are randomly phased, however, these components will be much smaller. The average sediment transport contributions due to components that include unpaired oscillating terms (e.g., $\widehat{hC}\overline{u}$ or $\overline{D}_h\hat{h}\frac{\partial\tilde{C}}{\partial y}$) are expected to be relatively negligible, since any terms oscillating with periods much less than two hours should average out to zero.

The ten largest sediment transport components of Eq. 19 and 20 for the three selected megacusp formation simulations are listed with relative magnitudes at time t = 4 hrs in Table 5. As anticipated, the most dominant components in all three selected cases are those involving products of mean terms (e.g., $\overline{hC}\,\overline{u}$). More surprisingly, however, the next largest transport contributions in the two moderate wave, idealized bathymetry cases are from advective components including a product of one mean term and one oscillating (VLF) term (e.g., $\overline{hC}\hat{u}$). This suggests that the timescales of some VLF oscillations may be greater than 30 minutes and thus make a non-zero contribution to sediment transport over the two-hour averaging period. The next largest contributions over idealized bathymetry are from components that include either an advective product of two VLF oscillating terms (e.g., $\widehat{hC}\hat{v}$) or a diffusive product of three means (e.g., $\overline{D}_h\overline{h}\frac{\overline{\partial C}}{\partial x}$). For the advective VLF product, this indicates that some degree of in-phase, resonant interaction between the two terms is occurring. In the third selected simulation with small waves over realistic bathymetry, transport contributions from the diffusive product components ($\overline{D}_h\overline{h}\frac{\overline{\partial C}}{\partial x}$ and $\overline{D}_h\overline{h}\frac{\overline{\partial C}}{\partial y}$) and asymmetry ($\overline{hC}\,\overline{u}_{a,u}$) are relatively more important than the VLF components, likely owing to the lower wave energies and increased wave breaking at the shoreline.

The majority of sediment transport forcing in all three cases is provided by these few largest components. Sediment transport contributions from components involving terms at infragravity timescales are generally several orders of magnitude smaller than those from the mean advective transport. The largest of these, $\widetilde{hC}\tilde{u}$, amounts to at most three percent of $\overline{hC}\overline{u}$ at t = 4 hrs, declining thereafter. Diffusive sediment transport components with terms from VLF or infragravity timescales also make significantly smaller contributions than the mean diffusion. In the selected "real" bathymetry simulation, the smaller transport contributions are more widely distributed among a larger number of components. Cross-shore turbulent diffusion appears to play a stronger role when water level is higher, likely because the waves tend to break more often at the shoreline and less often over the shoals for these cases.

1. SO Megacusps

Additional, two-dimensional insight into the megacusp formation processes is obtained from vector plots of paired *u*- and *v*- components on top of the predicted bathymetry change due to those components. For the SO megacusp formation simulation on ideal bathymetry, the large mean advective contribution ($\overline{hC}\overline{u}$ and $\overline{hC}\overline{v}$) includes strong cross-shore and alongshore components in the earlier stages (Fig. 31, top panel), but becomes more rip-current-dominated at a later stage (Fig. 32, top panel). At the MSL + 1.5 m shoreline, the magnitude of the alongshore transport component increases away from shoal locations and decreases toward rip channel locations, indicating that the mean flow extracts sediment from SO megacusp embayments and deposits some of it to augment the megacusp horns.

The longer timescale variations of the second largest SO megacusp transport components ($\overline{hC}\hat{u}$ and $\overline{hC}\hat{v}$) are apparent from a comparison of the associated early and late stage vector transport fields (Fig. 31 and 32, second panel). In contrast to the mean flow, these components contribute to accretion at the SO cusp embayments and erode regions shoreward of the rip channels, particularly at the later stage. As it makes up only about ten percent of the contribution from the mean components, however, this accretion and erosion will only mildly damp the growth of the SO megacusps. This portion of the

transport field continues to vary noticeably from one two-hour timestep to the next (not shown), reflecting the long-period VLF flow field cycles discussed above. Because of such variations, the net effect of these components on SO megacusp formation is more complex, and they likely play both supporting and opposing roles at different times.

The third-ranked component pair for SO megacusps is the product of the VLF sediment concentration with the mean flow field (i.e., $\widehat{hC}\overline{u}$ and $\widehat{hC}\overline{v}$). Contributing roughly 5% of the sediment transport of the mean advective components, this vector field also acts to dampen the SO megacusp growth (Fig. 31 and 32, third panel). Transport vectors maintain similar orientations at both early and later stages, but their magnitudes vary considerably over time, controlled by the VLF-varying concentration term ($\widehat{hC}$). The fourth-ranked component pair ($\widehat{hC}\hat{u}$ and $\widehat{hC}\hat{v}$) contributes about 0.5% of the transport forcing of that due to the largest components (Fig. 31 and 32, bottom panel). These VLF product components play their most significant role shoreward of the rip channels, contributing to both erosion and accretion. Their vector field also varies from one timestep to the next, with differences most visible in the alongshore direction (i.e., $\widehat{hC}\hat{v}$).

2. RO Megacusps

For the RO megacusp case, the mean advective sediment transport components ($\overline{hC}\overline{u}$ and $\overline{hC}\overline{v}$) are again dominant (Fig. 33 and 34, top panel). As with the SO megacusps, the shoaling waves again erode sediment from the shoals (blue regions) and deposit it into the rip channels (red regions). In this case, however, a consistent erosive region (blue) also develops at the shoreline shoreward of each rip channel, created by the swash-zone counter-circulations discussed in Section IIIC. The color range on the plots has been adjusted to better emphasize these regions. At t = 4 hrs, the diverging transport pattern created by these circulations contributes directly to deepening the RO megacusps, as indicated by the dark blue shading in the centers of early stage embayments (Fig. 33, top panel). Megacusp growth is relatively slow, as the mean transport components also erode the beach shoreward of the shoals. Later on, at t = 14 hrs, the mean advective

transport field remains roughly the same, but predicted bathymetry change becomes erosional at all locations across the shoals and along the shoreline.

Similar to the earlier SO megacusp results, advective components involving a product of mean and VLF terms again provide the second- and third-largest transport contributions for RO megacusp formation (Fig. 33 and 34, second and third panels). Here, however, their role in the cusp formation process appears to be more focused and relatively more important than in the SO case. Contributions from the components including the mean flow field (i.e., $\widehat{hC}\overline{u}$ and $\widehat{hC}\overline{v}$) are roughly equal to those including the VLF flow field (i.e., $\overline{hC}\hat{u}$ and $\overline{hC}\hat{v}$). At an early stage, transport patterns for both component pairs resemble those of the mean flow, with each also contributing to erosion of the RO megacusp embayments (Fig. 33, second and third panels). Later, although both contributions become smaller, their transport fields at the shoreline both act to remove sediment from RO cusp locations and deposit it at the cusp horns. In contrast to the SO megacusp case, the vector fields associated with these two transport contributions are somewhat more stable during later stages (not shown), consistently acting to build the RO megacusps.

The fourth-ranked sediment transport contribution for RO megacusps is provided by the advective products of mean concentration and mean wave asymmetry ($\overline{hC}\overline{u}_{asym}$ and $\overline{hC}\overline{v}_{asym}$), which consistently act to erode RO cusp embayments and build up their horns. These contributions are largely directed shoreward, as the onshore transport by higher velocities under wave crests significantly exceeds the offshore transport under the lower velocity troughs. Making up roughly 1% of the magnitude of the mean transport contribution, the asymmetry components also slightly slow the erosion in shoal areas and accretion in rip channels.

3. Real Bathymetry Results

A frequency analysis of dominant sediment transport processes in the sample "real" bathymetry simulation using small waves highlights the more important role played by diffusion and wave asymmetry in such cases (Fig. 35 and 36). While the mean

advective components ($\overline{hC}\overline{u}$ and $\overline{hC}\overline{v}$) remain dominant, contributions from the mean diffusive components ($\bar{D}_h\bar{h}\overline{\frac{\partial C}{\partial x}}$ and $\bar{D}_h\bar{h}\overline{\frac{\partial C}{\partial y}}$) are not far behind and may play a primary role in the initial development of the RO megacusp centered at y = 600 m alongshore. The mean advective transport field is roughly the same at early and later stages, principally acting to erode beach sediment shoreward of shoals and gradually build SO megacusps (Fig. 35 and 36, first panel). At the early stage, the transport due to diffusive components (Fig. 36, second panel) is of comparable magnitude to the mean advective transport near y = 600 m along the early stage shoreline, acting to erode the RO megacusp embayment there. In contrast, the mean advective transport contribution appears accretionary at this location. Like the mean diffusion, the mean wave asymmetry ($\overline{hC}\overline{u}_{asym}$ and $\overline{hC}\overline{v}_{asym}$) also plays a smaller role in eroding the RO megacusp embayment, but like the mean flow, its principal contributions are at alongshore locations of the shoals (Fig. 35 and 36, third panel). The fourth-ranking advective component pair, $\widehat{hC}\overline{u}$ and $\widehat{hC}\overline{v}$, make a smaller contribution that declines over time, dropping to 5% of the mean advective transport at the later stage (Fig. 35 and 36, fourth panel).

E. DISCUSSION

1. XBeach Evaluation Tests

Based on previous studies, the performance of XBeach in the quantitative skill tests seems reasonable. There have been a number of skill estimates computed previously for either XBeach or the similar Delft3D model, including several at the Sand City site (Table 6). Most estimates have been for wave and flow quantities (i.e., H_s, u, and v) rather than for bathymetry. In predicting wave heights, both XBeach and Delft3D have achieved high skill levels of 0.83 to 0.93, while for Eulerian and Lagrangian velocities the skill range is lower: 0.5 to 0.7. As modeled bathymetry is based upon accurate estimates of both waves and flow, model skill levels would logically be expected to be lower for bathymetry than for either waves or flow. A recent study by McCall et al. (2010) obtained skill levels as high as 0.77 for two-dimensional XBeach estimates of

hurricane storm surge and overtopping at Santa Rosa Island, Florida. However, the present study focuses on moderate wave climates, for which some assumptions of a depth-averaged model (e.g., vertically uniform flow fields and sediment concentrations) are less accurate.

The oversmoothing of shallow water bathymetry by XBeach (Section IIIC, subsection 3) likely results from an underestimation of uprush sediment transport in the swash zone, relative to offshore transport by the backwash. This imbalance leads to excessive erosion of the beach face and deposition in the rip channels. Masselink & Hughes (1998) conclude from an analysis of field measurements of individual waves that the uprush and backwash processes on a beach are governed by different physical processes not presently accounted for in available models. Nielsen, Robert, Møller-Christiansen, & Oliva (2001) suggest that large horizontal pressure gradients at bore fronts may contribute to increased fluidization of beach sediment during uprush, augmenting onshore transport. If so, this could act to balance the additional offshore transport during backwash due to fluidization by pressure gradients (Horn et al., 1998), resulting in a more stable beach profile under moderate waves. Representation of these effects in the current version of XBeach would require a parameterization to wave group timescales. In the absence of an effective parameterization, the model would need to be adapted to run at the timescale of individual waves, which would significantly increase computation time. Both options are currently being investigated by model developers.

2. Factors Influencing Megacusp Formation

The preceding model analyses have examined the roles played by mean daily water level, bathymetry shape, and wave energy in the formation of megacusps on rip channel bathymetry. Distinct patterns have emerged under which higher mean water levels and planar beaches result in SO megacusp formation, while lower mean water levels with pre-existing beach perturbations lead to RO megacusps. Smaller waves are more often associated with RO megacusps, while moderate waves usually build SO megacusps, and larger storm waves rapidly create an alongshore uniform beach. In an effort to reduce the considerable complexity of the problem, potentially important factors

including larger wave heights, oblique wave directions, and water level oscillations due to daily tidal cycles and individual waves have been excluded from this analysis. These are each briefly discussed in the following paragraphs.

Because of the model's tendency to oversmooth nearshore contours, the actual effects of moderately large waves (H_s ~ 2 m) on rip channel bathymetries and cuspate shorelines are not correctly represented by XBeach. However, the megacusp formation results presented in Fig. 27 suggest that megacusp locations are more sensitive to mean water level and beach shape than to wave energy level. The quantitative tests (Section IIIC) showed that XBeach can hindcast measured bathymetry change over several days with a reasonable level of skill. The qualitative testing confirmed that the model can generate megacusps using actual wave data, when milder wave conditions are present, indicating that XBeach represents the actual flow fields and sediment transport fairly well. It is therefore suggested that the modeled bathymetry evolution under small and moderate waves is relatively similar to what would be seen with these larger waves, except that it occurs more slowly.

Oblique wave approach angles, which were also not considered here, may affect bathymetry shape and megacusp location by tilting rip channels and shoals relative to the shoreline, and by shifting the alongshore locations of setup maxima and shoreline erosion. Measured wave directions indicate that the mean approach angle at Sand City is sometimes slightly south of shore-normal. However, additional simulations with XBeach (not included here) suggest that much larger breaking wave angles (greater than 10 degrees) are required in order to significantly change the outcomes of the presented megacusp formation tests. In modified RO megacusp simulations over idealized bathymetry, offshore wave angles of 20–30º tend to focus shoreline erosion into the centers of the beach concavities, creating somewhat narrower RO cusps, but otherwise the resulting shoreline is little changed from the shore-normal wave case.

Further test simulations have also been conducted with XBeach to investigate the effects of including a 12-hour tidal cycle. These tests suggest that such variations principally act to diffuse the megacusp formation processes in the cross-shore direction but do not fundamentally change the outcome (e.g., Fig. 37). Individual waves are

thought to have a similar diffusive effect, which is roughly balanced between onshore and offshore directions and may be parameterized in XBeach by modifying the model's diffusion coefficient.

The preceding section's analysis of waves shoaling over a "real" bathymetry suggests that irregularities of the rip channel bathymetry itself can also affect the intertidal sediment transport patterns in important ways. Rip channels that are slanted relative to the shoreline may modify wave refraction patterns and shift resulting flow fields to change shoreline erosion and deposition patterns. Sediment deposits just offshore of rip channels (visible as slight "bumps" in contours of Fig. 26, middle panel) may focus additional wave energy into rip channels, resulting in increased erosion. Nearer to the shoreline, rip feeder channels are often detected at Sand City, but because of their smaller scales (sometimes less than a meter wide), these features are most often not resolved on measured bathymetries with grids spaced at 5 or 10 m. By focusing and accelerating the converging flow from the shoals into the rips, these feeder channels likely contribute to strengthening swash-zone counter-circulations and building RO megacusps. Because they were not included on the idealized (or measured) bathymetry for the RO megacusp simulations, model-predicted counter-circulations were relatively weak, and the resulting megacusps were narrower than those seen in the field.

F. SUMMARY AND CONCLUSIONS

To test the hypothesis that beach megacusps can form shoreward of either rip channels or shoals, multi-year video and ADCP time series are analyzed and the XBeach 2DH sediment transport model is tested, adapted, and applied in a series of nearshore simulations. Using measured average wave conditions, XBeach model parameters are calibrated to the mean 1D profile for the steep, terraced rip-channel bathymetry at Sand City, California. When optimal parameter settings are used, the model obtains an equilibrium profile that is somewhat flatter and broader than the measured profile, differing in elevation by an average of 13 cm. XBeach is then applied to hindcast two cases of measured bathymetry change from the 2007 RCEX experiment. In the first test, initialized with bathymetry from May 1 and using either mean daily waves or mean storm

waves, the model predicts the measured May 11 bathymetry with a skill of up to 0.60. In the second test, initialized with bathymetry from May 18, XBeach qualitatively captures the development of three megacusp embayments measured with video on May 25. Although XBeach hindcasts measured bathymetry change reasonably well, it oversmooths the swash contours for larger waves ($H_s \geq 1.5$ m), likely because of an erroneous underweighting of onshore transport due to the wave bores.

A series of 18 idealized simulations is conducted to investigate the formation of megacusps shoreward of rip channel bathymetries. Wave energy and mean water levels are varied and specific conditions leading to either shoal-opposite (SO) or rip-opposite (RO) megacusps are identified. One real and one idealized rip channel bathymetry are used. In model results, SO megacusps tend to be associated with higher mean water levels and larger waves, while RO megacusps occur most often at lower mean water levels. Similar water level data were observed for the two types of megacusps at the Sand City site. However, measured cases of RO megacusp formation at Sand City often occurred under more energetic wave climates (H_s = 1.5 to 2 m), for which XBeach either predicts SO megacusps or rapid smoothing to an alongshore uniform beach.

Two cases of megacusp formation on idealized bathymetry and one on more realistic bathymetry are selected from the above simulations for further analysis, to identify dominant sediment transport contributions to SO and RO megacusp formation in the mean, VLF, and infragravity frequency ranges. At higher mean water levels, shoal-opposite setup maxima at the shoreline create shore-parallel, divergent transport vectors that dig out SO megacusp embayments. At lower mean water levels, pre-existing beach perturbations force rip-opposite mean transport counter-circulations in the swash zone that deepen and steepen RO megacusps. Simulations over the realistic bathymetry initially result in a single, steeper RO megacusp, but then develop several SO megacusps.

In a process-based frequency analysis, transport forcing due to mean advective terms is determined to be most important in all three cases, but the location and effects of this forcing are strongly influenced by the mean water level relative to existing bathymetry. Surprisingly, advective transport components that vary at VLF timescales

also play an important role. Two-hour means of vector transport fields for such VLF components continue to change from one timestep to the next, indicating that some of the VLF oscillations have periods greater than 30 min. For larger waves and higher mean water levels, advective transport forcing due to mean wave asymmetry becomes significant, while sediment diffusion at the shore break is relatively more important under small waves. A more limited analysis is conducted of other potentially important factors such as more extreme waves, tidal cycles, and oblique wave directions. It is suggested that their roles are generally secondary to those played by mean water level, wave energy, and bathymetry shape.

Based on both modeled and measured results, it is concluded that beach megacusps may form on rip channel bathymetries shoreward of either shoals or rip channels, forced primarily by the mean advective sediment transport and by advective transport components oscillating at VLF timescales. The main transport components themselves are shaped by a positive feedback from the changing nearshore and beach morphology, in a manner that is strongly influenced by the mean water level.

THIS PAGE INTENTIONALLY LEFT BLANK

IV. OVERALL SUMMARY AND CONCLUSIONS

A combination of field data and modeling is used to test hypotheses about two common nearshore bathymetric features, rip channels and beach megacusps, both of which are regularly found along the coastline of southern Monterey Bay, California. Multi-year datasets from surf-zone video cameras, ADCPs, and offshore buoys are analyzed, filtered, and compared to determine whether a linear relationship exists between alongshore rip channel migration and alongshore sediment transport. Making use of additional video and ADCP time series along with bathymetric surveys, a 2DH sediment transport model is calibrated and applied to investigate the formation of beach megacusps and identify the most important sediment transport processes.

A. ALONGSHORE RIP MIGRATION AND SEDIMENT TRANSPORT

Daily locations and average alongshore migration rates of surf-zone rip channels are determined from multi-year video datasets at three sites along southern Monterey Bay: Sand City, Fort Ord, and Marina. The CDIP spectral wave propagation model is validated by comparison with nearshore ADCP measurements and then used to refract measured offshore waves into the surf zone, where the CERC formula is applied to generate estimates of concurrent alongshore sediment transport rates. Initial correlation coefficients between daily migration and transport rates are found to be relatively low: $r = 0.01$, 0.44, and 0.38, respectively, at the three sites. A parallel simulation conducted with random Gaussian time series suggests that this is because the migration rates are often not distinguishable above the noise associated with digitization of video data. An expanded CERC transport formulation that also includes the effects of alongshore wave height gradients is also applied to the Sand City site, where such gradients are significant, but it does not significantly improve the daily rate correlations.

Several different filtering methods are used to compare the migration and transport rates in ways that will overcome the noise barrier. When rip migration and sediment transport rates are averaged over eight days, they attain correlation coefficients 50–100% higher than those found with daily rates. The moderate increases in correlation

values emphasize the challenges of accurately representing complex nearshore processes, even after data are filtered. When daily rates are low-pass filtered with a cutoff frequency of 1/(8 days), coefficient values slightly better than those from eight-day-averaged rates at each site are obtained. This type of analysis highlights important longer-period oscillations (such as tidal and seasonal cycles) that might influence alongshore rip migration patterns. When only the 10% of days with the highest transport rates are included from each time series, daily correlation results significantly improve at all three study sites, suggesting that there may be a more limited range of higher-energy conditions over which a linear relationship applies. Correlation coefficients are highest when daily rates are cumulatively summed (integrated): $r = 0.94$, 0.76, and 0.87 at Sand City, Fort Ord, and Marina, respectively. Cumulatively summed migration and transport rates can be used to track the mean migration of each rip field and the net amount of sediment transported north or south along the beach at each site. Plots of these quantities suggest that rip migration might lag behind sediment transport, particularly in milder summer months when the minimum energy and transport levels necessary for migration may not be attained by the smaller waves. Correlations at the Sand City site remain anomalously low for all filtering methods except cumulative summing, likely owing to the site's sheltered location and the effects of nearby irregularities in the shoreline.

On the basis of the moderate to high correlations obtained between migration and transport rates with the above filtering methods, it is concluded that the alongshore migration rate of rip channels may be expressed as a linear function of the local alongshore sediment transport rate over longer timescales.

B. MEGACUSPS ON RIP CHANNEL BATHYMETRY

Model parameters for the XBeach 2DH sediment transport model are calibrated to the mean 1D profile for the steep, terraced rip-channel bathymetry at Sand City, California. While previous studies with fixed shoreline models have been unable to predict beach evolution, XBeach has a movable shoreline and is capable of simulating even smaller-scale erosion and accretion of the beach face and dunes. In multiple simulations, the model is initialized with average measured waves and varying parameter

settings and allowed to simulate profile evolution until a quasi-equilibrium state is reached. Optimal parameters are extracted from the simulation that best matches the measured mean profile. XBeach is then tested by hindcasting two cases of measured bathymetry change from the 2007 RCEX experiment. In the first test, the model predicts the measured bathymetry evolution over a ten-day period with a maximum skill of 0.60. In the second test, XBeach qualitatively captures the development of three megacusp embayments that develop over a five-day period following the experiment. The model tends to significantly oversmooth the intertidal bathymetry for larger waves ($H_s \geq 1.5$ m), likely because of an underweighting of onshore transport due to wave bores. Oversmoothing is less of a problem under moderate waves ($H_s \sim 1$ m), as long as simulations are limited to a few days.

The formation of megacusps shoreward of rip channel bathymetries is investigated with a series of 18 idealized simulations in which wave energy and mean water levels are varied. One real and one idealized rip channel bathymetry are used. Specific conditions leading to either shoal-opposite (SO) or rip-opposite (RO) megacusps are identified. In model results, SO megacusps tend to be associated with higher mean water levels and larger waves, while RO megacusps occur most often at lower mean water levels. Video and tidal data from the Sand City site tend to confirm the role of mean water levels that is suggested by XBeach. However, under more energetic wave climates (H_s = 1.5 to 2 m), XBeach either predicts SO megacusps or rapid smoothing to an alongshore uniform beach, while these conditions are most often observed with RO megacusps at Sand City.

From the above simulations, two cases of megacusp formation on idealized bathymetry and one on realistic bathymetry are further examined to identify dominant sediment transport contributions to SO and RO megacusp formation in the mean, VLF, and infragravity frequency ranges. An examination of mean flow fields when mean water levels are higher suggests that setup at the shoreline is highest shoreward of the shoals, where it creates an alongshore-directed, diverging flow field that carves out SO megacusp embayments. At lower mean water levels, converging flow from feeder

currents creates counter circulations within pre-existing beach perturbations shoreward of the rip channels, and the perturbations are widened and steepened into RO megacusps. Simulations over the realistic bathymetry are more complex, initially creating single, steeper RO megacusp, but then also building several mild-sloped SO megacusps.

In a process-based frequency analysis, XBeach is modified to decompose advective and diffusive sediment transport terms into mean, VLF, and infragravity ranges and track their relative sizes. Forcing due to mean advective sediment transport components (i.e., $\overline{hC}\overline{u}$ and $\overline{hC}\overline{v}$) is determined to be most important in all three of the above selected cases, but the location and effects of this forcing are found to be strongly influenced by the mean water level relative to existing bathymetry. Although their contributions are averaged over a two-hour period, advective transport components varying at VLF timescales also play an important role, indicating that some of the VLF oscillations have periods greater than 30 min. For larger waves and higher water levels, advective transport forcing due to mean wave asymmetry becomes significant, while sediment diffusion at the shore break is relatively more important under smaller waves. This analysis does not fully address other potentially important factors such as larger waves, tidal cycles, and oblique wave directions, but preliminary analysis suggests that their roles are less important than those played by mean water level, wave energy, and bathymetry shape.

Based on both field data and model results, it is concluded that beach megacusps may form on rip channel bathymetries shoreward of either shoals or rip channels. The primary forcing is provided by the mean advective sediment transport and by advective transport components oscillating at VLF timescales. The changing nearshore and beach morphology are strongly influenced by the mean daily water level and can also have a significant feedback effect on the main transport components, ultimately making the mean transport increasingly dominant over the oscillating components.

APPENDIX

Daily migration-transport rate correlations can be weakened by a variety of measurement errors intrinsic to the process of recording these datasets. As discussed in Chapter II, measurement uncertainty for rip locations at each site is expected to be roughly Gaussian-distributed. When migration rates of multiple rips are averaged, the mean error is reduced as the number of averaged rip timelines (*N*) increases:

$$\varepsilon_{avg} = \frac{1}{N}\sum_{n=1}^{N}\varepsilon_n \ , \tag{21}$$

where ε_{avg} represents the error in the averaged rip migration rate for a given day and ε_n is the Gaussian-distributed migration rate error for each individual rip. For simulated, random migration rate errors that are Gaussian-distributed with zero mean and a standard deviation of 8.5 m, Eq. 21 results in an averaged error distribution with standard deviation ranging from 2.5 m (for 12 rips) to 4.2 m (for four rips). Positive and negative errors can be summed in the equation because they are treated as a continuous sequence of values.

On the southern Monterey Bay coastline, where wave approach is close to shore normal year-round, accurate values for incident angles are essential to accurate alongshore sediment transport estimates. Maximum achievable accuracy for breaking wave angles, however, is probably ±3º owing to errors in wave direction, shoreline orientation, and/or model bathymetry. While wave directional uncertainties at offshore buoys can be ±5º, they are smaller owing to refraction and Gaussian-distributed at breaking depth, and thus unlikely to cause a consistent incident angle bias.

Incorrect shore normal orientation is the most likely source of wave angle bias. In this study, shore normal was measured by multiple methods, including smaller scale (O(200m)), shore-based GPS and theodolite surveys, estimates derived from nearshore bathymetry contours, and larger-scale linear fits to several kilometers of average coastline data. For the Sand City site, results range from 310º to 312º true north. Although the lowest value, 310º, was adopted for this study, comparisons with mean rip migration data

suggest that the site's coastline may be even more westward-facing (see Fig. 11). If the shore normal is arbitrarily shifted to 307º, adjusted alongshore transport results then exhibit seasonal oscillations that appear more like those in the rip migration data. At Marina, a shore-normal angle of 280º instead of 282º visually improves the fit of mean rip migration and net transport. However, in each case overall correlations of migration and transport rates decline rather than increase.

Errors in modeled bathymetry are the likely source of small (< 5º) directional biases that are often identified in CDIP-modeled wave angles. In southern Monterey Bay, several of the NOAA bathymetric surveys used by CDIP were acquired in the early 1930s (National Oceanic and Atmospheric Administration, 2010b) and depths in some areas may have changed significantly. To check for a consistent directional bias in model output at Sand City, mean directions were computed and compared for each frequency bin using CDIP-modeled and ADCP-measured wave spectra in 2006–07. Because the directional spread at the site is nearly as small as the uncertainties in ADCP directional measurements, a definitive conclusion was not reached. ADCP mean directions were generally similar to CDIP values, and average model bias did not exceed one degree for any frequency bin.

In the extended CERC formulation calculations, additional errors may have resulted from incorrect values of alongshore wave height gradients, estimated for Sand City using the large-scale, simplified two-point difference method described in Section IID. The accuracy of that technique was tested by computing gradients over a six-month period for smaller-scale alongshore ranges of 1–3 km (5–15 data points) surrounding the Sand City site and compared to $\partial H_{rms,0} / \partial y$ values estimated with the two-point method. Gradients generated using the shorter ranges were found to have 6–10 times greater variability than those estimated using the simplified two-point method, but mean gradients over the period were nearly the same (within 5% for the 2–3 km ranges), suggesting that the estimate used in this analysis is a reasonable approximation over the longer term.

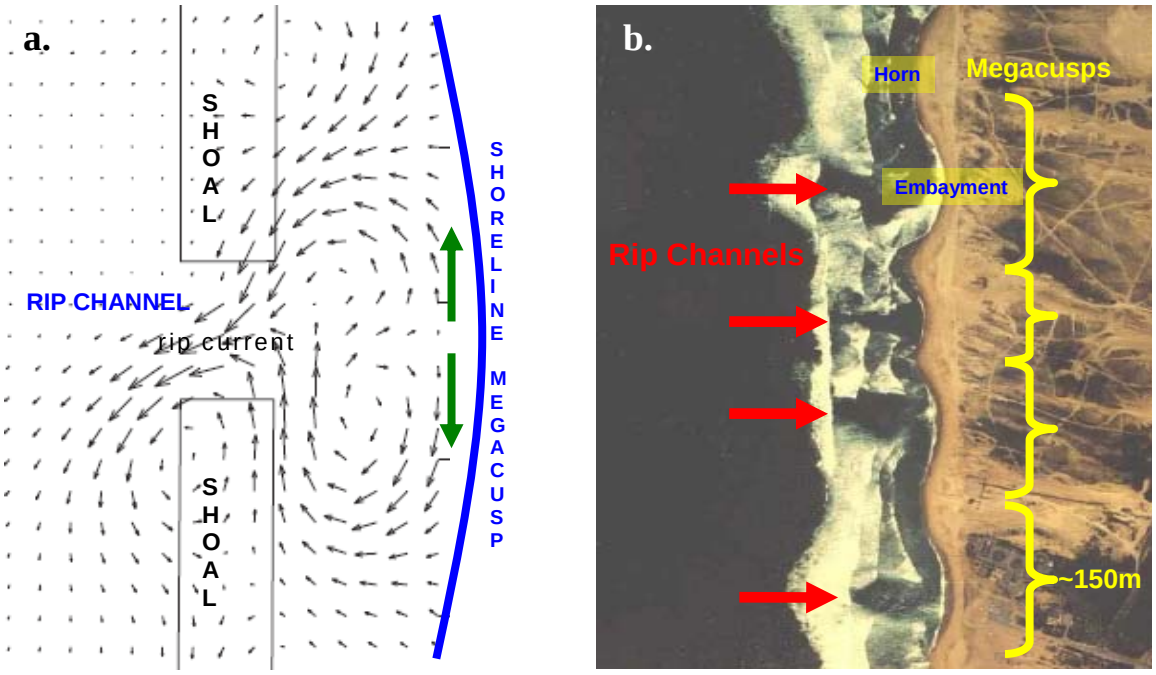

Figure 1. (a) Idealized rip current flow-field (from Haas, Svendsen, Haller, & Zhao, 2003), including offshore-directed rip current, which cuts a deeper rip channel through the alongshore bar. Shoreward of the rip, feeder currents converging into the channel generate diverging swash-zone counter-circulations (green arrows), which may contribute to widening the megacusp embayment at the shoreline. (b) Aerial photograph of section of Monterey Bay showing alignment of surf zone rip channels (red arrows) with shoreline megacusps (yellow brackets). Principal megacusp features include an embayments, where the beach is narrower, and horns, where the beach is wider.

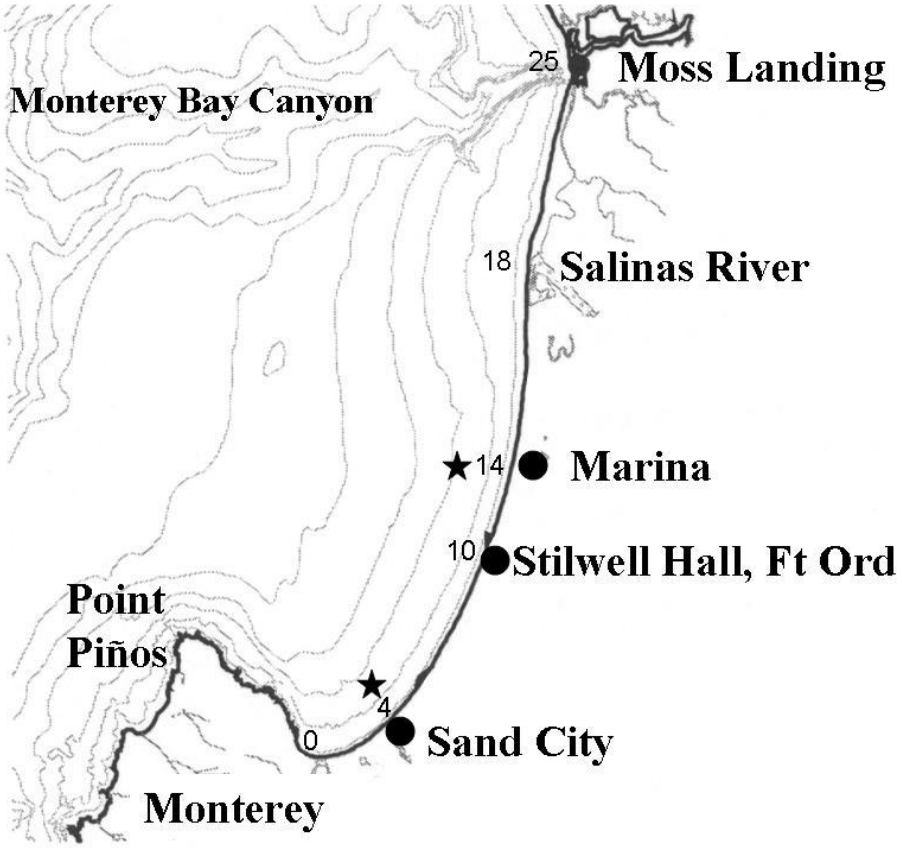

Figure 2. Three video sites (circles) and two nearshore (13-m depth) ADCP sites (stars) along southern Monterey Bay, California, which were used in the study. Alongshore distance (km) from the southern end of the bay is indicated for each site and various other landmarks. (The Marina site was shut down in 2009.)

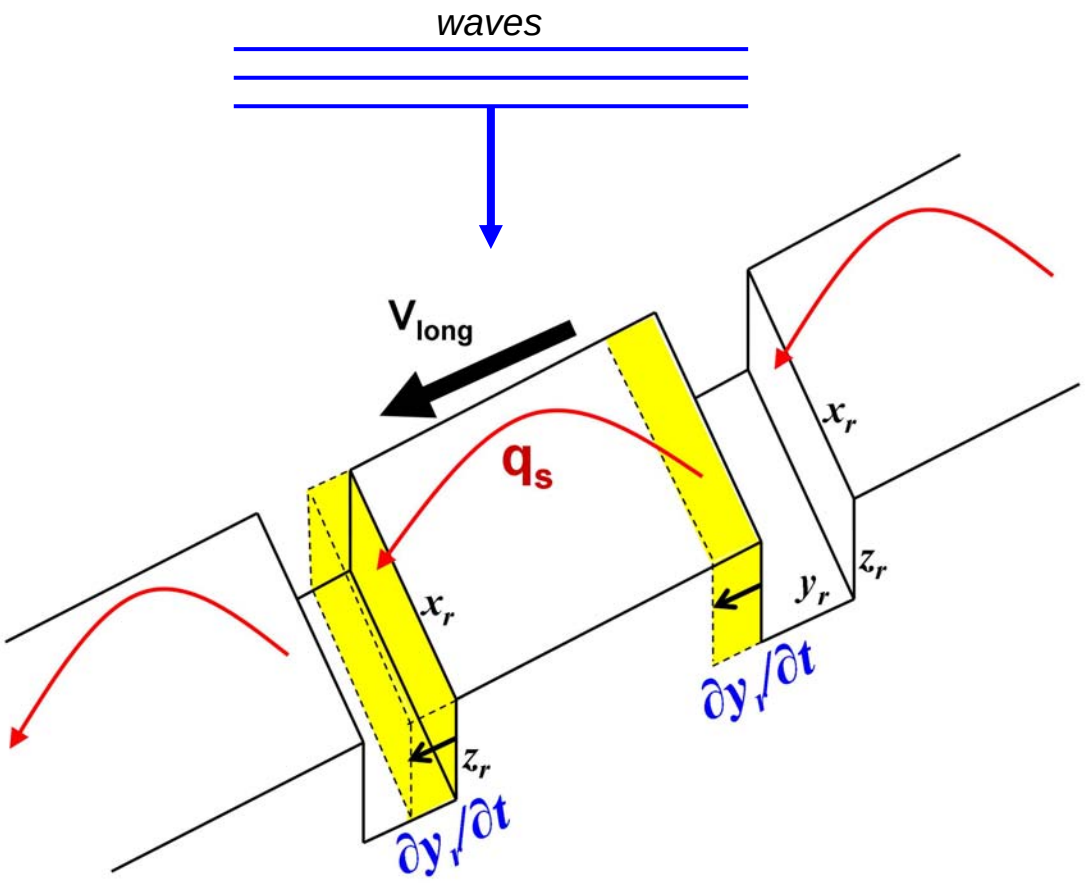

Figure 3. Simplified picture of relationship between alongshore rip migration rate and alongshore sediment transport rate. Rip channels are treated as rectangular holes in a flat seabed, each of length x, width y, and depth z. Waves approaching at an angle generate an alongshore current, V_{long}, that flows in a direction perpendicular to the channel axes. Alongshore flow removes sediment from the downflow side of each channel and deposits it on the upflow side of the next one, so that the channels migrate in the same direction as the transport. The transport rate, q_s, will be linearly proportional to the alongshore distance, $\partial y_r / \partial t$, traveled by each migrating channel: $q_s \sim x_r \cdot y_r \cdot \left(\partial y_r / \partial t\right)$

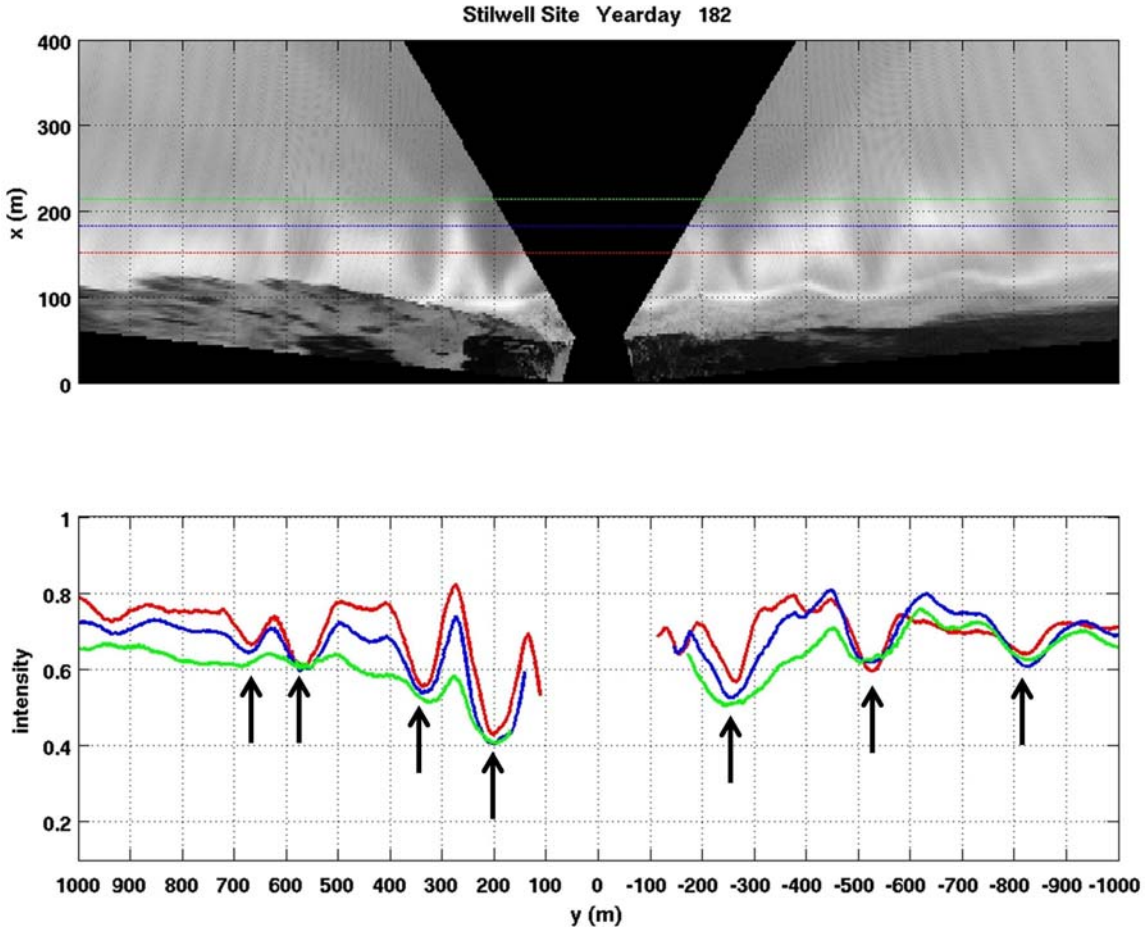

Figure 4. Example of intensity image and transects used for visually marking alongshore rip channel locations. Top panel shows time-averaged image from Stilwell site, transformed to an overhead perspective. White regions correspond to surf-zone areas of consistent wave breaking, while offshore-directed, darker regions between them delineate rip channels. Bottom panel plots image intensity versus alongshore location for the three colored alongshore transects of the rectified image (red: 150 m; blue: 180 m; green: 210 m). Selected intensity minima corresponding to rip locations are indicated with vertical arrows.

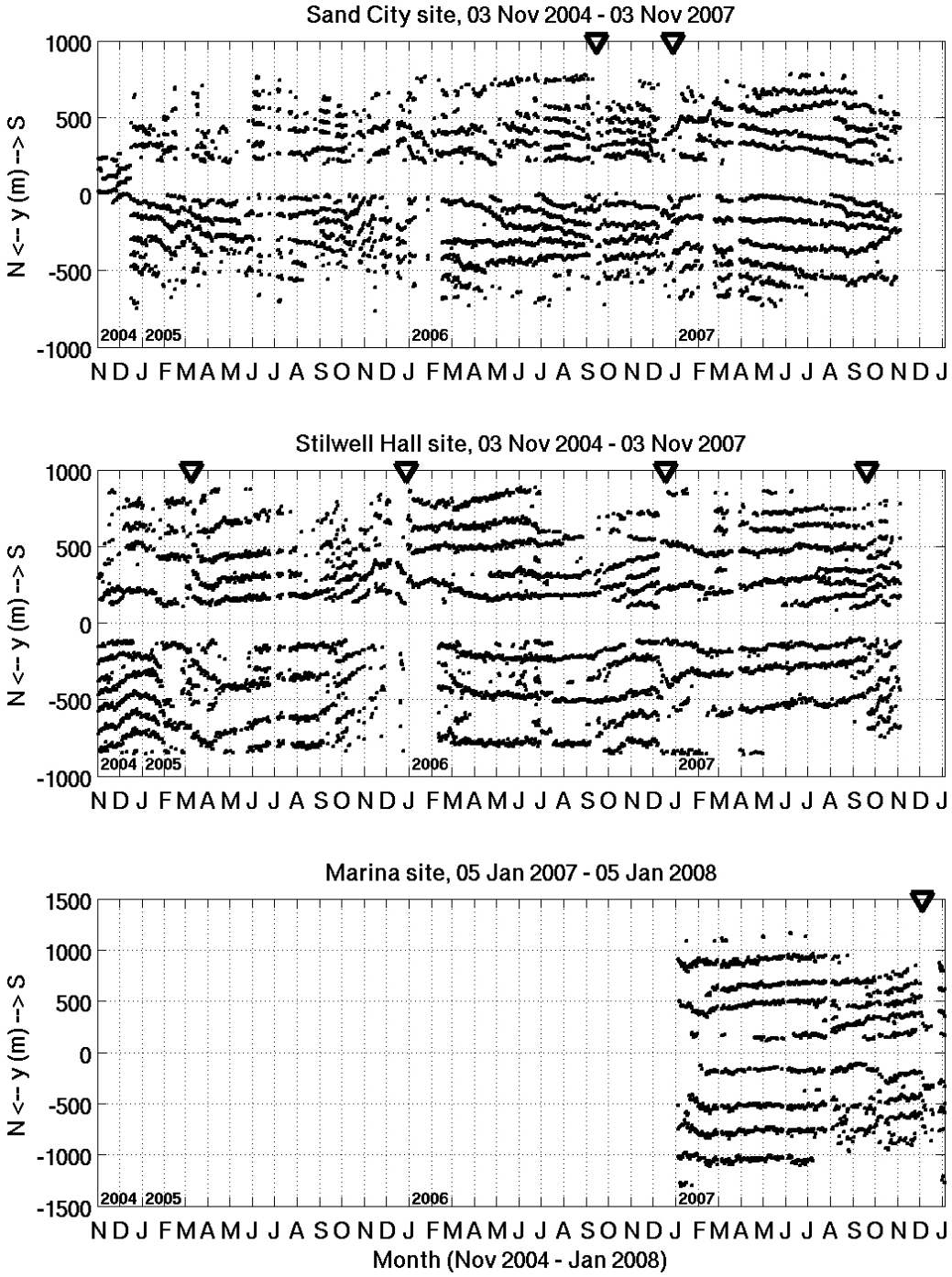

Figure 5. Timestacks of rip channel locations at Sand City (top panel), Stilwell (middle), and Marina (bottom) camera sites. In each panel, individual selected rip locations are plotted as single points for each day, with alongshore location on the y-axis (positive southward) and time on the x-axis. Three years of video data are available for the Sand City and Stilwell sites; only one year is available for Marina. Approximate times of full or partial resets are marked with arrows along the top of each panel.

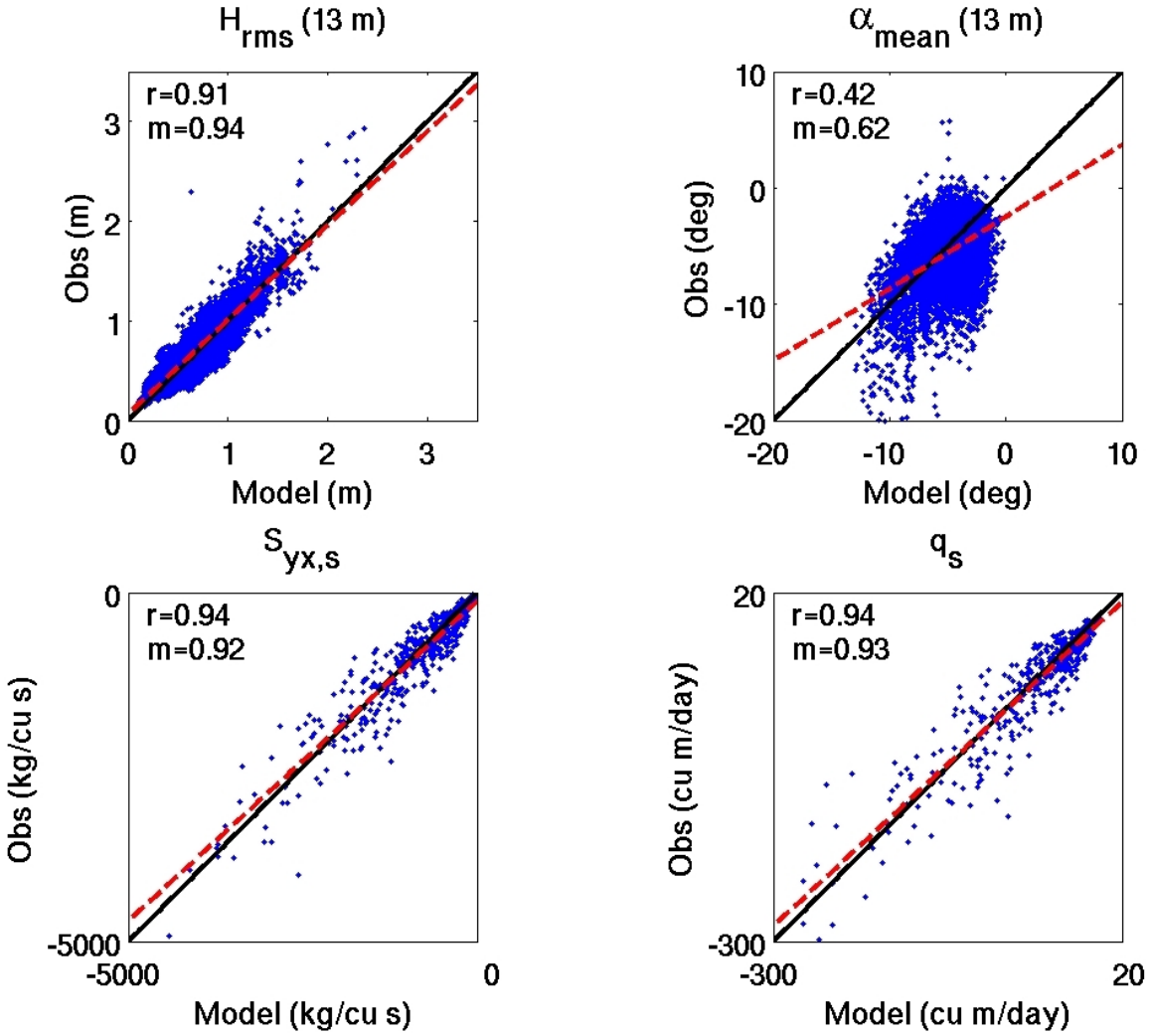

Figure 6. Comparisons of model predictions with ADCP observations at Sand City between June 2006 and October 2007 with correlation coefficients (r) and slopes (m) in upper left corner. While the correlation of CDIP- and ADCP-predicted rms wave heights, H_{rms}, at 13 m depth is high (top left), mean direction α_{mean}, correlation is relatively poor (top right). The mismatch of directions is not surprising, as both modeled and measured directional spreads at Sand City are roughly the same size as the estimated ADCP measurement error (i.e., about ±5°). In spite of this, CDIP-model-based predictions of offshore radiation stress, $S_{yx,s}$, and sediment transport rates, q_s, in the surf zone correlate well with ADCP-based calculations (bottom). Positive is southward for α_{mean}, $S_{yx,s}$, and q_s.

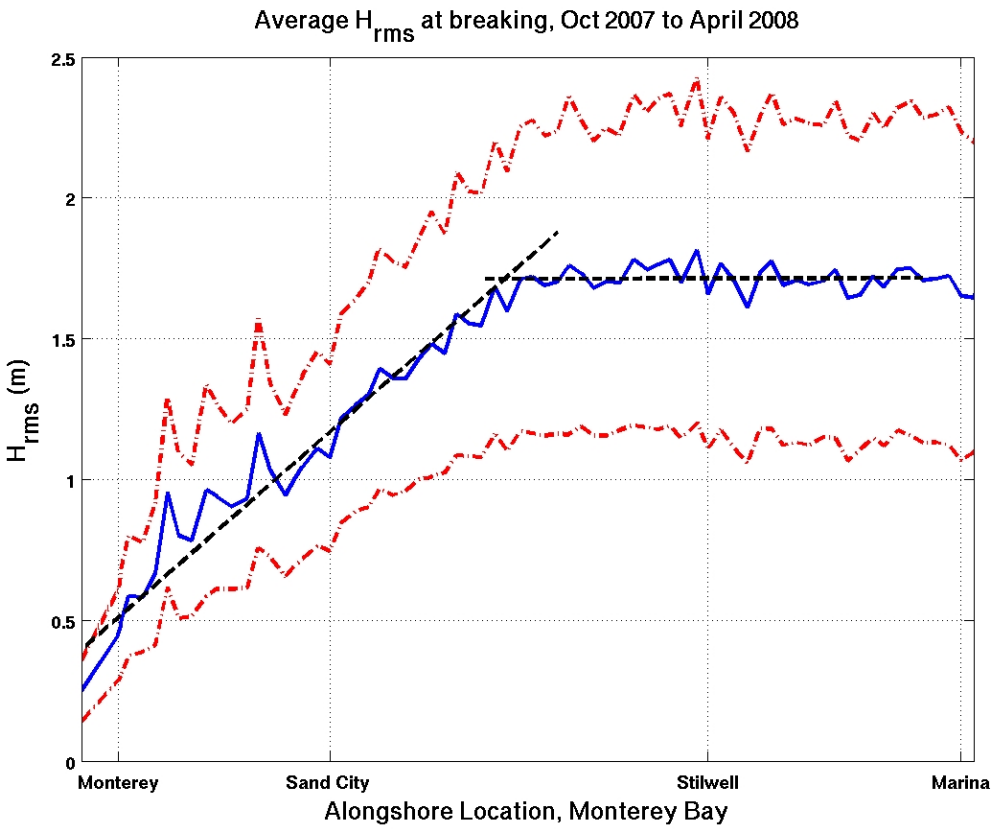

Figure 7. Model-predicted rms wave heights at breaking along the shoreline of southern Monterey Bay, averaged over six months. Data spread (± one standard deviation) is shown by dash-dot lines. Dashed lines on top of main curve indicate mean alongshore slopes of wave heights on southern and northern sections of the shoreline between Monterey and Marina. While wave heights remain relatively constant over the northern half of this range, there is a wave height gradient (~ 1/4000) further south, indicating that alongshore variations in radiation stress component S_{yy} and setup will have a stronger effect on alongshore transport for that section of coastline.

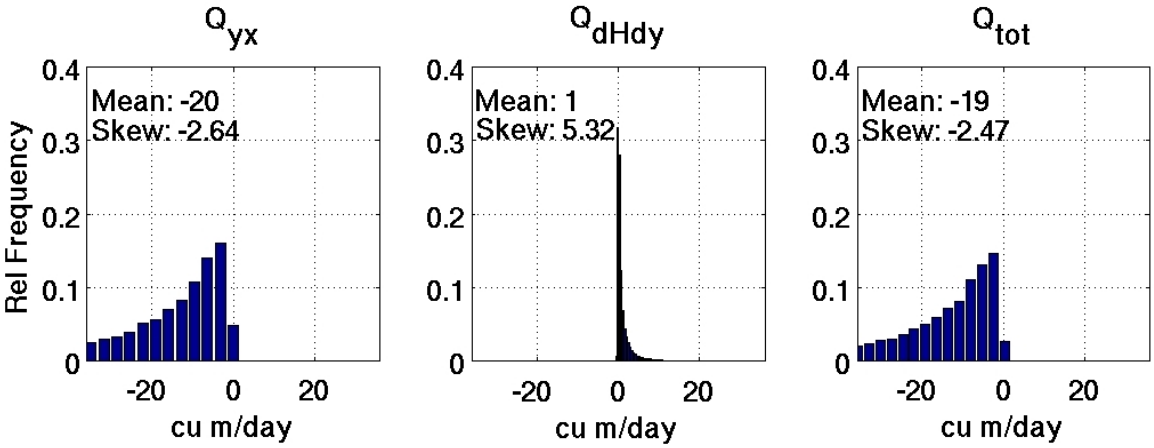

Figure 8. Relative frequency distributions of estimated sediment transport contributions over three years at Sand City due to $S_{yx,s}$ (Eq. 1; left panel), $\partial H/\partial y$ (second term in Eq. 2; center panel), and total overall transport including both contributions (full Eq. 2; right panel). Transport due to $S_{yx,s}$ is almost entirely negative, leading to a purely northward alongshore transport. In contrast, the contribution due to the alongshore wave height gradient is smaller, but largely positive. When contributions are summed, the resulting distribution has a less negative mean and skewness, but continues to exhibit a strong northward bias.

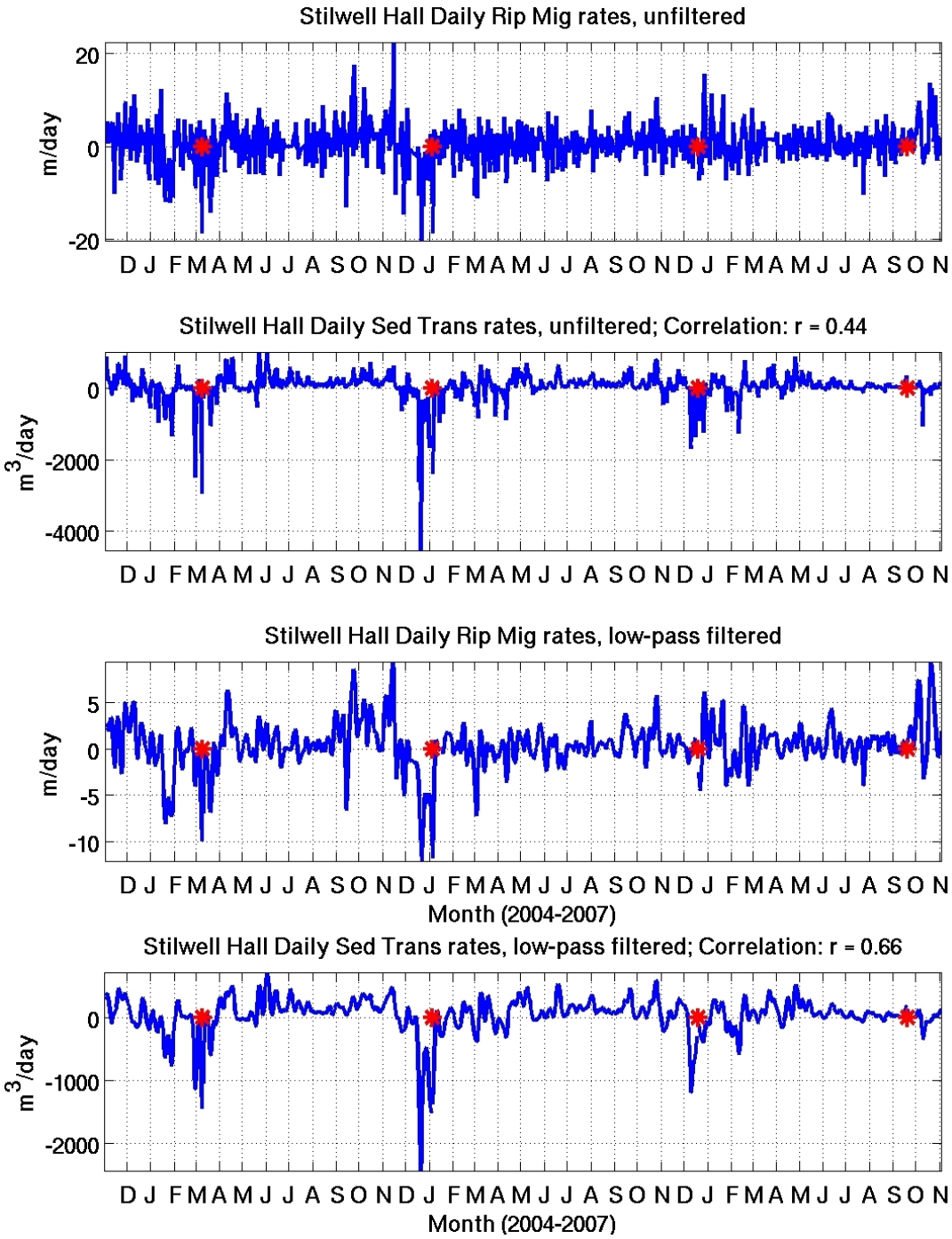

Figure 9. Time series of measured alongshore rip channel migration and CERC model sediment transport for Stilwell Hall site before and after low-pass filtering. Top two panels show unfiltered rates, which have correlation r=0.44 for non-reset days. For bottom two panels, a fourth-order Butterworth low-pass digital filter is applied to each time series with f_{max}=1/(8 days), improving the correlation to r=0.66. Excluded reset days are marked with asterisks on each panel.

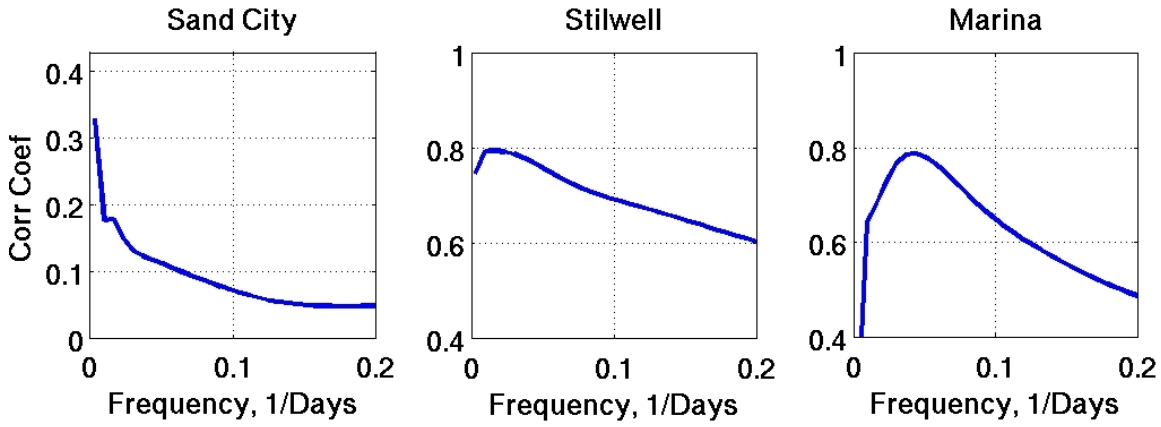

Figure 10. Variation of correlation coefficient between daily rates of rip migration and sediment transport as a function of the low-pass cut-off frequencies ranging from 1/(360 days) to 1/(5 days). Highest correlations are achieved for lower frequencies, although peak correlation does not always coincide with the lowest frequency, likely because of seasonal irregularities. The steep drop in correlation at Marina occurs at 1/(360 days), because this corresponds to the entire length of the dataset.

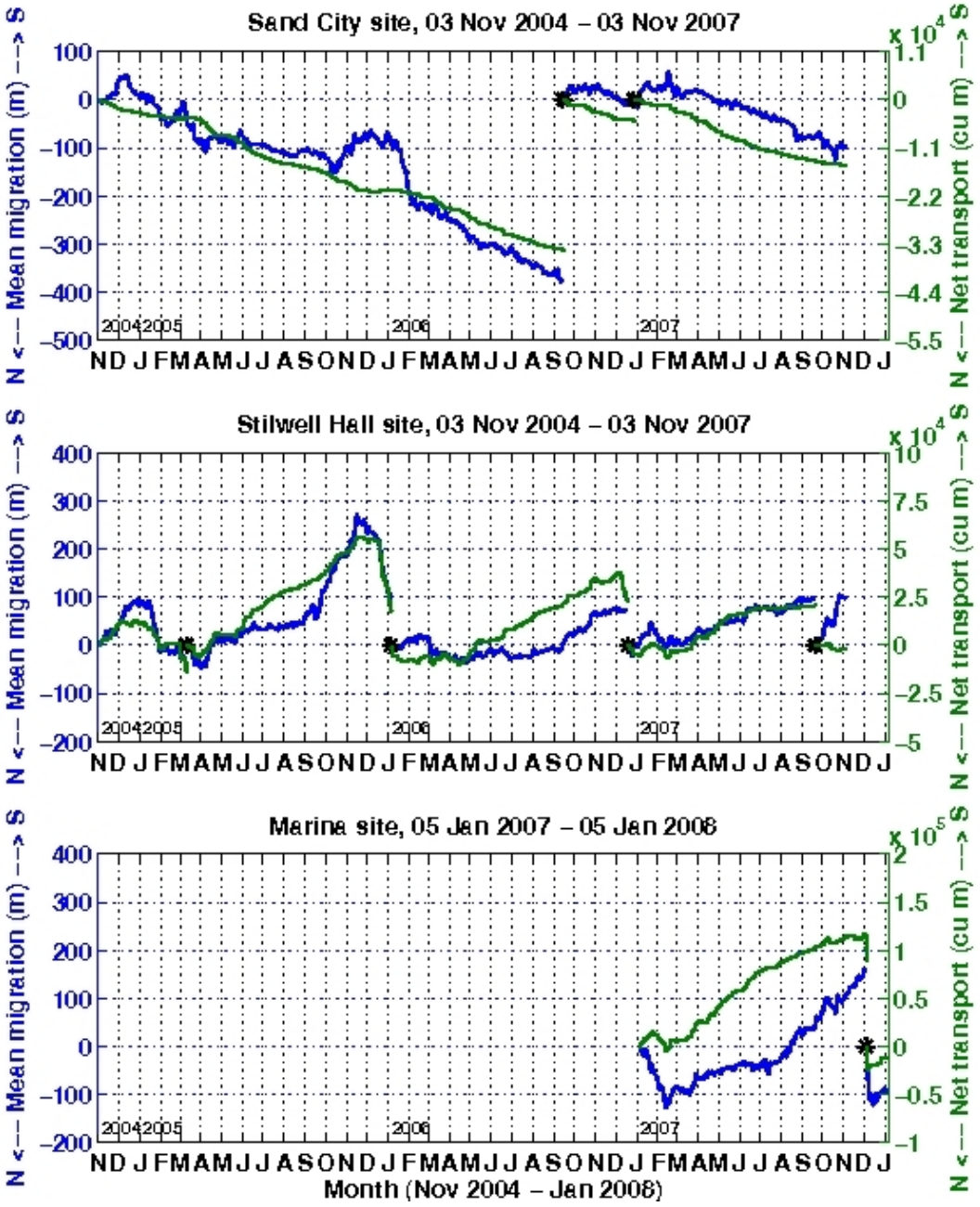

Figure 11. Mean rip migration (blue, left scale) and sediment transport (green, right scale) for the three video study sites, calculated by cumulatively summing mean daily rates. The generally uniform migration and transport direction at Sand City contrasts with oscillatory behavior seen at Marina and Stilwell, though seasonal oscillations are apparent at all three sites. Significant northward migration and transport are consistently seen at all sites in December to March, while a southward trend is generally apparent between September and December. Visually identified rip field resets are marked with asterisks.

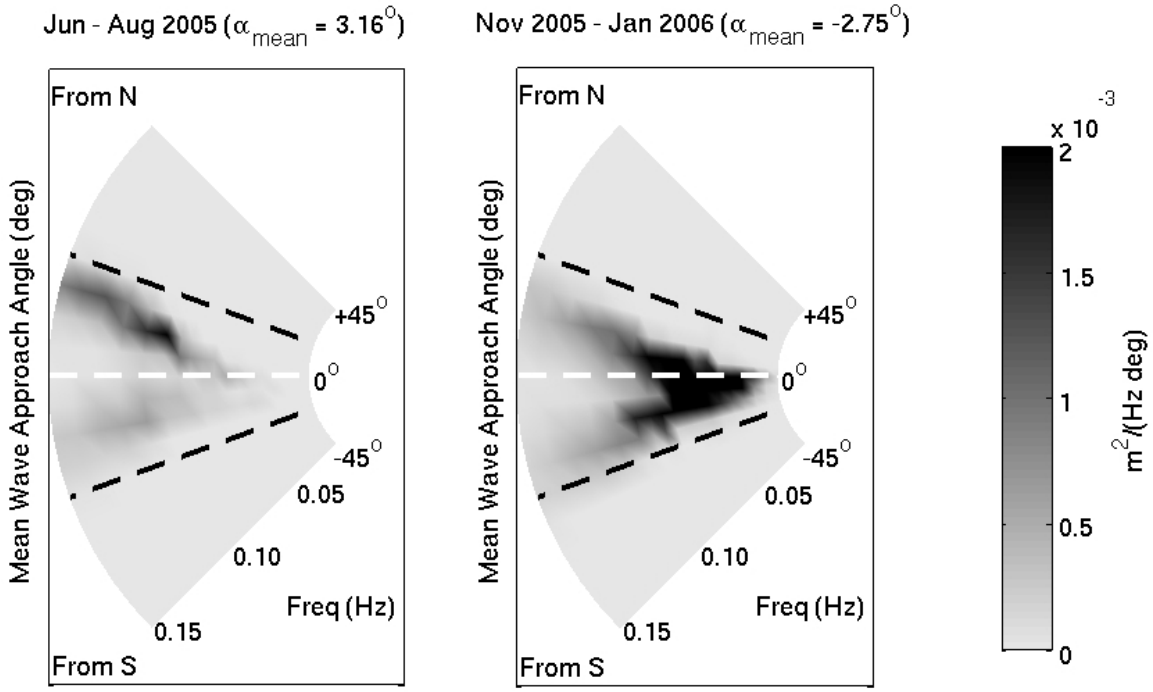

Figure 12. Wave roses showing mean wave directions and frequencies at 15 m depth, offshore of Stilwell site, as estimated by CDIP spectral refraction program. Directions are relative to shore normal. Left panel represents three months in summer of 2005 ($H_{rms,avg}$ = 0.73 m), and right panel represents three months in winter of 2005–06 ($H_{rms,avg}$ = 1.27 m). Mean approach angle for entire period, α_{mean}, is 3º north of shore normal in summer and 2.8º south of shore normal in winter. Black dashed lines on each panel correspond to ±20º, confirming that nearly all wave approach angles for both time periods are contained within a range that is close to shore normal (white dashed line).

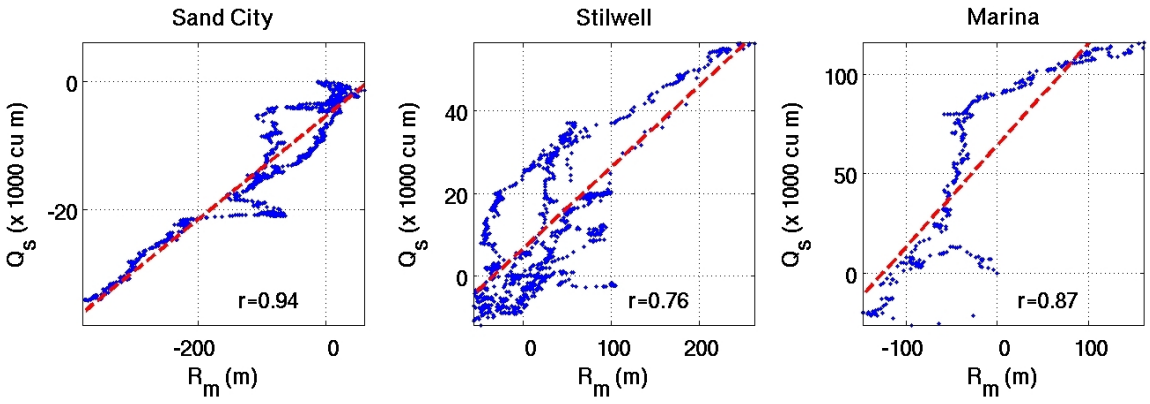

Figure 13. Correlations of mean rip migration, R_m, and net sediment transport, Q_s (as predicted by the CERC formula) for the three study sites. The linear least-square best fit is indicated by the dashed line. Correlation coefficients are provided in the lower right corner.

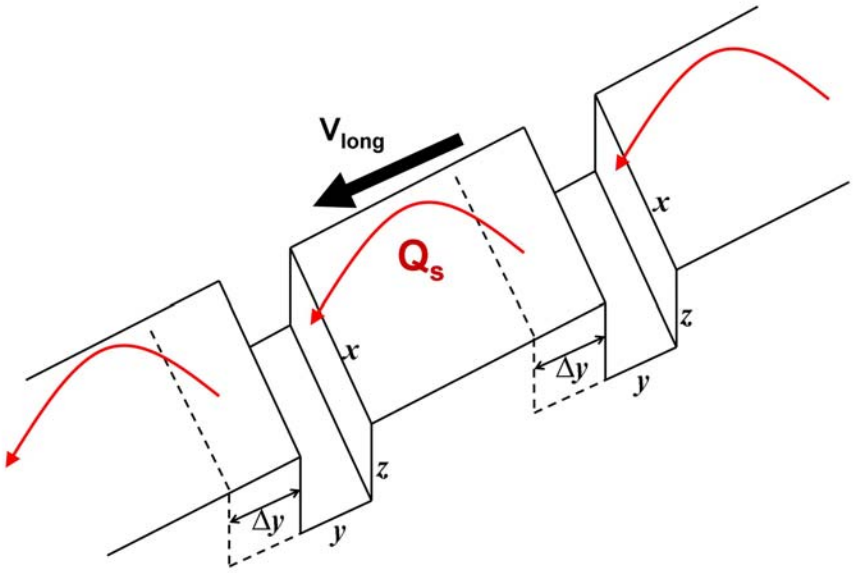

Figure 14. Simplified picture of relationship between mean rip migration and net sediment transport. Rip channels are treated as rectangular holes in a flat seabed, each of length x, width y, and depth z, with alongshore current flowing in a direction perpendicular to the channel axes. If alongshore flow removes sediment from the downcoast side of each channel and deposits it on the upcoast side of the next one, the channels will migrate in the same direction as the transport. Net transported volume will be proportional to the amount removed from the downcoast side of each rip and thus linearly proportional to the alongshore distance, Δy, traveled by each migrating channel: $Q_s \sim xz\Delta y \sim \Delta y$.

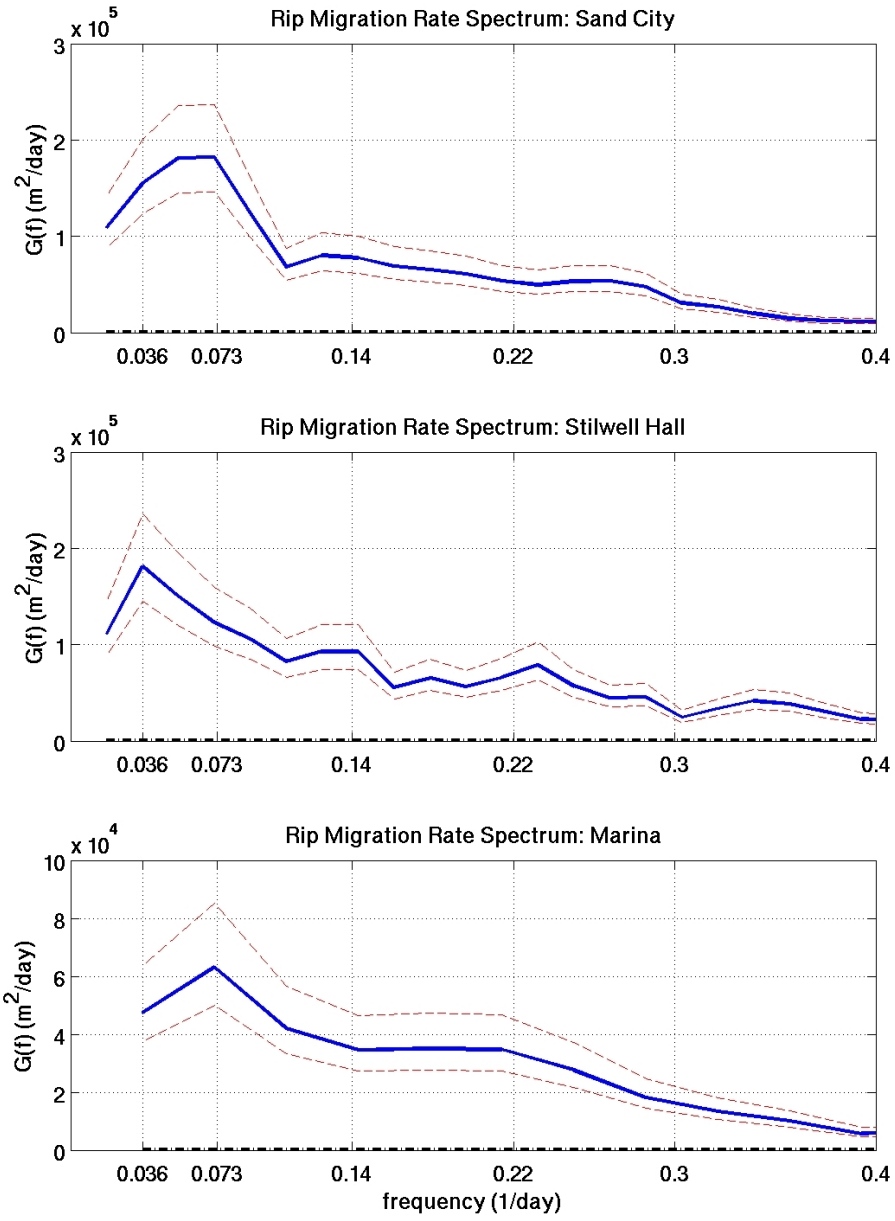

Figure 15. Frequency spectra of daily rip migration rates for inter-reset periods at the three study sites. Eighty percent confidence intervals are indicated by dashed lines. The three-year data set at Stilwell shows a significant spectral peak at approximately 0.036 days^{-1} (28-day period) and suggests a second peak at approximately 0.14 days^{-1} (seven-day period). A significant peak also occurs near 0.073 days^{-1} (14-day period) for the three-year Sand City and one-year Marina datasets. This may signal the influence of the lunar tidal cycle on alongshore sediment transport patterns, or the existence of an optimal depth for accelerated rip migration. The noise floor corresponding to a variance of (8.5 m/day)^2 is shown on each set of axes as a heavy dash-dot line, to emphasize the relative strength of these signals.

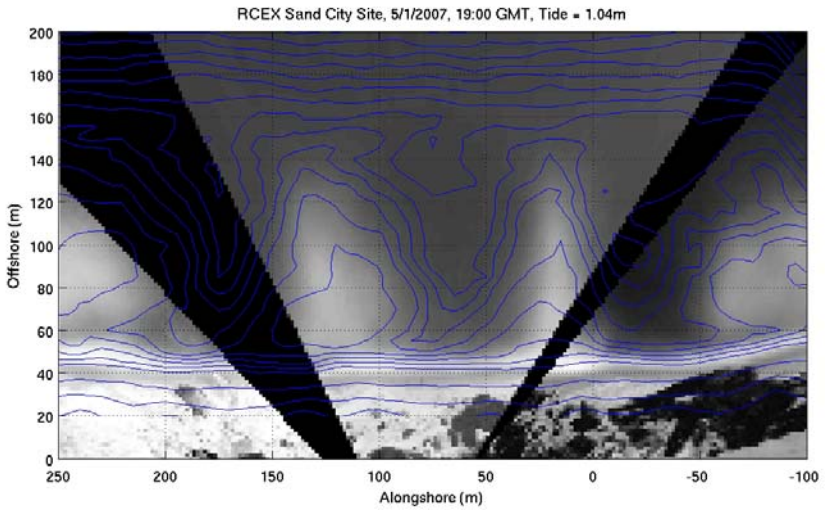

Figure 16. Comparison of rectified video with measured bathymetry at the Sand City site, May 1, 2007. Blue contours of bathymetry measured with GPS-equipped PWC are traced on top of 20-minute time-averaged, rectified image from three cameras (dark wedges are regions where the cameras did not overlap). On video image, white areas in the surf zone indicate wave breaking over shoals, while dark areas capture deeper rip channel locations. Light and dark surf-zone video regions match the measured shoals and rip channels reasonably well, and the general shape of the shoreline is also captured by the video. Note that beyond the surf zone, depth contours are essentially straight and parallel.

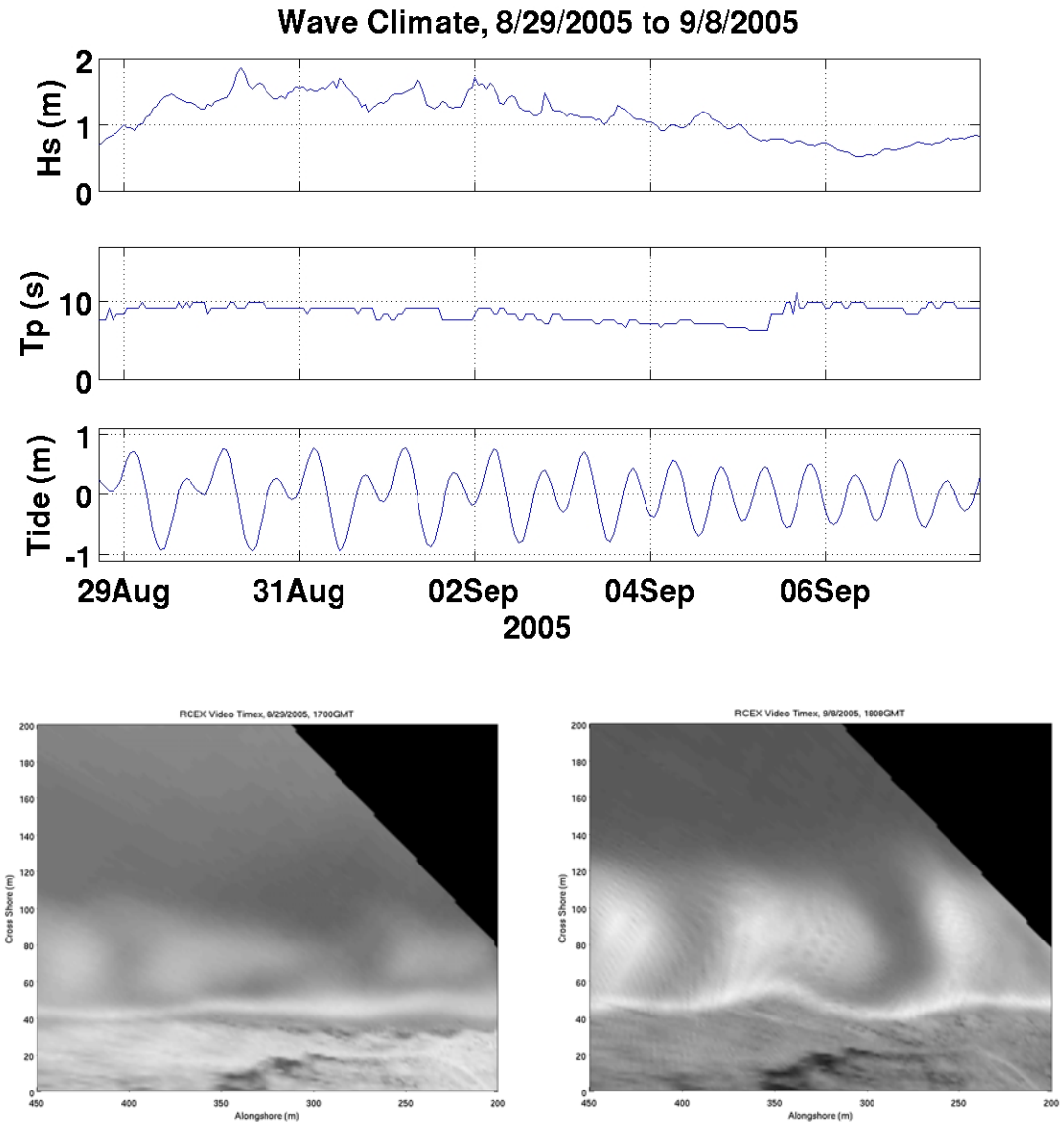

Figure 17. Top two panels show significant wave height (H_s) and peak period (T_p) measured at 13m depth over 10 days in Aug – Sep 2005. Third panel shows tide for the same period, relative to MSL. Bottom two panels are rectified images from the site at the beginning and end of this period, respectively, and show the development of megacusps along a shoreline that was initially straight.

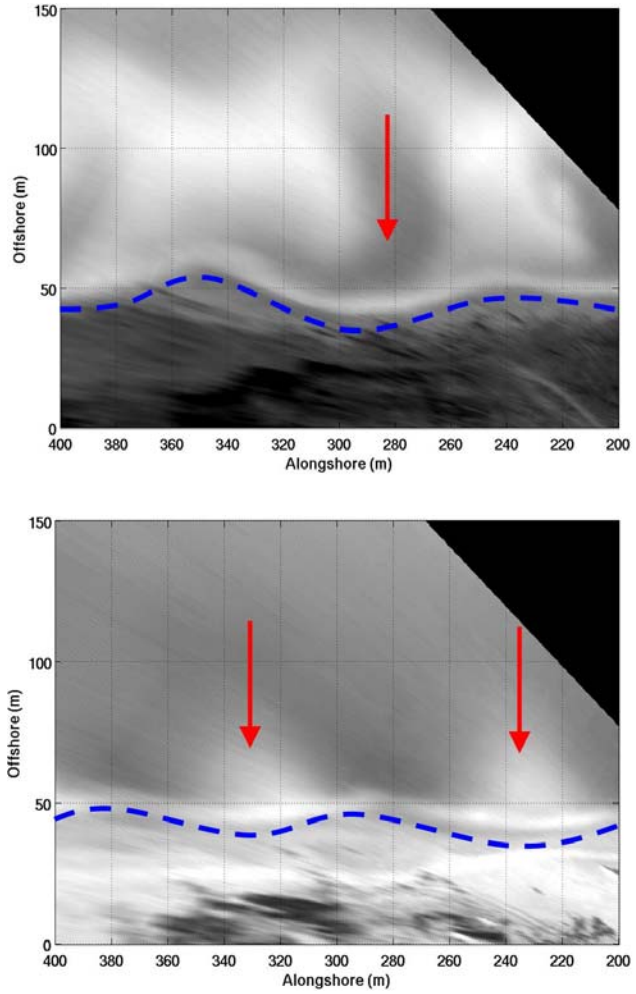

Figure 18. Sample time-averaged, rectified images recorded at the Sand City site. Approximate shoreline is traced near bottom of each image (dashed line) and offshore is at top. Arrows mark alongshore locations of megacusp embayments. In top image, embayment is shoreward of the rip channel ("rip-opposite" or RO), while in bottom image the embayments appear to be shoreward of the shoals ("shoal-opposite" or SO). For the top image (recorded in September 2005, tide ~ MSL), H_s values in the preceding days approached 2 m, with T_p around 10 s. For the bottom image (November 2008, tide = MSL + 0.7 m), preceding wave heights averaged around 0.7 m, while peak periods ranged from about 6–12 s.

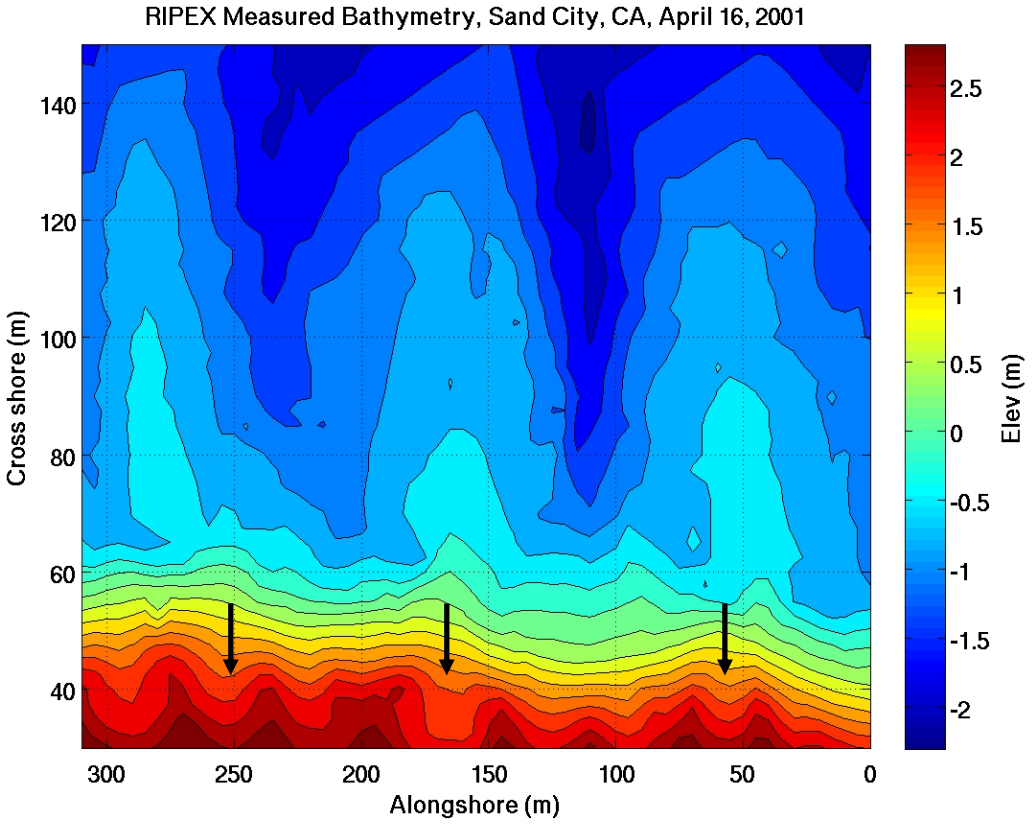

Figure 19. Section of bathymetry from 2001 RIPEX experiment, featuring rip-opposite (RO) cusp contours in the intertidal region (green and yellow contours) as well as shorter, "swash"-type cusps that start at approximately MSL + 2 m (darker red contours, near bottom of image). The smaller cusps were likely created during a period of sustained higher mean water levels (during spring tides) by waves that were at least partially focused by refracting over the rip channel bathymetry. If this focusing helped to create the shoal-opposite (SO) embayments marked with black arrows above, these data constitute the only directly measured evidence of SO cusps at the Sand City site.

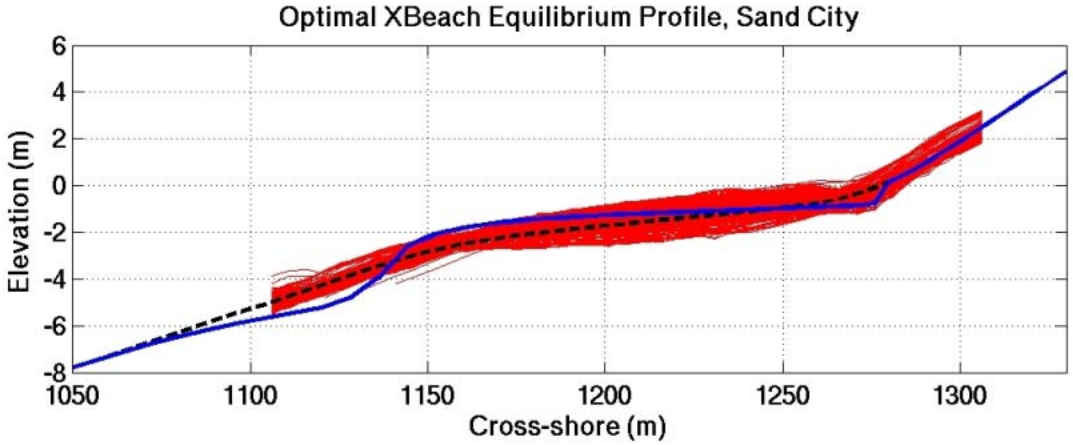

Figure 20. Optimal profile from 1D equilibrium profile calibration tests (blue line). Initial profile (black dashed line) was created by averaging all measured profiles from the Sand City RCEX experiment (red lines), then extended offshore to -30 m and onshore to +10 m. At model equilibrium, all bathymetry elevations changed less than 1 mm in 10 hours. The RMS elevation difference between initial and final profiles is 0.13 m, with a maximum difference of 0.95 m. Except near the offshore boundary, the equilibrium profile remains within the vertical elevation range of the measured profiles.

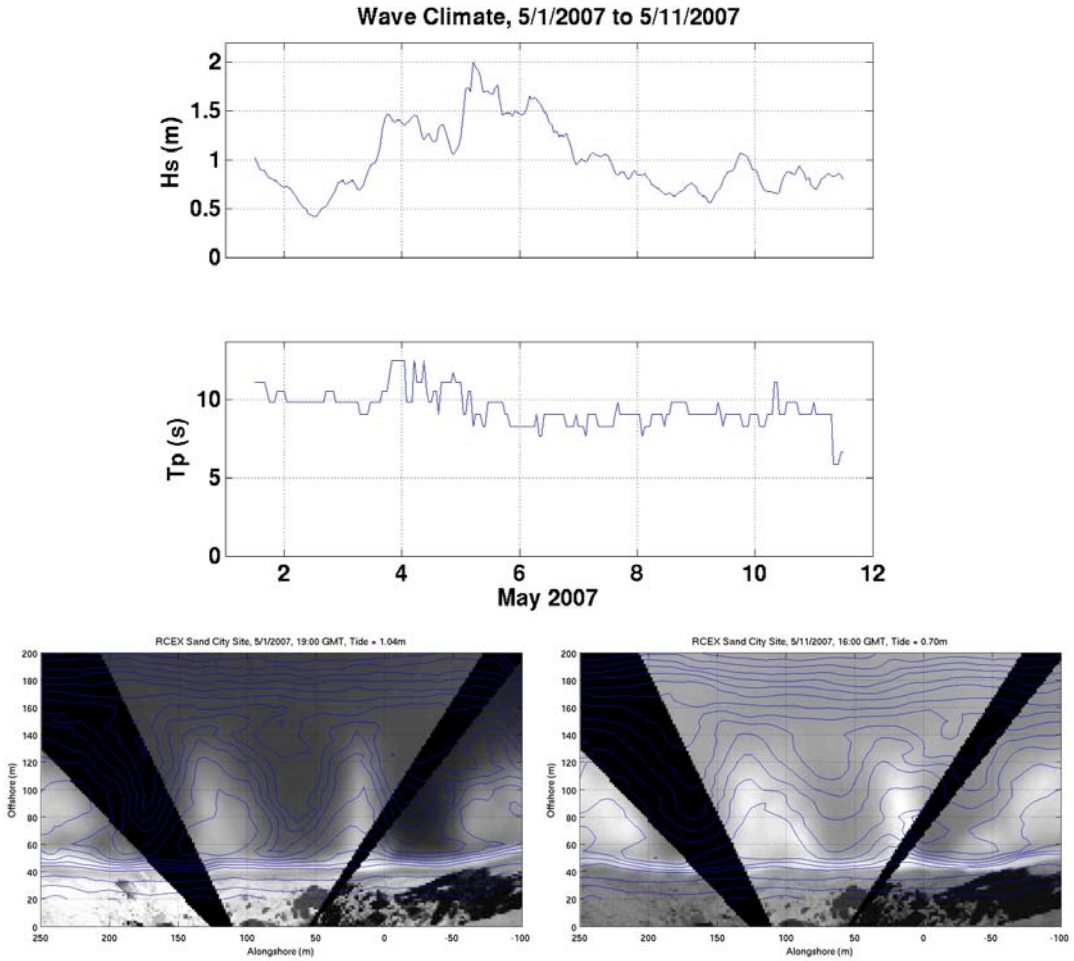

Figure 21. Wave conditions recorded during the 2007 RCEX experiment from May 1–11 (top two panels), including one stormy period that featured moderate-sized waves with significant wave heights up to 2 m. Bottom two panels show video images from initial and final days of this period, overlaid with measured bathymetry contours. These data are used in the 2D skill test of the XBeach model.

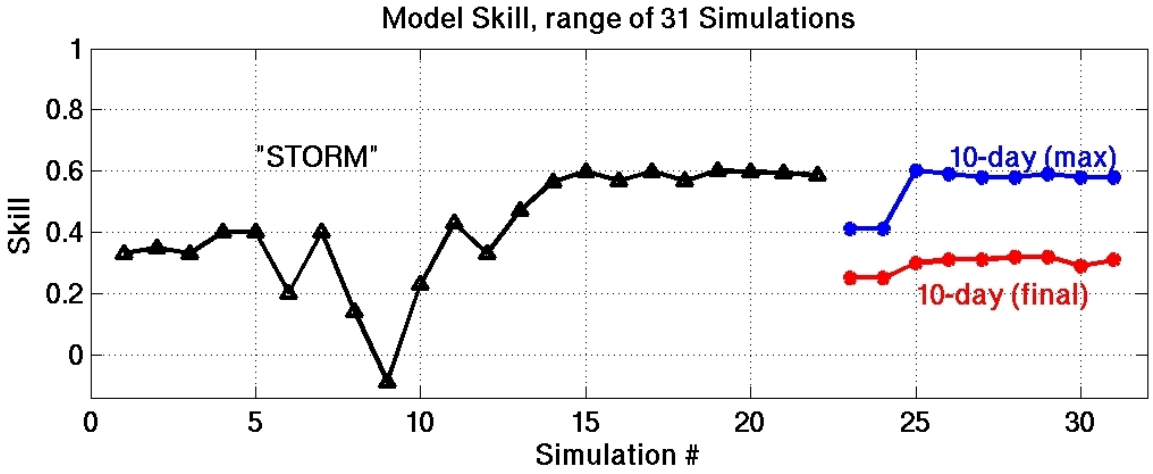

Figure 22. XBeach model skill values for 31 simulations in quantitative 2D skill test. The first 22 simulations are for 3.5 "storm" days, with significant wave height and peak period equal to storm values ±20%. Skill values are lower for the storm cases with artificially low peak period and small wave height (e.g., simulation #9 had H_s=0.8*$H_{s,storm}$ and T_p=0.8*$T_{p,storm}$). The highest skill values (approximately 0.6) are attained for waves with H_s=$H_{s,storm}$ and T_p=$T_{p,storm}$, using a higher Shields limiter (θ_{sf} =1.2). The last nine simulations are run for 10 days using daily- or two-day-averaged wave height and period for each day (Fig. 21). The "max" curve (blue) includes maximum skill achieved by each test (generally after 4–5 days), while the "final" curve shows skill value after full 10-day simulations.

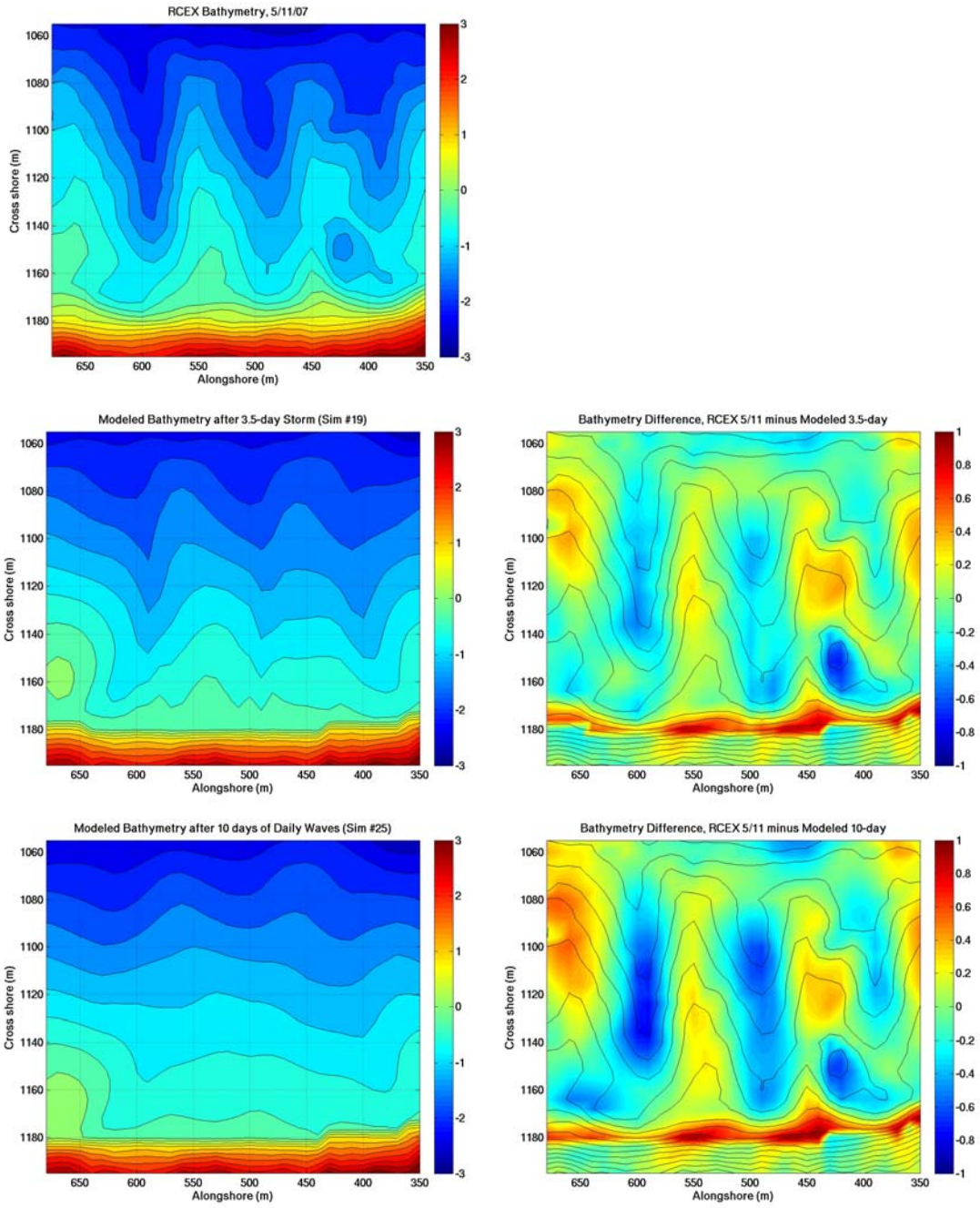

Figure 23. Comparison of measured and XBeach-predicted bathymetries at Sand City, May 11, 2007. Top left image is measured bathymetry. Final bathymetries from 3.5-day XBeach "storm" simulation #19 (middle left) and 10-day simulation #25 (bottom left) are both smoothed relative to actual bathymetry. In plots of measured-minus-modeled bathymetry differences over measured May 11 bathymetry contours (right panels), the largest model errors result from over-erosion of the shoreline.

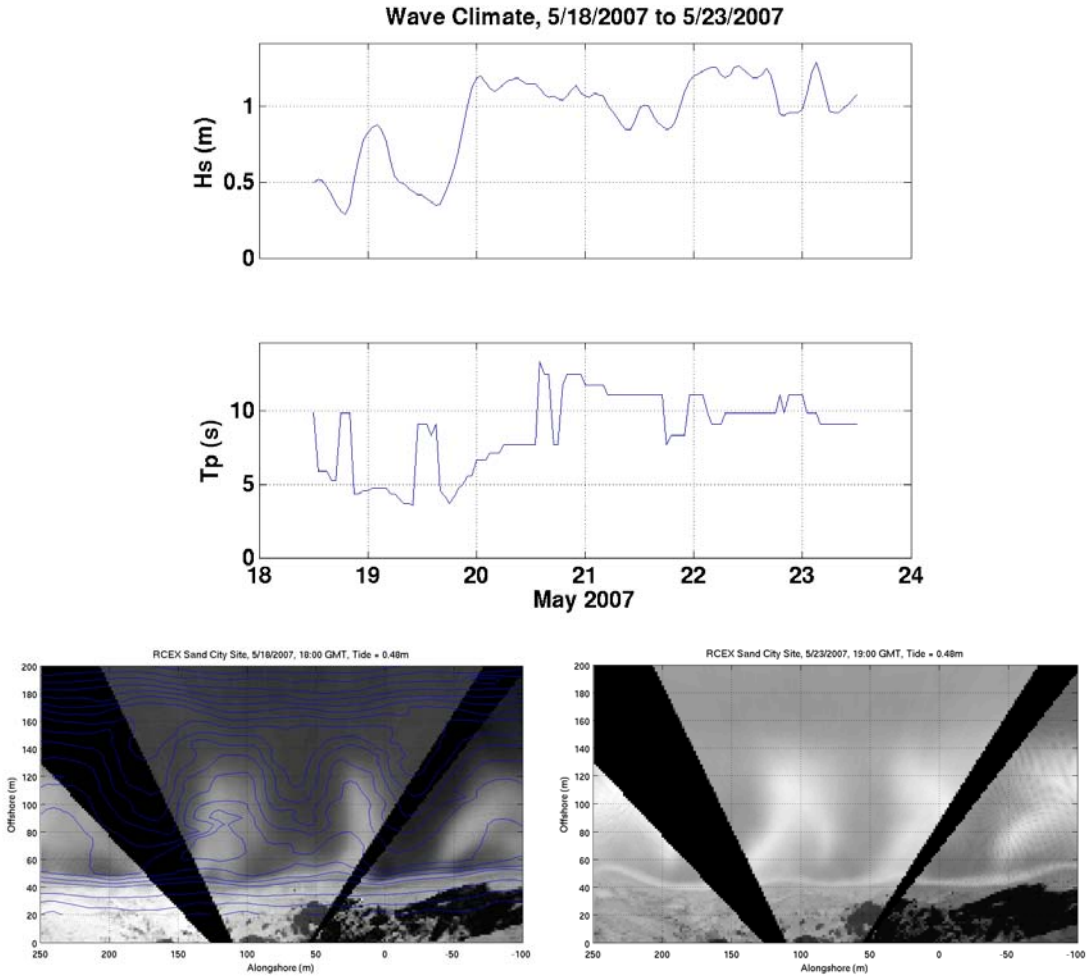

Figure 24. Wave conditions recorded during the 2007 RCEX experiment from May 18–23 (top two panels), including a three-day period of consistently moderate waves with significant wave heights around 1 m. Bottom two panels show video images from initial and final days of this period, overlaid with measured bathymetry contours when available. Both images were recorded at tide = MSL + 0.48 m. These data are used in the second, qualitative 2D test of the XBeach model.

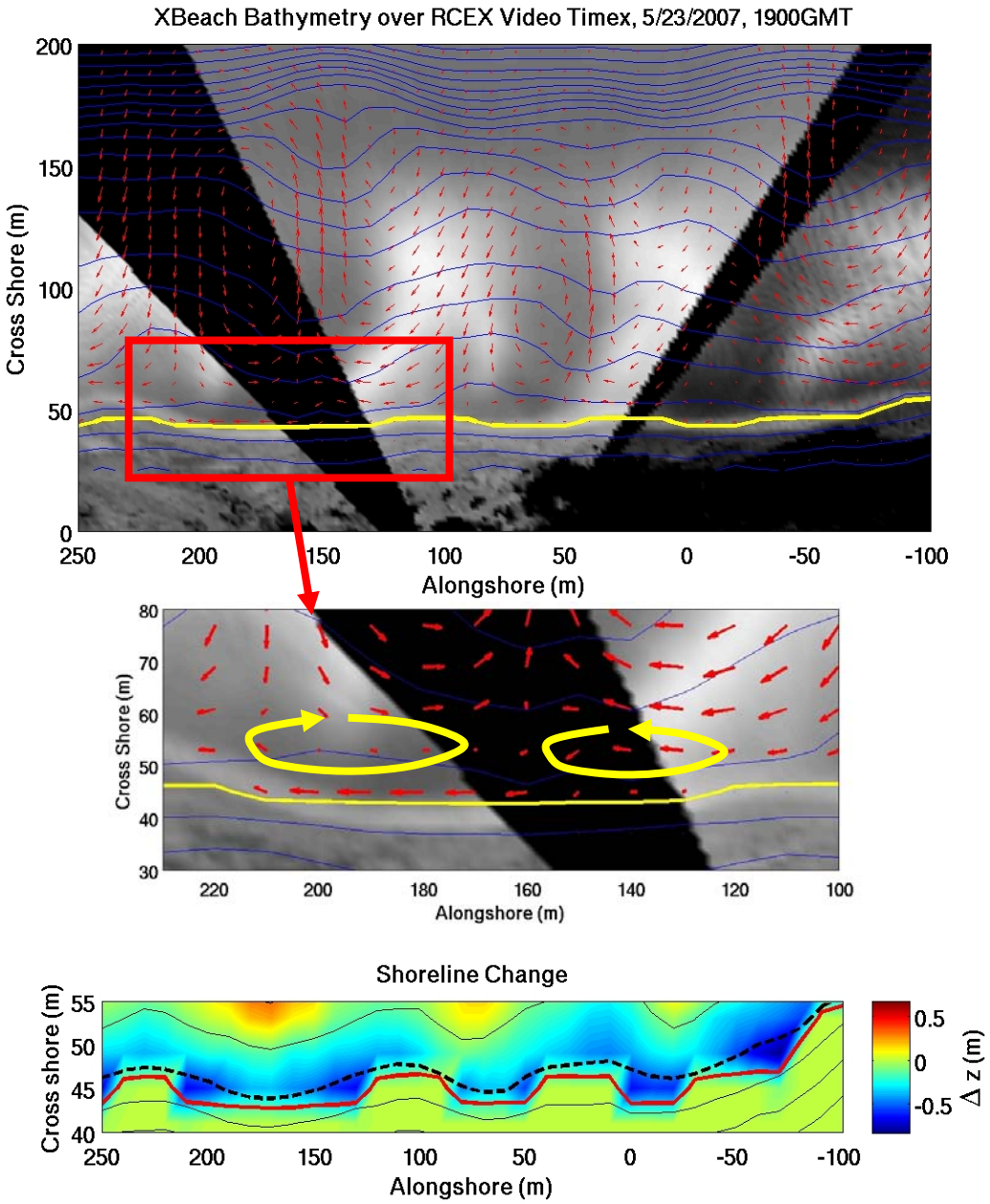

Figure 25. *Top*: Video image of surf zone at Sand City, CA, on May 23, 2007, overlaid with XBeach-predicted bathymetry contours (blue) and flow field vectors (red arrows). Model initialized with measured bathymetry from May 18, 2007, and average "storm" waves (H_s = 1.1 m, T_p = 10 s) for a 72-hr period. Yellow line shows XBeach-predicted shoreline, which qualitatively captures the video-detected shoreline shape, including three RO megacusps (centered at ~ 0 m, 75 m, and 175 m). *Middle*: Zoomed view of leftmost megacusp (lower panel) shows that XBeach also predicts swash zone counter-currents in the embayment. *Bottom*: Model-predicted elevation change (color), overlaid with bathymetry contours. Megacusp embayments on May 23 shoreline (red line) have been widened relative to original May 18 perturbations (black dashed line).

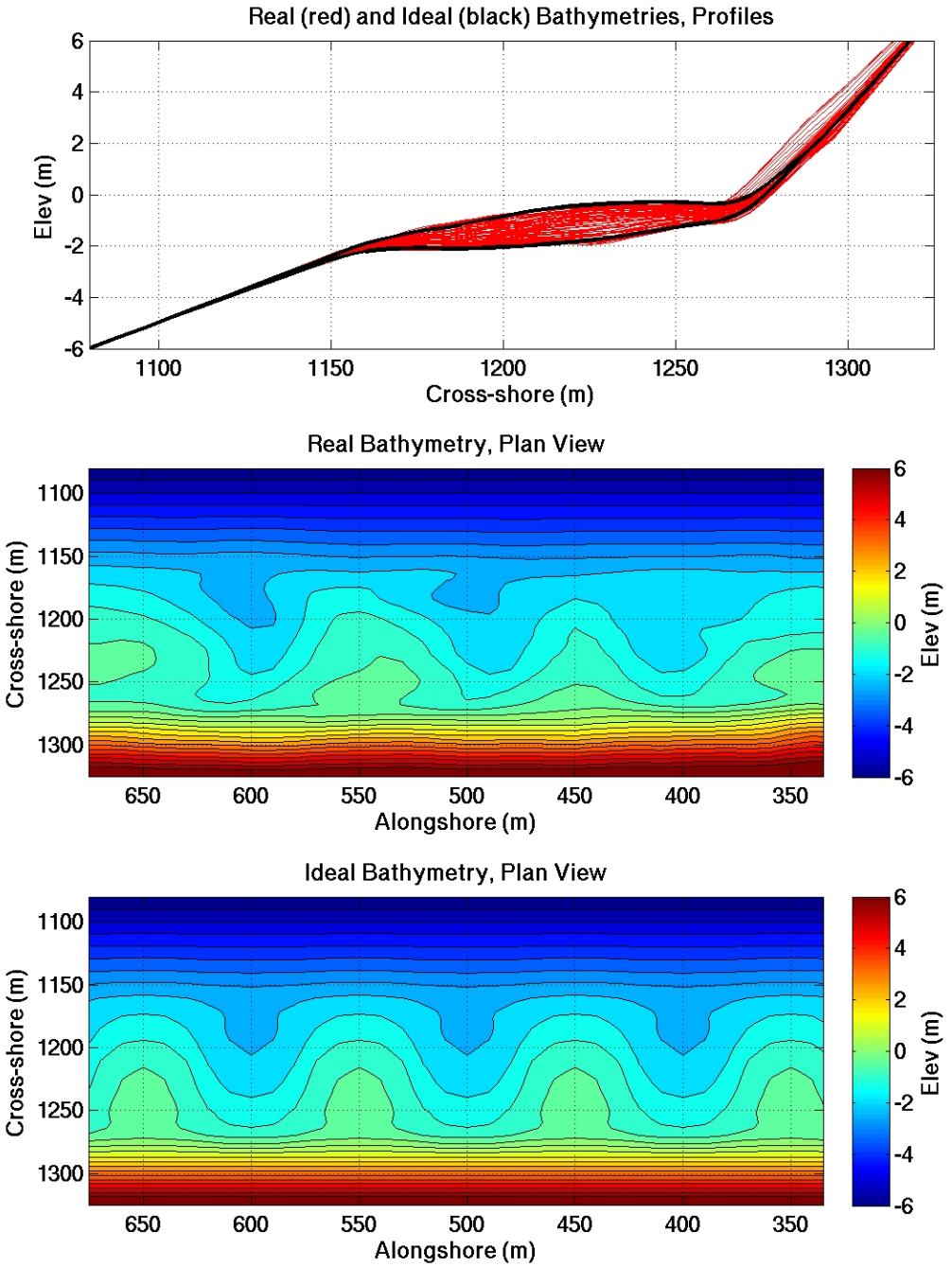

Figure 26. Bathymetry profiles and plan views for the two idealized megacusp formation scenarios, based on measured data from May 1, 2007. Top panel shows range of profiles from three-point-smoothed RCEX "real" bathymetry (red lines) overlaid with max/min profiles from "ideal" bathymetry (black lines). Each bathymetry extends offshore to 30 m with a 1:50 slope and on the beach up to 10 m with a 1:10 slope. Middle and bottom panels show "real" and "ideal" bathymetry contours, respectively, for central, nearshore section of model grid.

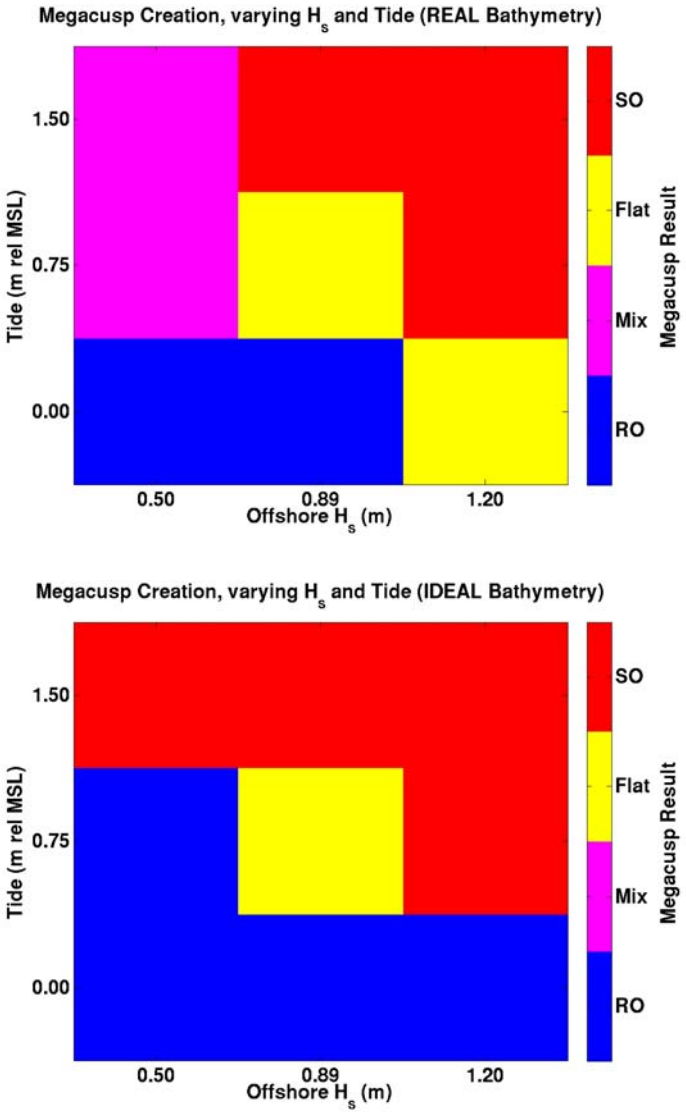

Figure 27. Summarized results of 18 XBeach simulations to build megacusps on a beach shoreward of realistic (top) and idealized (bottom) bathymetry. Offshore significant wave height values are 0.5, 0.89, and 1.2 m (x-axis), and fixed mean water levels are MSL + 0.0, 0.75, and 1.5 m (y-axis). Blue squares denote the formation of rip-opposite (RO) megacusps and red squares indicate shoal-opposite (SO) megacusps, while magenta represents a mix of RO and SO, and yellow is used where bathymetry flattened out with no resultant megacusps. Lower mean water levels and smaller waves tend to generate RO megacusps, while higher mean water levels and bigger waves lead to SO megacusps.

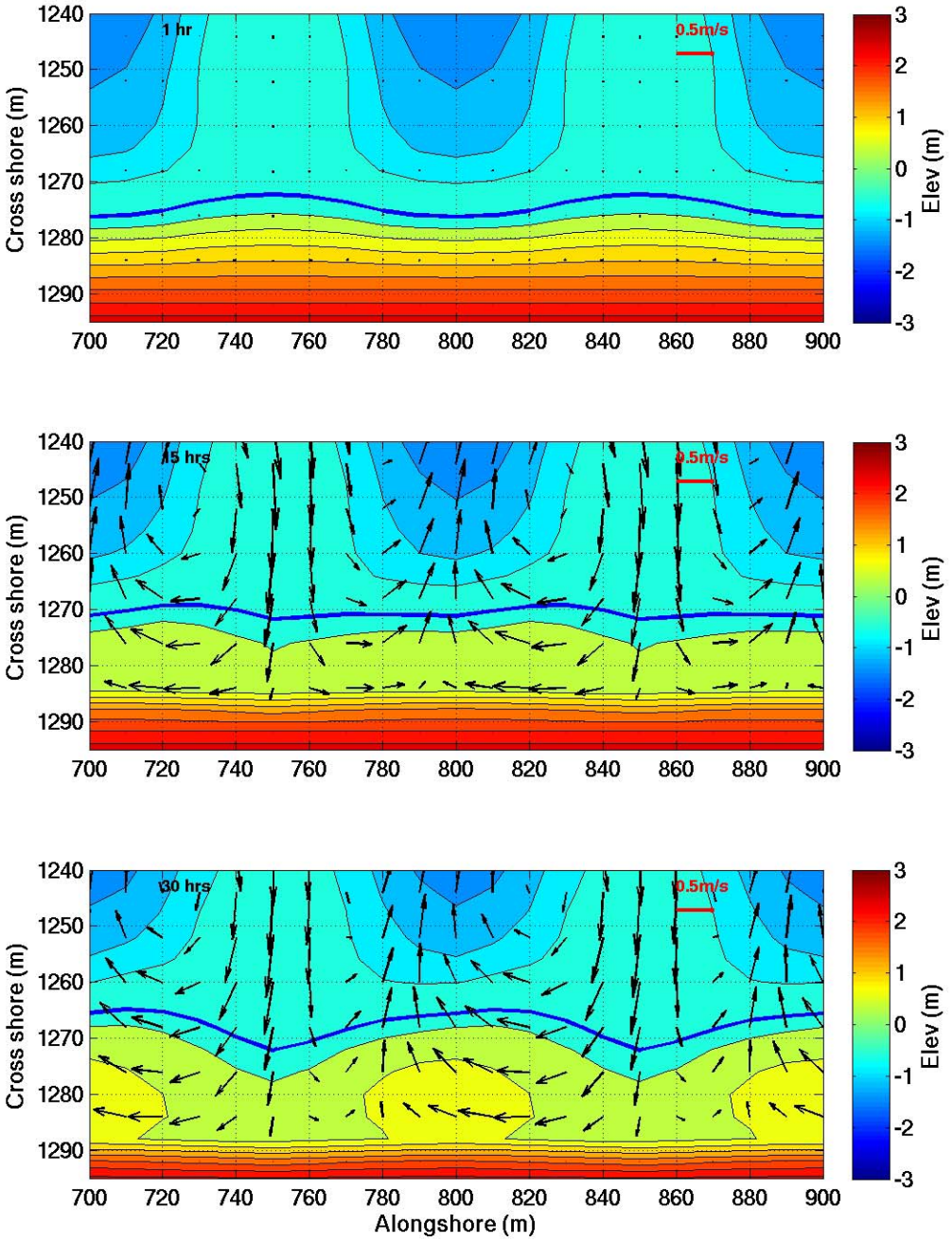

Figure 28. SO megacusp formation on idealized rip channel bathymetry. Images show bathymetry contours and mean flow field vectors (arrows) at 1, 15, and 30 hours, under shore-normal JONSWAP waves with H_s = 1.2 m, T_p = 11 s, and water level = MSL + 1.5 m. Blue line is used for MSL contour.

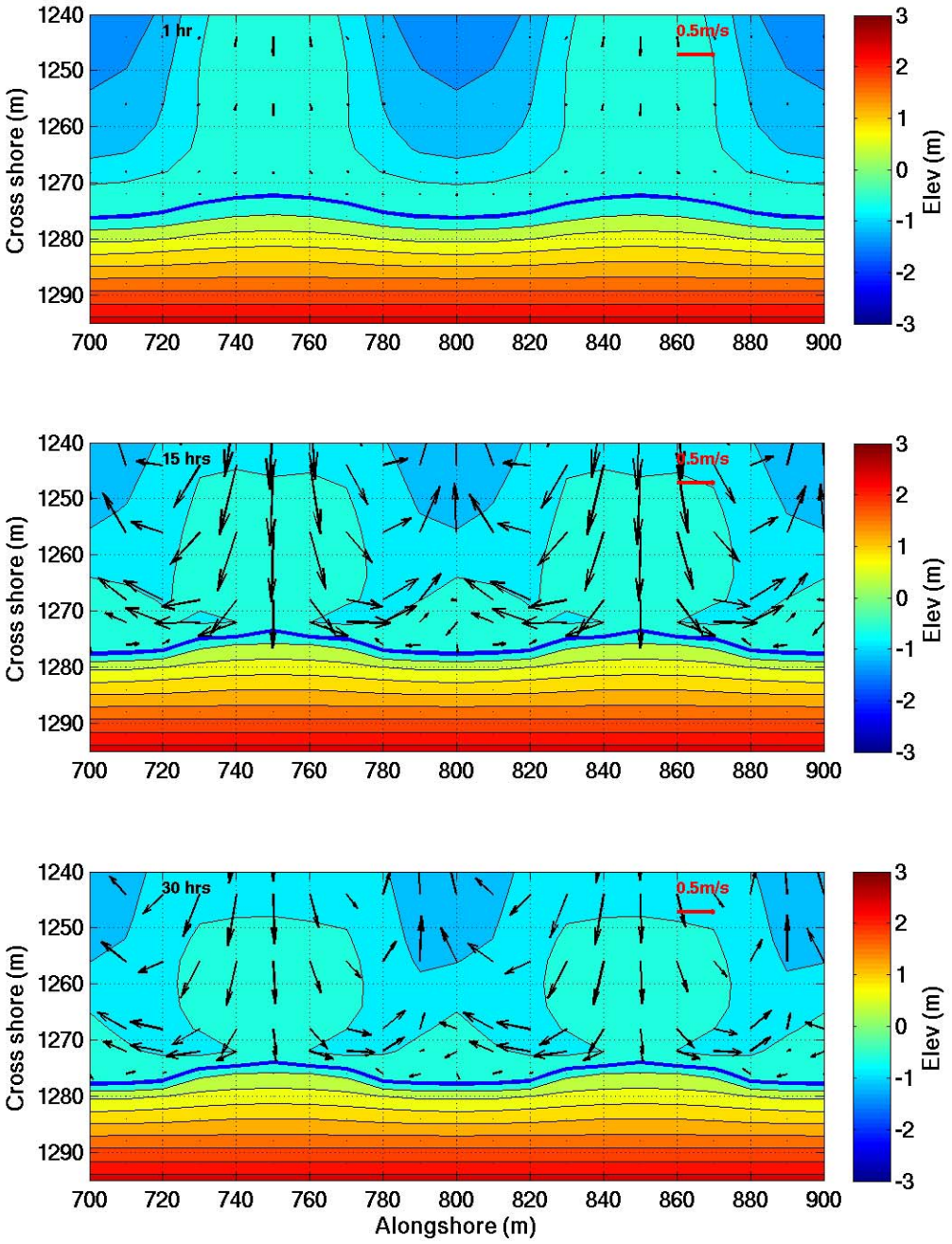

Figure 29. RO megacusp growth/steepening from existing perturbations on idealized rip channel bathymetry. Images show bathymetry contours and mean flow field vectors (arrows) at 1, 15 and 30 hours, under shore-normal JONSWAP waves with H_s = 1.2 m, T_p = 11 s, and water level = MSL. Blue line is used for MSL contour and includes narrow perturbations at startup (top panel). Weak but persistent counter-circulation vortices are present in megacusp embayments (middle and bottom panels).

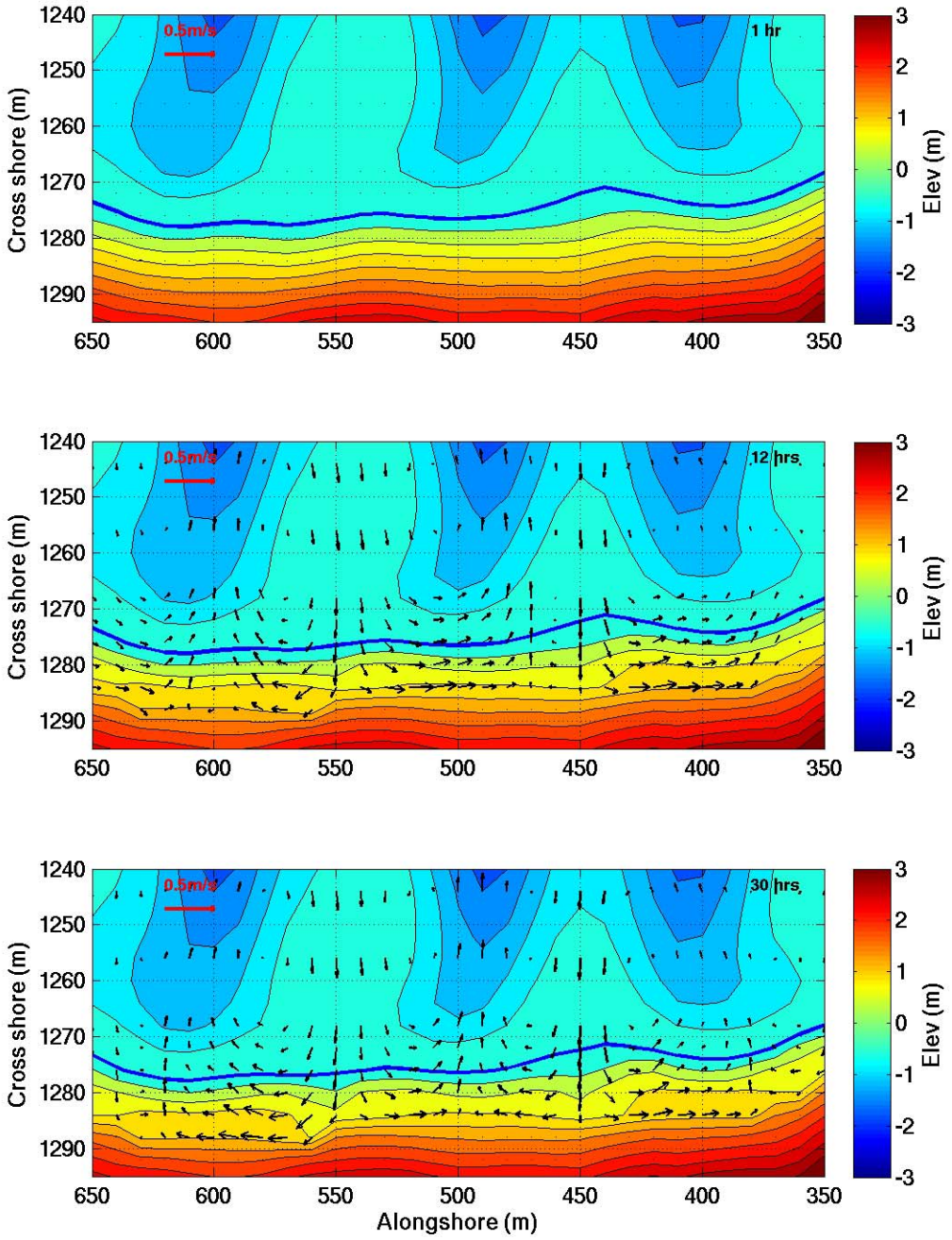

Figure 30. Megacusp growth on "real" (three-point smoothed) rip channel bathymetry from RCEX experiment. For this simulation, H_s = 0.5 m, T_p = 7 s, and water level is fixed at MSL + 1.5 m. By t = 12 hrs (middle panel), the mean flow field (arrows) has generated RO megacusp at the +1 m contour, centered near y = 600 m. At t = 30 hrs (bottom panel), multiple SO megacusps have begun to grow at MSL + 0.3 m and MSL + 0.6 m contours (MSL is thick blue contour).

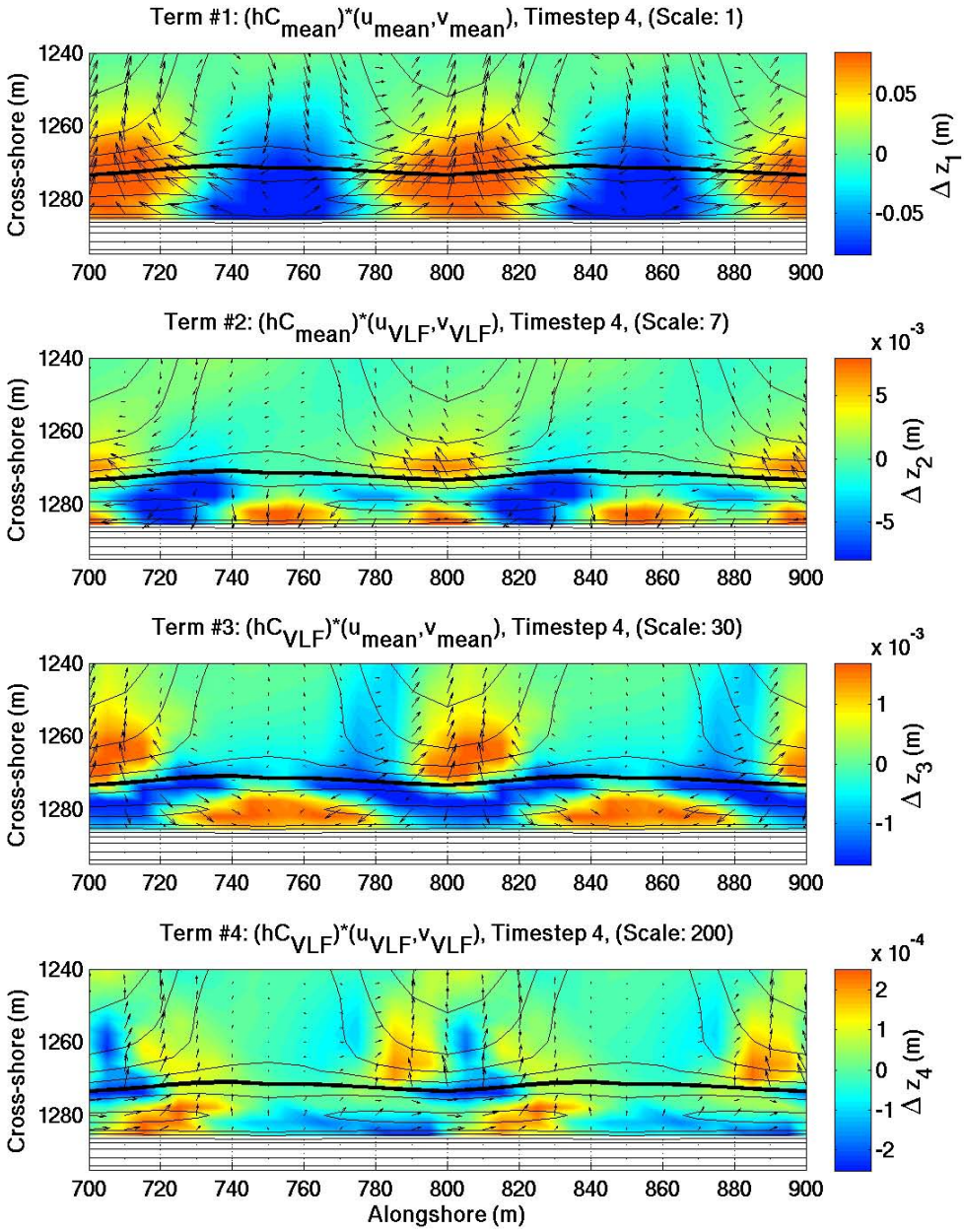

Figure 31. SO megacusp formation (early stage, t = 8 hrs). Largest four paired components of Eq. 19 and 20 plotted as vector flow fields over mean or VLF component of bathymetry change Δz (color shading), with concurrent bathymetry contours (black lines; MSL thicker). Bathymetry changes Δz_i are estimated from negative gradient of each component (white regions are unchanged beach elevations). Vector length on each plot is adjusted by specified "Scale" multiplier for viewability. *Top panel*: $\overline{hC}\overline{u}\cdot\vec{i}+\overline{hC}\overline{v}\cdot\vec{j}$. *Second panel*: $\overline{hC}\hat{u}\cdot\vec{i}+\overline{hC}\hat{v}\cdot\vec{j}$. *Third panel*: $\widehat{hC}\overline{u}\cdot\vec{i}+\widehat{hC}\overline{v}\cdot\vec{j}$. *Bottom panel*: $\widehat{hC}\hat{u}\cdot\vec{i}+\widehat{hC}\hat{v}\cdot\vec{j}$. (Note: $u\cdot\vec{i}$ is cross-shore direction and $v\cdot\vec{j}$ is alongshore.)

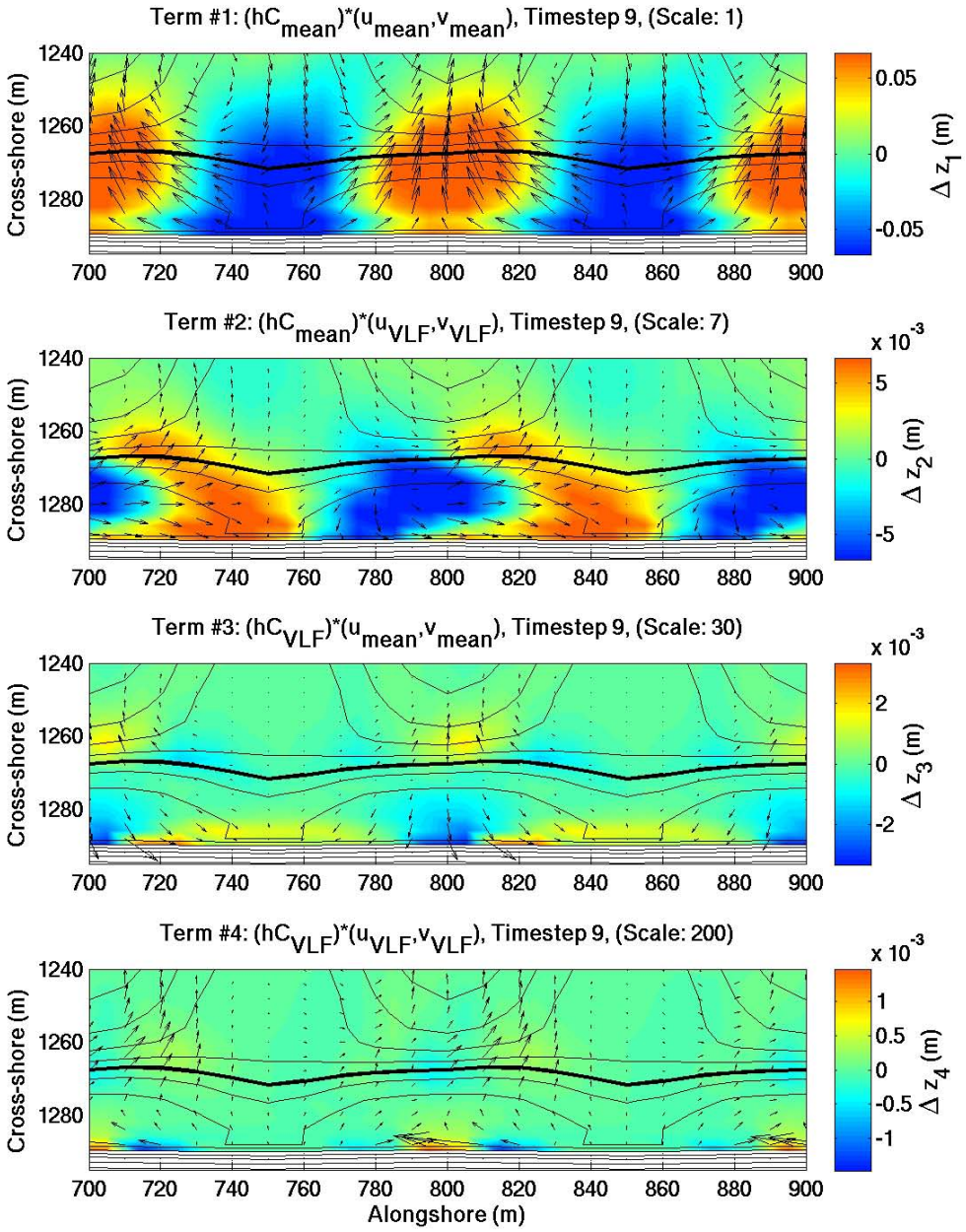

Figure 32. SO megacusp formation (late stage, t = 18 hrs). Largest four paired components of Eq. 19 and 20 plotted as vector flow fields as in Fig. 31. *Top panel*: $\overline{hC}\overline{u}\cdot\vec{i}+\overline{hC}\overline{v}\cdot\vec{j}$. *Second panel*: $\overline{hC}\hat{u}\cdot\vec{i}+\overline{hC}\hat{v}\cdot\vec{j}$. *Third panel*: $\widehat{hC}\overline{u}\cdot\vec{i}+\widehat{hC}\overline{v}\cdot\vec{j}$. *Bottom panel*: $\widehat{hC}\hat{u}\cdot\vec{i}+\widehat{hC}\hat{v}\cdot\vec{j}$.

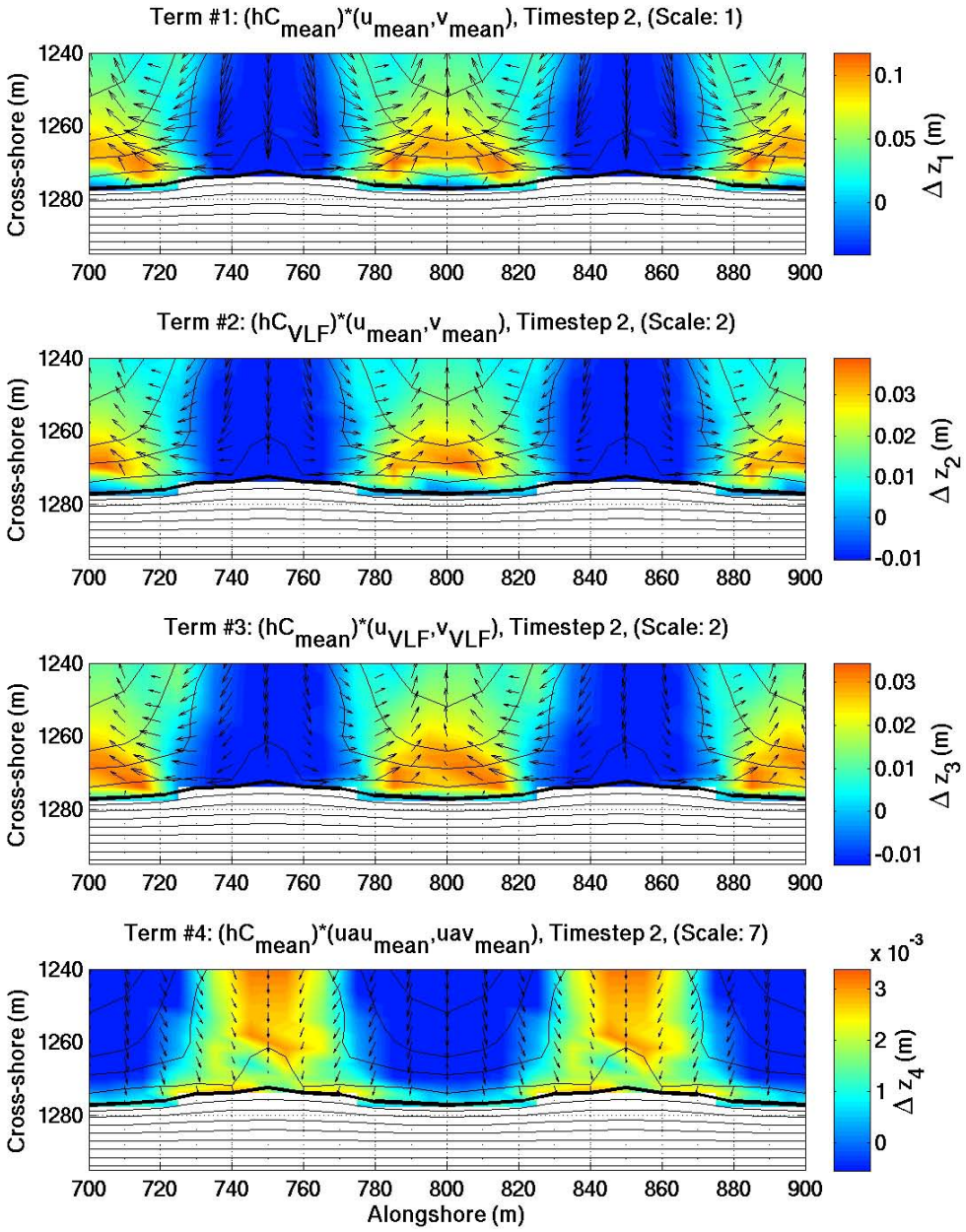

Figure 33. RO megacusp formation (early stage, t = 4 hrs). Largest four paired components of Eq. 19 and 20 plotted as vector flow fields as in Fig. 31. *Top panel*: $\overline{hC\overline{u}} \cdot \vec{i} + \overline{hC\overline{v}} \cdot \vec{j}$. *Second panel*: $\widehat{hC\overline{u}} \cdot \vec{i} + \widehat{hC\overline{v}} \cdot \vec{j}$. *Third panel*: $\overline{hC\hat{u}} \cdot \vec{i} + \overline{hC\hat{v}} \cdot \vec{j}$. *Bottom panel*: $\overline{hC\overline{u}}_{asym} \cdot \vec{i} + \overline{hC\overline{v}}_{asym} \cdot \vec{j}$. Here, minimum color scale value has been increased slightly to better emphasize erosive regions ($\Delta z_i < 0$) in cusp embayments.

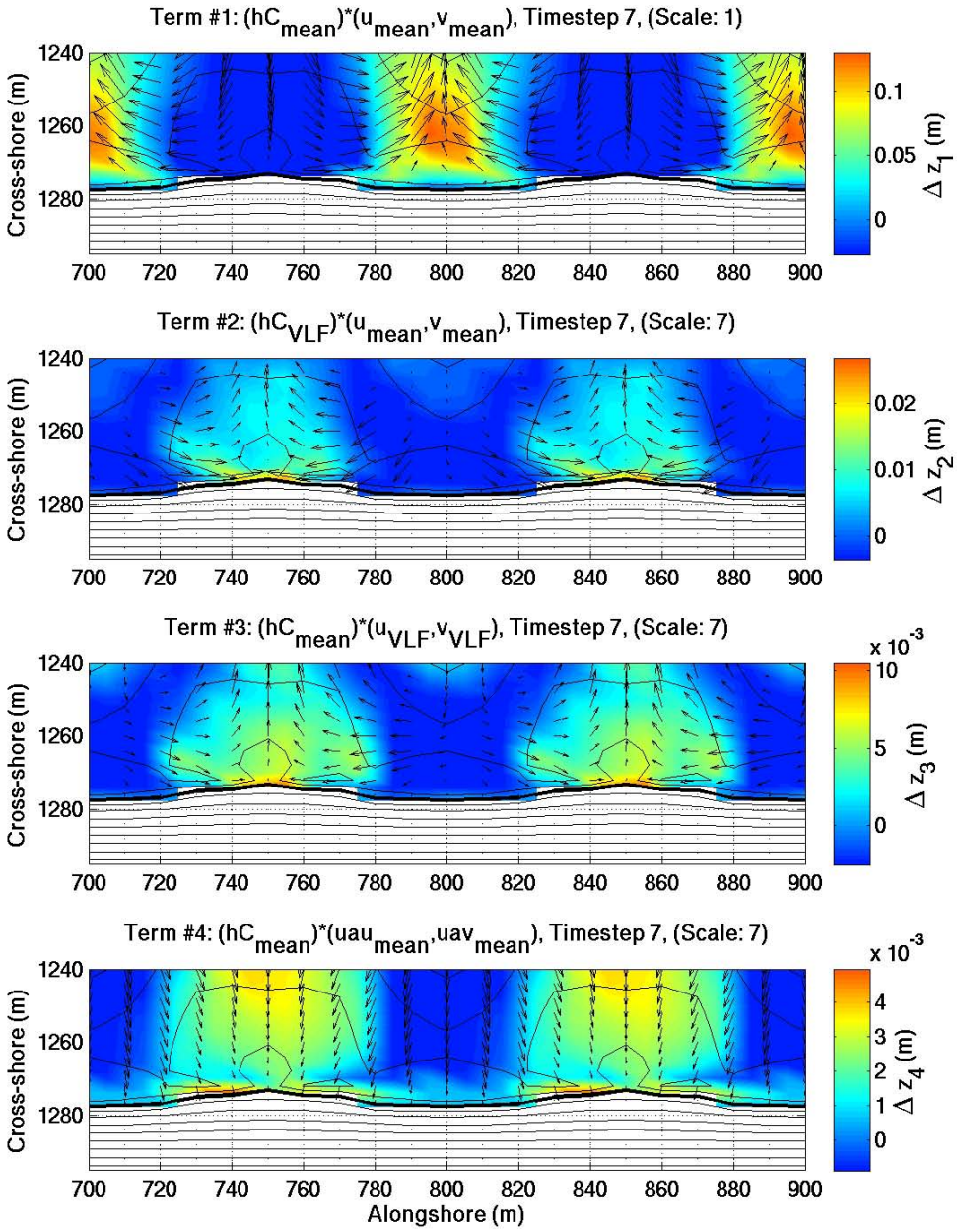

Figure 34. RO megacusp formation (later stage, t = 14 hrs). Largest four paired components of Eq. 19 and 20 plotted as vector flow fields as in Fig. 33. *Top panel*: $\overline{hC\vec{u}} \cdot \vec{i} + \overline{hC\vec{v}} \cdot \vec{j}$. *Second panel*: $\widehat{hC\vec{u}} \cdot \vec{i} + \widehat{hC\vec{v}} \cdot \vec{j}$. *Third panel*: $\overline{hC\hat{u}} \cdot \vec{i} + \overline{hC\hat{v}} \cdot \vec{j}$. *Bottom panel*: $\overline{hC\vec{u}}_{asym} \cdot \vec{i} + \overline{hC\vec{v}}_{asym} \cdot \vec{j}$.

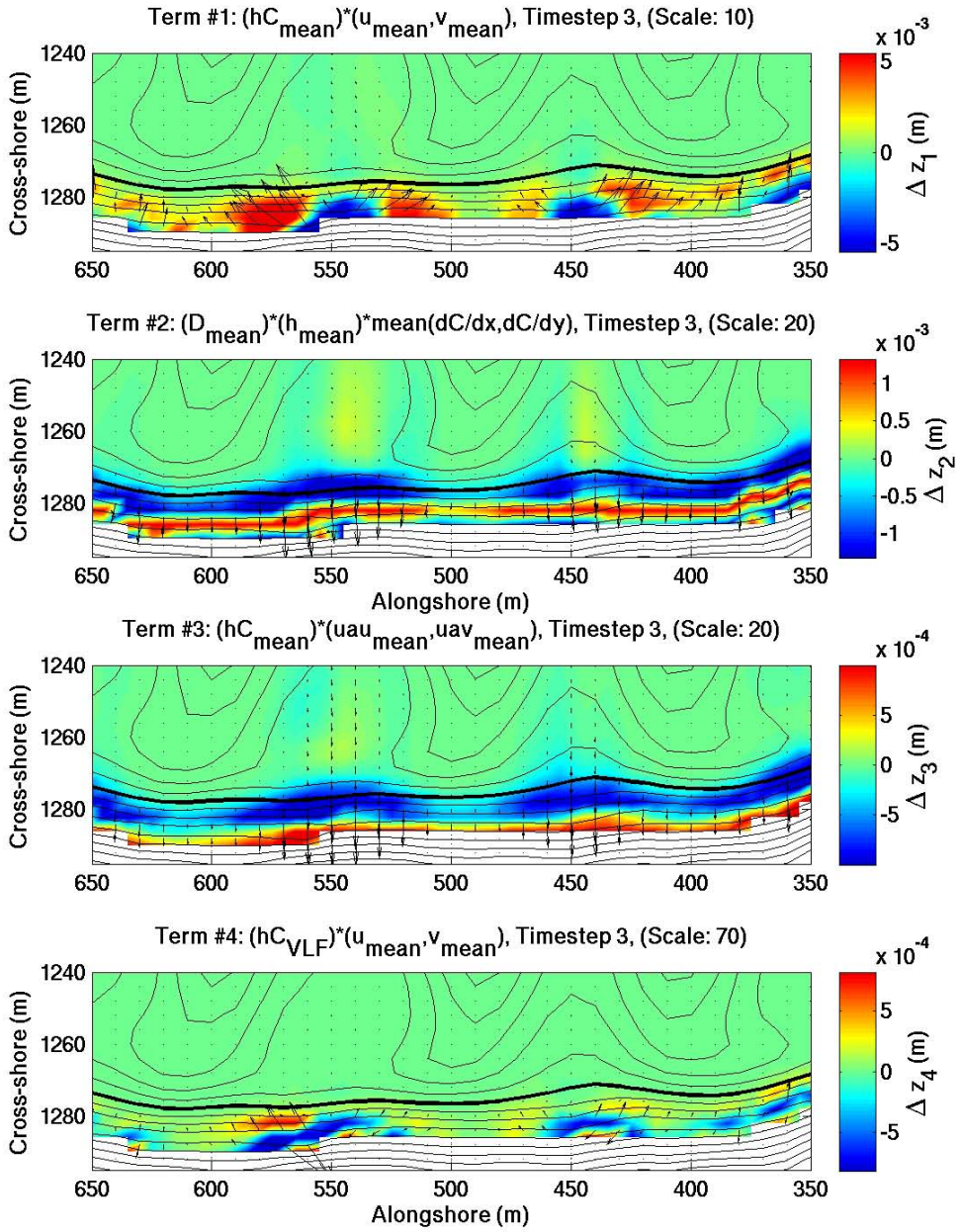

Figure 35. Megacusp formation on real bathymetry with small waves, H_{m0} = 0.5 m (early stage, t = 6 hrs). Largest four paired components of Eq. 19 and 20 plotted as vector flow fields as in Fig. 31. <u>*Top panel*</u>: $\overline{hC}\overline{u}\cdot\vec{i}+\overline{hC}\overline{v}\cdot\vec{j}$. <u>*Second panel*</u>: $\overline{D}\overline{h}\left[\frac{\overline{\partial C}}{\partial x}\vec{i}+\frac{\overline{\partial C}}{\partial y}\vec{j}\right]$. <u>*Third panel*</u>: $\overline{hC}\overline{u}_{asym}\cdot\vec{i}+\overline{hC}\overline{v}_{asym}\cdot\vec{j}$. <u>*Bottom panel*</u>: $\widehat{hC}\overline{u}\cdot\vec{i}+\widehat{hC}\overline{v}\cdot\vec{j}$.

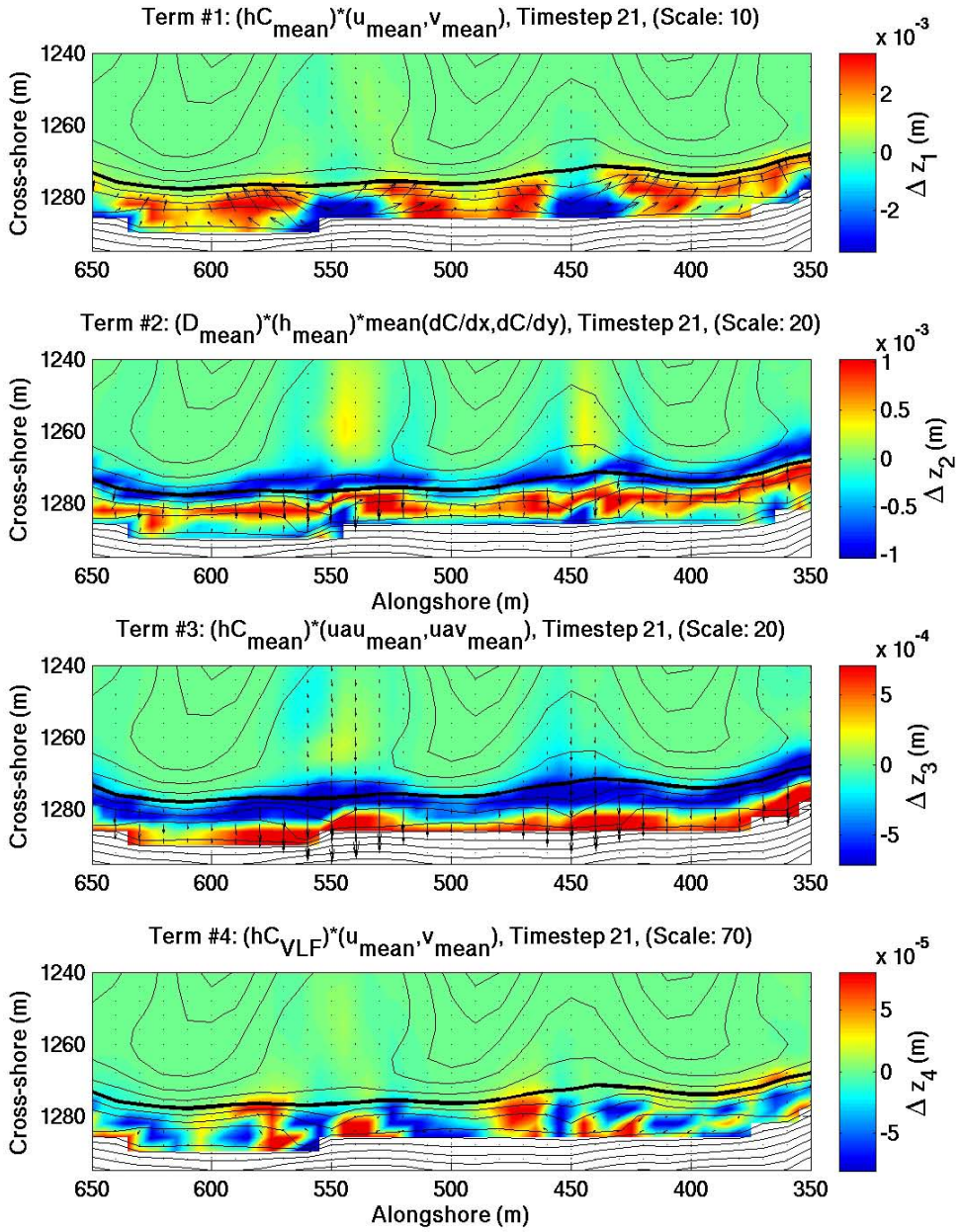

Figure 36. Megacusp formation on real bathymetry with small waves, H_{m0} = 0.5 m (late stage, t = 42 hrs). Largest four paired components of Eq. 19 and 20 plotted as vector flow fields as in Fig. 22. <u>*Top panel*</u>: $\overline{hC}\overline{u}\cdot\vec{i}+\overline{hC}\overline{v}\cdot\vec{j}$. <u>*Second panel*</u>: $\overline{D}\overline{h}\left[\frac{\overline{\partial C}}{\partial x}\vec{i}+\frac{\overline{\partial C}}{\partial y}\vec{j}\right]$. <u>*Third panel*</u>: $\overline{hC}\overline{u}_{asym}\cdot\vec{i}+\overline{hC}\overline{v}_{asym}\cdot\vec{j}$. <u>*Bottom panel*</u>: $\widehat{hC}\overline{u}\cdot\vec{i}+\widehat{hC}\overline{v}\cdot\vec{j}$.

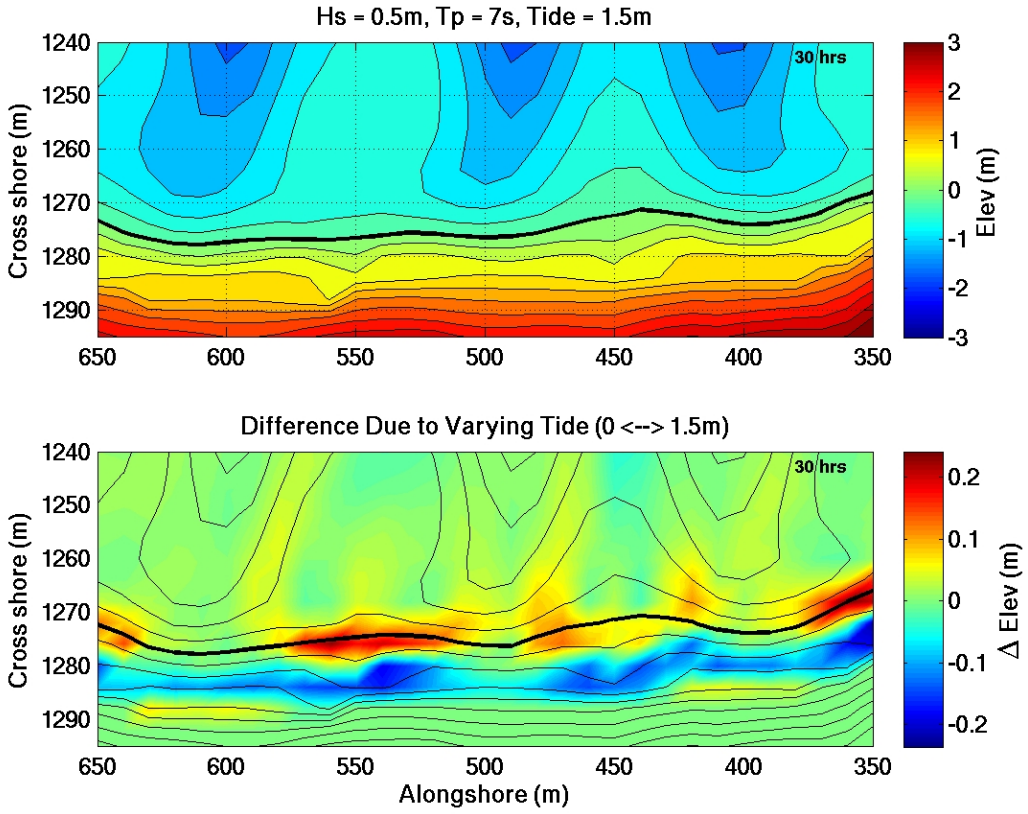

Figure 37. Comparison of "real" bathymetry elevations following 30 hours of evolution under small waves (H_s = 0.5m, T_p = 7 s). *Top panel*: Bed elevations resulting from fixed tide level of MSL + 1.5 m. *Bottom panel*: Differences from original elevations (color) when tide level is instead varied between 0 and 1.5 m in a 12-hour cycle. Relative to the fixed tide case, the SO megacusp contours under the varying tide are spread out in the cross-shore, but otherwise in the same location. The contours of the RO megacusp (centered at y = 600 m) are also slightly steeper with the fixed tide than with the variable tide.

Table 1. Comparison of rip location statistics. Summary of subjective differences in rip locations, which were selected on 110 daily rectified video images from Jan–Apr 2005 by four investigators. MO is M. Orzech and ET is E. Thornton, while alternates 1 and 2 are graduate students somewhat less experienced with the problem. Statistics calculated are the same as those in Holman et al. (2006). In the first three data columns, space and time averages (subscripts *y* and *t*) are presented for the location differences dy_i, their standard deviation, and their RMS value. The final two columns show the time-averaged number of rip locations matched and missed between each pair of investigators.

Digitizer	$\left\langle \left\langle dy_i \right\rangle_y \right\rangle_t$	$\left\langle \left\langle std(dy_i) \right\rangle_y \right\rangle_t$	$\left\langle \left\langle rms(dy_i) \right\rangle_y \right\rangle_t$	$\left\langle N_{match} \right\rangle_t$	$\left\langle N_{miss} \right\rangle_t$
MO-ET	0.3	11.5	11.5	6.1	2.1
MO-alt 1	1.8	10.4	10.6	5.3	2.3
MO-alt 2	-0.8	12.3	12.3	5.9	2.4

Table 2. Summary of measured rip migration and modeled sediment transport rates and filtered correlations. Column 1 lists RMS rip migration rate data at each site, determined by the methods described in Section IIC. Column 2 shows absolute sediment transport rate statistics as predicted by the CERC formulation. Remaining columns contain correlation coefficients (excluding resets) for original daily rip migration and alongshore transport rates (Column 3), using eight-day-average rates (Column 4), using daily rates from only the highest 10% of transport days (Column 5), using daily rates to which a fourth-order low-pass filter with cutoff of 1/8 days^{-1} has been applied (Column 6), and using cumulatively summed mean migration distance and net sediment transport (Column 7).

	RMS Rip Migration (m/day)	**Sediment Transport Magnitude (m^3/day)**	**Migration-Transport Correlation**				
			Daily	**Filtered**			
				Eight-day	*Low-Pass*	*High 10%*	*Cumulative Sums*
	1	**2**	**3**	**4**	**5**	**6**	**7**
SAND CTY							
Max	18	500					
Mean	5.8	68	0.01	0.06	0.07	0.23	0.94
Mode	4.5	26					
STILWELL							
Max	22	4500					
Mean	6.7	206	0.44	0.60	0.66	0.66	0.76
Mode	4.5	2					
MARINA							
Max	30	22700					
Mean	9.0	462	0.38	0.58	0.60	0.54	0.87
Mode	7.5	175					

Table 3. Summary of Equilibrium Profile Test Results

XBeach Model Parameters	***Values Tested***	***Optimal Value***
θ_{sf} *(smax)*	0.8, 1.0, 1.2	0.8
$T_{s,factor}$ *(tsfac)*	0.05, 0.10, 0.15	0.10
$u_{a,fac}$ *(facua)*	0.1, 0.5, 1.0	0.5
f_{mor} *(morfac)*	1, 5, 10	1
h_{min} *(hmin)*	0.001, 0.01, 0.1 m	0.01 m
γ (*gamma)*	0.45, 0.60, 0.75	0.45

Table 4. Fixed Settings for Other XBeach Model Parameters*

Parameter	Value	Parameter	Value
instat	4	rho	1025 kg/m^3
break	3	g	9.81 m/s^2
alpha	1.0	thetamin	-80º
wci	0	thetamax	+80º
beta	0.05	nuh (ν_b)	0.1
delta	0	nuhfac (β_ν)	1.0
form	1-2	rhos	2650 kg/m^3
eps	0.1 m	tideloc	1
umin	0.1 m/s	tidelen	varied
dtheta	10º	tint	varied
morstart	varied	left	0–1
zs0	varied	right	0–1
C (Chezy)	40 m$^{0.5}$/s	D50	0.0004 m
vardx	1	D90	0.0006 m
dx, dy	varied	nx, ny	varied
s (cos pwr)	8	gammajsp	3.3
fnyq	0.3 Hz		

** All parameters not included here or in Table 3 are set to their default values.*

Table 5. Dominant Sediment Transport Components for Megacusp Formation

Rank (t = 4 hrs)	"Ideal" Bathymetry				"Real" Bathymetry	
	RO Megacusps[a]		SO Megacusps[b]		RO/SO Megacusps[c]	
	Term	Rel. Size	Term	Rel. Size	Term	Rel. Size
1	$\overline{hC}\overline{v}$	100	$\overline{hC}\overline{v}$	100	$\overline{hC}\overline{u}$	100
2	$\overline{hC}\overline{u}$	42	$\overline{hC}\overline{u}$	90	$\overline{hC}\overline{v}$	78
3	$\overline{hC}\hat{v}$	37	$\overline{hC}\hat{v}$	30	$\overline{hC}\overline{u}_{asym}$	37
4	$\widehat{hC}\overline{v}$	27	$\overline{hC}\hat{u}$	19	$\overline{D}\overline{h}\dfrac{\overline{\partial C}}{\partial x}$	31
5	$\overline{hC}\hat{u}$	15	$\overline{hC}\overline{u}_{asym}$	17	$\overline{D}\overline{h}\dfrac{\overline{\partial C}}{\partial y}$	7
6	$\widehat{hC}\overline{u}$	13	$\widehat{hC}\overline{v}$	12	$\widehat{hC}\overline{u}$	6
7	$\widehat{hC}\hat{v}$	12	$\overline{D}\overline{h}\dfrac{\overline{\partial C}}{\partial x}$	11	$\overline{hC}\hat{v}$	6
8	$\widehat{hC}\hat{u}$	5	$\widehat{hC}\overline{u}$	9	$\overline{D}\overline{h}\dfrac{\widehat{\partial C}}{\partial x}$	5
9	$\overline{D}\overline{h}\dfrac{\overline{\partial C}}{\partial x}$	4	$\overline{D}\overline{h}\dfrac{\widehat{\partial C}}{\partial x}$	6	$\widehat{hC}\overline{v}$	5
10	$\overline{hC}\overline{u}_{asym}$	3	$\widehat{hC}\hat{v}$	4	$\overline{hC}\hat{u}$	3

Simulation Wave and Tide Settings:

a. H_{m0} = 1.2 m, T_p = 11 s, tide = MSL

b. H_{m0} = 1.2 m, T_p = 11 s, tide = MSL + 1.5 m

c. H_{m0} = 0.5 m, T_p = 7 s, tide = MSL + 1.5 m

Table 6. Recent Skill Tests with XBeach or Delft3D

Source	Model	Location	Parameter	Skill range
Reniers et al., 2006	Delft3D	Sand City, CA	H_s	0.83 – 0.85
Brown, 2009	XBeach	Sand City, CA	H_{rms}	0.84 – 0.93
Brown, 2009	XBeach	Sand City, CA	u^E, v^E	0.47 – 0.72
Brown, 2009	XBeach	Sand City, CA	u^L, v^L	~ 0.5
McCall et al., 2010	XBeach	Santa Rosa Island, FL	z_{bed}	-2.69 – 0.77

LIST OF REFERENCES

Aagaard, T., Greenwood, B., & Nielsen, J. (1997). Mean currents and sediment transport in a rip channel. *Marine Geology,* 140, 24–45.

Andrews, D.G. & McIntyre, M.E. (1978). An exact theory of nonlinear waves on a Lagrangian-mean flow. *Journal of Fluid Mechanics*, 89(4), 609–646.

Battjes, J.A. (1975). Modeling of turbulence in the surf zone. In *Proceedings of Symposium on Modeling Technology* (1050–1061). New York, NY: ASCE.

Battjes, J.A., & Janssen, J.P.F.M. (1978). Energy loss and set-up due to breaking of random waves. In *Proceedings of 16th International Conference on Coastal Engineering, Vol 1* (569–587). New York, NY: ASCE.

Blondeaux, P. (2001). Mechanics of coastal forms. *Annual Review of Fluid Mechanics,* 33, 339–370.

Bogle, J.A., Bryan, K.R., Black, K.P., Hume, T.M., & Healy, T.R. (2001). Video observations of rip formation and evolution. *Journal of Coastal Research,* Special Issue 34, 117–127.

Bowen, A.J. (1969). Rip currents, 1, Theoretical investigations. *Journal of Geophysical Research*, 74(23), 5467–5478.

Brander, R.W., & Short, A.D. (2001). Flow kinematics of low-energy rip current systems. *Journal of Coastal Research* 17(2), 468–481.

Brown, J. (2008). *Field Measurements and Modeling of Surfzone Currents on Inhomogeneous Beaches*. Master's Thesis, University of Delaware.

Brown, J., MacMahan, J., Reniers, A., & Thornton, E. (2009). Surf zone diffusivity on a rip-channeled beach. *Journal of Geophysical Research,* 114, C11015, DOI: 10.1029/2008JC005158.

Calvete, D., Dodd, N., Falques, A., & van Leeuwen, S.M. (2005). Morphological development of rip channel systems: normal and near-normal wave incidence. *Journal of Geophysical Research,* 110(C10), C10006, DOI 10.1029/2004JC002803.

Coastal Data Information Program (2010). *CDIP Homepage*. Retrieved March 1, 2010, from Coastal Data Information Program, University of California at San Diego Web site: http://cdip.ucsd.edu

Dean, R.G., & Dalrymple, R.A. (1984). *Water Wave Mechanics for Scientists and Engineers*. Englewood Cliffs, NJ: Prentice Hall.

Dodd, N., Blondeaux, P., Calvete, D., de Swart, H.E., Falques, A., Hulscher, S.J.M.H., Rozynski, G., & Vittori, G. (2003). The use of stability methods in understanding the morphodynamical behavior of coastal systems, *Journal of Coastal Research*, 19, 849–865.

Edelman, T. (1968). Dune erosion during storm conditions. In *Proceedings of 11th Conference on Coastal Engineering* (719–722). New York, NY: ASCE.

Falques, A., & Calvete, D. (2005). Large-scale dynamics of sandy coastlines: diffusivity and instability. *Journal of Geophysical Research*, 110(C3), C03007, DOI 10.1029/2004JC002587.

Feddersen, F., Guza, R.T., Herbers, T.H.C., & Elgar, S. (2000). Velocity moments in alongshore bottom stress parameterizations. *Journal of Geophysical Research*, 105(C4), 8673–8686.

Galappatti, R. & Vreugdenhil, C.B. (1985). A depth integrated model for suspended transport. *Journal of Hydraulic Research*, 23(4), 359–377.

Gallagher, E.L., Elgar, S., & Guza, R.T. (1998). Observations of sand bar evolution on a natural beach. *Journal of Geophysical Research*, 103(C2), 3203–3215.

Haas, K.A., Svendsen, I.A., Haller, M.C., & Zhao, Q. (2003). Quasi-three-dimensional modeling of rip current systems, *Journal of Geophysical Research*, 108(C7), 3217, DOI: 10.1029/2002JC001355.

Haller, M.C., Dalrymple, R.A., & Svendsen, I.A. (2002). Experimental study of nearshore dynamics on a barred beach with rip channels. *Journal of Geophysical Research*, 107(C6), 3061, DOI: 10.1029/2001JC000955.

Holland, K.T., Holman, R.A., Lippmann, T.C., Stanley, J., & Plant, N. (1997). Practical use of video imagery in nearshore oceanographic field studies. *IEEE Journal of Oceanic Engineering*, 22(1), 81–92.

Holman, R.A., Symonds, G., Thornton, E.B., & Ranasinghe, R. (2006). Rip spacing and persistence on an embayed beach. *Journal of Geophysical Research*, 111, C01006, doi:10.1029/2005JC002965.

Holman, R.A., & Bowen, A.J. (1982). Bars, bumps, and holes: models for the generation of complex beach topography. *Journal of Geophysical Research*, 87(C1), 457–468.

Horikawa, K. (1988). *Nearshore Dynamics and Coastal Processes*. Tokyo, Japan: University of Tokyo Press.

Keeley, J.R., & Bowen, A.J. (1977). Longshore Variations in Longshore Currents. *Canadian Journal of Earth Sciences*, 14, 1898–1905.

Klein, M.D., & Schuttelaars, H.M. (2006). Morphodynamic evolution of double-barred beaches. *Journal of Geophysical Research*, 111, C06017, DOI: 10.1029/2005JC003155.

Komar, P.D. (1998). *Beach Processes and Sedimentation, 2nd Ed*. Englewood Cliffs, NJ: Prentice Hall.

Lippmann, T.C., & Holman, R.A. (1989). Quantification of sand bar morphology: A video technique based on wave dissipation. *Journal of Geophysical Research,* 94 (C1), 995–1011.

List, J.H., Hanes, D.M., & Ruggiero, P. (2007). Predicting longshore gradients in longshore transport: Comparing the CERC formula to Delft3D. *Proceedings of the 30th International Conference on Coastal Engineering*, Vol. 4, 3370–3380.

MacMahan, J.H., Thornton, E.B., Reniers, A.J.H.M., Stanton, T.P., & Symonds, G. (2008). Low-energy rip currents associated with small bathymetric variations, *Marine Geology*, 255(3–4), 156–164.

MacMahan, J.H., Thornton, E.B., & Reniers, A.J.H.M. (2006). Rip current review. *Coastal Engineering*, 53, 191–208.

MacMahan, J.H., Thornton, E.B., Stanton, T., & Reniers, A.J.H.M. (2005). RIPEX: Observations of a rip current system. *Marine Geology*, 218, 113–134.

Masselink, G., & Pattiaratchi, C. (2000). Tidal asymmetry in sediment resuspension on a macrotidal beach in northwestern Australia. *Marine Geology*, 163, 257–274.

Masselink, G., & Turner, I. (1999). The effect of tides on beach morphodynamics. In Short, A.D. (Ed.), *Handbook of Beach and Shoreface Morphodynamics* (pp. 204-229). New York, NY: Wiley & Sons.

Masselink, G., & Hughes, M. (1998). Field investigation of sediment transport in the swash zone. *Continental Shelf Research*, 18, 1179–1199.

McCall, R.T., van Thiel de Vries, J.S.M., Plant, N.G., van Dongeren, A.R., Roelvink, J.A., Thompson, D.M., & Reniers, A.J.H.M. (2010). Two-dimensional time dependent hurricane overwash and erosion modeling at Santa Rosa Island. *Coastal Engineering*, 57, 668–683.

Murray, A.B. (2004). Rip channel development on nonbarred beaches: The importance of a lag in suspended-sediment transport. *Journal of Geophysical Research*, 109 (C4), DOI:10.1029/2002JC001581.

National Oceanic and Atmospheric Administration (2010a). *National Data Buoy Center*. Retrieved January 11, 2010, from NOAA's National Data Buoy Center Web site: http://www.ndbc.noaa.gov.

National Oceanic and Atmospheric Administration. (2010b). *NOS Hydrographic Survey Viewer*. Retrieved January 26, 2010, from NOAA Web site: http://map.ngdc.noaa.gov/website/mgg/nos_hydro/viewer.htm.

Nielsen, P., Robert, S., Møller-Christiansen, B., & Oliva, P. (2001). Infiltration effects on sediment mobility under waves. *Coastal Engineering*, 42, 105–114.

Nishi, R., & Kraus, C. (1996). Mechanism and calculation of sand dune erosion by storms. In *Proceedings of the 25th Coastal Engineering Conference* (3034–3047). New York, NY: ASCE.

O'Reilly, W.C., & Guza, R.T. (1993). A Comparison of two spectral wave models in the Southern California Bight. *Coastal Engineering* 19, 263–282.

Orzech, M.D., Thornton, E.B., MacMahan, J.H., O'Reilly, W.C., & Stanton, T.P. (2010). Alongshore rip channel migration and sediment transport. Marine Geology 271, 278–291.

Ozasa, H., & Brampton, A.H. (1980). Mathematical modeling of beaches backed by seawalls. *Coastal Engineering*, 4, 47–63.

Ranasinghe, R., Symonds, G., Black, K., & Holman, R.A. (2004). Morphodynamics of intermediate beaches: A video imaging and numerical modeling study. *Coastal Engineering*, 51, 629–655.

Ranasinghe, R., Symonds, G., & Holman, R.A. (1999). Quantitative characterization of rip currents via video imaging. In *Coastal Sediments 99* (987–1002). New York, NY: ASCE.

Raubenheimer, B., Guza, R.T., & Elgar, S. (1996). Wave transformation across the inner surf zone. *Journal of Geophysical Research*, 101 (C10), 25,589–25,597.

Reniers, A.J.H.M., MacMahan, J.H., Thornton, E.B., & Stanton, T.P. (2006). Modelling infragravity motions on a rip-channel beach. *Coastal Engineering*, 53, 209–222.

Reniers, A.J.H.M., Thornton, E.B., & Roelvink, J.A. (2004). Morphodynamic modeling of an embayed beach under wave-group forcing. *Journal of Geophysical Research,* 109, C01030, DOI: 10.1029/2002JC001586.

Rienecker, M.M., & Fenton, J.D. (1981). A Fourier approximation method for steady water waves. *Journal of Fluid Mechanics*, 104, 119–137.

Roelvink, J.A. (1993). Dissipation in random wave groups incident on a beach. *Coastal Engineering*, 19, 127–150.

Roelvink, D., Reniers, A., van Dongeren, A., van Thiel de Vries, J., McCall, R., & Lescinski, J. (2009). Modeling storm impacts on beaches, dunes and barrier islands. *Coastal Engineering*, 56(11–12), 1133–1152.

Roelvink, J.A. & van Banning, G.K.F.M. (1994). Design and development of Delft3D and application to coastal morphodynamics. In *Proceedings of Hydroinformatics'94 Conference* (pp. 451–456). Leiden, Netherlands: Balkema.

Roelvink, J.A., & Stive, M.J.F. (1989). Bar-generating cross-shore flow mechanisms on a beach. *Journal of Geophysical Research*, 94(C4), 4785–4800.

Ruessink, B.G., van Enckevort, I.M.J., Kingston, K.S., & Davidson, M.A. (2000). Analysis of observed two- and three-dimensional nearshore bar behaviour. *Marine Geology*, 169, 161–183.

Sallenger, A.H., & Holman, R.A. (1985). Wave energy saturation on a natural beach of variable slope. Journal of Geophysical Research, 90(C6), 11,939–11,944.

Short, A.D. (1985). Rip current type, spacing and persistence, Narrabeen Beach Australia. *Marine Geology*, 65, 47–71.

Short, A.D. (1979). Three-dimensional beach stage model. *Journal of Geology*, 87, 553–571.

Smit, M.W.J., Klein, M.D., & Stive, M.J.F. (2003). Morphodynamic modelling of rip channel migration. In *Proceedings of Coastal Sediments 2003* (100–112). Hackensack, NJ: World Scientific.

Soulsby, R. (1997). *Dynamics of marine sands*. London, England: Thomas Telford Publications. ISBN 0 7277 2584 X.

Thornton, E.B., Sallenger, A.H., & MacMahan, J.H. (2007). Rip currents, cuspate shorelines and eroding dunes. *Marine Geology*, 240 (1-4), 151–167.

Thornton, E.B., Humiston, R.T., & Birkemeier, W. (1996). Bar/trough generation on a natural beach. Journal *of Geophysical Research*, 101(C5), 12,097–12,110.

Thornton, E.B., & Kim, C.S. (1993). Longshore current and wave height modulation at tidal frequency inside the surf zone. *Journal of Geophysical Research*, 98 (C9), 16,509–16,519.

Thornton, E. B., & Guza, R.T. (1983). Transformation of wave height distribution. *Journal of Geophysical Research*, 88, 5925–5938.

Thornton, E.B., & Guza, R.T. (1982). Energy saturation and phase speeds measured on a natural beach. *Journal of Geophysical Research*, 87, 9499–9508.

Turner, I.L., Whyte, D., Ruessink, B.G., & Ranasinghe, R. (2007). Observations of rip spacing, persistence and mobility at a long, straight coastline. *Marine Geology*, 236, 209–221.

U.S. Army Corps of Engineers (2002). *Shore Protection* Manual, 8th ed. Washington, DC: Coastal Engineering Research Center.

Van Dongeren, A.R., Reniers, A.J.H.M., Battjes, J.A., & Svendsen, I.A. (2003). Numerical modeling of infragravity wave response during Delilah. *Journal of Geophysical Research*, 108 (C9), 3288, DOI:10.1029/2002JC001332.

Van Enckevort, I.M.J., & Ruessink, B.G. (2001). Effect of hydrodynamics and bathymetry on video estimates of nearshore sand bar position. *Journal of Geophysical Research*, 106 (C8), 16,969–16,979.

Van Thiel de Vries, J. (2008). *Dune Erosion During Storm Surges*. Delft, Netherlands: Deltares. ISBN 1877-5608.

Wright, L.D., & Short, A.D. (1984). Morphodynamic variability of surf zones and beaches: A synthesis. *Marine Geology*, 56, 93–118.

Zyserman, J., & Fredsøe, J. (1988). The effect of rip-currents on longshore sediment transport. In *Proceedings of 2nd International Symposium on Wave Research and Coastal Engineering* (127–138). Hannover: ISWRCE.

INITIAL DISTRIBUTION LIST

1. Defense Technical Information Center
   Ft. Belvoir, Virginia

2. Dudley Knox Library
   Naval Postgraduate School
   Monterey, California

3. Edward B. Thornton
   Department of Oceanography, NPS
   Monterey, California

4. Jamie H. MacMahan
   Department of Oceanography, NPS
   Monterey, California

5. Timothy P. Stanton
   Department of Oceanography, NPS
   Monterey, California

6. Thomas H.C. Herbers
   Department of Oceanography, NPS
   Monterey, California

7. Kenneth Davidson
   Department of Meteorology, NPS
   Monterey, California

8. Jeffrey D. Paduan
   Department of Oceanography, NPS
   Monterey, California

9. Ad Reniers
   RSMAS, University of Miami
   Coral Gables, Florida

10. Mark D. Orzech
    NRL Code 7322
    Stennis Space Center, Mississippi